

UC San Diego

UC San Diego Previously Published Works

Title

Two-dimensional perovskite templates for durable, efficient formamidinium perovskite solar cells

Permalink

<https://escholarship.org/uc/item/05d359b4>

Journal

Science, 384(6701)

ISSN

0036-8075

Authors

Sidhik, Siraj

Metcalf, Isaac

Li, Wenbin

et al.

Publication Date

2024-06-14

DOI

10.1126/science.abq6993

Copyright Information

This work is made available under the terms of a Creative Commons Attribution License, available at <https://creativecommons.org/licenses/by/4.0/>

Peer reviewed

Two-dimensional perovskite templates for durable, efficient formamidinium perovskite solar cells

Siraj Sidhik^{1,2#}, Isaac Metcalf^{1#}, Wenbin Li³, Tim Kodalle⁴, Connor Dolan⁵, Mohammad Khalili², Jin Hou¹, Faiz Mandani², Andrew Torma³, Hao Zhang³, Rabindranath Garai², Jessica Persaud², Amanda Marciel², Itzel Alejandra Muro Puente⁶, G. N. Manjunatha Reddy⁶, Adam Balvanz⁷, Mohamad A. Alam⁸, Claudine Katan⁹, Esther Tsai¹⁰, David Ginger¹¹, David Fenning⁵, Mercuri G. Kanatzidis¹², Carolin M. Sutter-Fella⁴, Jacky Even^{13*} and Aditya D. Mohite^{1,2*}

¹Material Science and Nanoengineering, Rice University, Houston, TX 77005, USA.

²Department of Chemical and Biomolecular Engineering, Rice University, Houston, TX 77005, USA.

³Applied Physics Graduate Program, Smalley-Curl Institute, Rice University, Houston, TX, 77005, USA.

⁴Molecular Foundry, Lawrence Berkeley National Laboratory, Berkeley, CA 94720, USA

⁵Department of Nanoengineering, University of California, San Diego, La Jolla, CA 92093, USA.

⁶University of Lille, CNRS, Centrale Lille Institut, Univ. Artois, UMR 8181-UCCS-Unité de Catalyse et Chimie du Solide, F-59000 Lille, France

⁷Department of Chemistry, Northwestern University, Evanston, IL 60208, USA.

⁸School of Electrical and Computer Engineering, Purdue University, West Lafayette, IN, USA.

⁹Univ Rennes, ENSCR, CNRS, ISCR-UMR 6226, Rennes F-35000, France.

¹⁰Center for Functional Nanomaterials, Brookhaven National Laboratory, Upton, NY, USA

¹¹Department of Chemistry, University of Washington, Seattle 98195.

¹²Department of Chemistry and Department of Materials Science and Engineering, Northwestern University, Evanston, IL 60208, USA.

¹³Univ Rennes, INSA Rennes, CNRS, Institut FOTON - UMR 6082, Rennes F-35000, France.

*Correspondence to: jacky.even@insa-rennes.fr; adm4@rice.edu

31 **Abstract**

32 **We present a design strategy for fabricating ultra-stable, phase pure films of formamidinium**
33 **lead iodide (FAPbI₃) by lattice templating using specific two-dimensional (2D) perovskites**
34 **with FA as the cage cation. When a pure FAPbI₃ precursor solution is brought in contact**
35 **with the 2D perovskite, the black phase forms preferentially at 100 °C, much lower than the**
36 **standard FAPbI₃ annealing temperature of 150 °C. X-ray diffraction and optical**
37 **spectroscopy suggest that the resulting FAPbI₃ film compresses slightly to acquire the (011)**
38 **interplanar distances of the 2D perovskite seed. The 2D templated bulk FAPbI₃ films**
39 **exhibited an efficiency of 24.1% in a p-i-n architecture with 0.5 cm² active area, and an**
40 **exceptional durability with T₉₇ of 1000 hours under 85 °C and maximum power point**
41 **tracking.**

42

43

44 Perovskite light absorbers with the chemical formula APbI₃ (where A is a monovalent cation) have
45 been extensively studied in photovoltaic devices. Among the commonly used A-site cations, such
46 as formamidinium (FA), methylammonium (MA), and caesium (Cs⁺), FA has shown promising
47 performance because of its lower bandgap (E_g), improved optoelectronic properties, and higher
48 thermal stability compared to MA (1). The larger size of the FA cation yields the Pm3m cubic
49 perovskite lattice through close packing, rather than the lower-symmetry tetragonal (I4/mcm)
50 lattice of MAPbI₃ (2,3). The lower E_g value of FAPbI₃ results from a high degree of Pb 6s - I 5p
51 orbital overlap and reduction of octahedral tilts. The FAPbI₃ lattice appears to be a polymorphous
52 network where the average high symmetry structure results from a random distribution of local
53 lower-symmetry (distorted) structural motifs (4). The complexity of the α - (black) phase of 3D
54 bulk FAPbI₃ is also reflected by the distribution of the reported average lattice parameter values
55 ranging at room temperature (RT) from a ranging from 6.352 to 6.365 Å (5,6).

56 Moreover, the high symmetry of the FAPbI₃ lattice comes at the expense of phase stability.
57 The Goldschmidt tolerance factor of the black α -phase of three-dimensional (3D) FAPbI₃ (0.987)
58 is at the edge of the stable range for the perovskite structure (0.8 to 1.0) because the FA cation is
59 almost too large for the A-site (7). As a result, the room temperature (RT) strain-free α -phase of
60 FAPbI₃ presents vanishing shear and bulk elastic moduli, and a metastability against the
61 reconstructive phase conversion to the yellow, photoinactive non perovskite δ -phase (5,8).
62 Alloying FA with Cs, MA, or both at the A-site can reduce the effective A-site radius of the
63 perovskite structure and lower the tolerance factor, which improves phase stability at RT but comes
64 at the expense of a widened bandgap (9-11).

65 Kinetically trapping the α -phase of FAPbI₃ is one of the key steps to achieve stable solar
66 cell operation at RT (12). Recently, there have been several reports on FA-based perovskites which
67 with certified power conversion efficiencies (PCEs) exceeding 25% (record 26.2%) for n-i-p (13-
68 20), and 24% for p-i-n device architectures (21-24), often by incorporating high concentrations of
69 methylammonium chloride (MACl) (25), formamidinium formate (16), methylene diammonium
70 dichloride (26), isopropyl ammonium chloride (27), and methylammonium formate (28), to
71 stabilize the black phase with a E_g of 1.52 eV or higher. The large E_g (compared to the lowest-
72 reported FAPbI₃ value of 1.45 eV obtained on single crystals (5,29)) is indicative of alloying
73 between FA and MA at the A-site of the perovskite lattices. Other cations, such as Cs⁺ (9,30), and
74 Rb⁺ (20,31), have also been studied for their potential to improve stability.

75 Nonetheless, the stability of these FA-based solar cells is still limited, specifically under
76 temperatures exceeding 60°C and AM1.5G light illumination under operation at maximum-power-
77 point tracking (MPPT). Recently, multiple studies have used bulky amine salts with FAPbI₃ to
78 stabilize the α -phase through the formation of a metastable two-dimensional (2D) perovskite phase

79 (19,27,32-40). These 2D perovskites have the chemical formula $A'_2A_{n-1}Pb_nI_{3n+1}$, where A' is a
80 bulky monoammonium cation and n controls the thickness of the perovskite layers. Inspired by
81 this success, we opted to combine in-plane lattice matched 2D perovskites with $FAPbI_3$, to create
82 lattice-matched interfaces using our newly introduced 2D memory seeds method, instead of
83 employing amine salts (41-43).

84 Here, we show that bulk $FAPbI_3$ forms a highly stable black phase at a temperature well
85 below the δ - $FAPbI_3$ to α - $FAPbI_3$ transition temperature by templating the (001) interplanar spacing
86 of 3D $FAPbI_3$ to the (011) interplanar spacing of a judiciously selected 2D phase (the respective
87 Pb-Pb interatomic spacing for each structure). The $FAPbI_3$ precursors, when drop-cast over a film
88 of Ruddlesden-Popper (RP) phase 2D perovskite $A'_2FAPb_2I_7$, where the A' cation can be
89 butylammonium (BA), or pentylammonium (PA), converted into black phase $FAPbI_3$ at
90 temperatures as low as 100 °C, which is well below the 150 °C temperature at which additive-free
91 control films underwent a yellow-to-black phase transition.

92 From our studies of film formation using correlated wide-angle x-ray scattering (WAXS),
93 optical absorbance, and photoluminescence (PL), we hypothesized that the resulting black $FAPbI_3$
94 phase exhibited a lattice constant corresponding to the $d_{(011)}$ interplanar spacing of the underlying
95 2D perovskite. We could also translate the 2D-templated stabilization of $FAPbI_3$ to scalable
96 solution-processed methods by adding the pre-synthesized 2D perovskites powders (0.5-1.0
97 mol%) into the $FAPbI_3$ precursor solutions. In a heterophase 3D-2D FA-based film, the phase-
98 stable 2D perovskite nucleated first because had a lower enthalpy of formation and was the phase
99 stable at RT. The 2D structure presented a perovskite surface on which the 3D perovskite can
100 form by distorting to adopt the underlying 2D lattice periodicity, allowing for the preferential
101 templating of the 3D perovskite on the 2D phase during subsequent film annealing. The obtained

102 bulk films of FAPbI₃ exhibit a bandgap (E_g) of 1.48 eV and demonstrate exceptional durability
103 under aggressive ISOS-L-2 conditions of 85°C/AM1.5G illumination and a PCE of 24.1% in a p-
104 i-n device architecture on a 0.5 cm² device area. We believe that these results validate a novel
105 design strategy for the templated growth of 3D perovskites using designer 2D perovskites, which
106 share a nearly identical lattice constant.

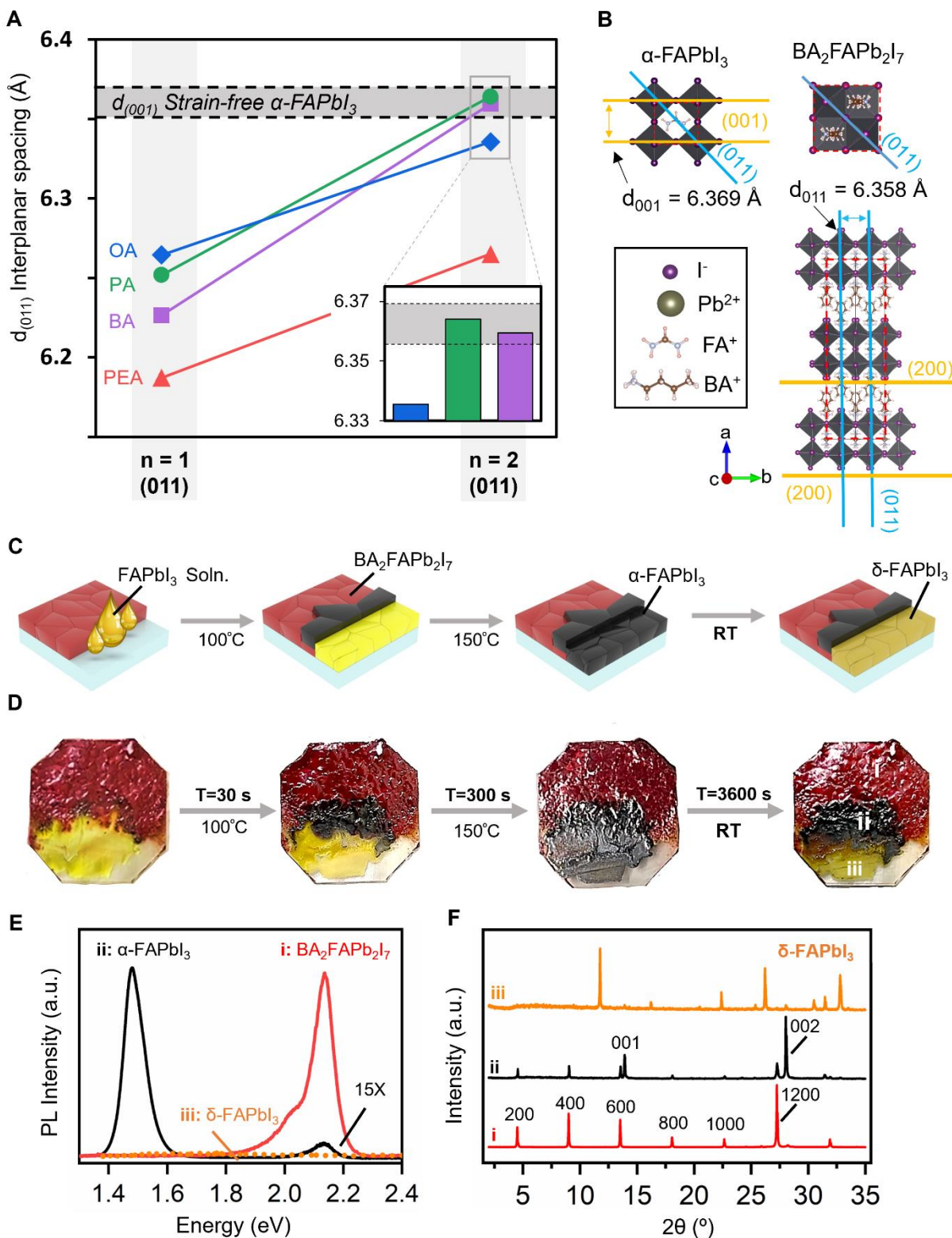
107 **Black phase stabilization of FAPbI₃ with 2D perovskite template**

108 The general design principle, the selection criteria, and proof-of-concept for the 2D perovskite-
109 based templating of FAPbI₃ are shown in **Fig. 1**. **Fig. 1A** shows the in-plane lattice parameter
110 corresponding to the Pb-I-Pb distance, along directions perpendicular to the (011) plane for the 2D
111 BA₂FAPb₂I₇ perovskite and the (001) plane for the 3D FAPbI₃ perovskite, as a function of layer
112 thickness (n-value) for 2D perovskites formed with a variety of A' site cations. The grey horizontal
113 bar represents the range of reported lattice parameters for bulk FAPbI₃ taken single-crystal
114 structural studies (5,6). The (011)^{2D} interplanar spacings were calculated from crystal structures
115 obtained with single-crystal diffraction of each 2D perovskite. Based on the lattice parameters, we
116 hypothesized that the lattice mismatch between the 2D and 3D perovskites must be kept low to
117 minimize the 2D-3D interfacial energy and encourage growth through templating.

118 We searched for FA-based 2D perovskites with an in-plane lattice parameter close to
119 FAPbI₃. As a result, we identified that 2D n=2 FA-based perovskites with the bulky cations
120 butylammonium (BA) and pentylammonium (PA), with lattice constants of 6.359 Å and 6.364 Å
121 respectively, were almost perfectly lattice matched with that of 3D FAPbI₃ lattice parameters.
122 However, our crystal structure analysis revealed that the phenylethylammonium (PEA) and
123 octylammonium (OA) n=2 Pb-I-Pb distance was too small (6.265 Å and 6.336 Å, lattice mismatch
124 of 1.5% and 0.5%, respectively) to match the 3D FAPbI₃ structure. Notably, all the n=1 2D

125 perovskites considered were lattice mismatched with FAPbI₃ and were not viable options for
126 templating the 3D phase.

127 **Fig. 1B** illustrates the crystal structure of α -FAPbI₃ and BA₂FAPb₂I₇ (BA n=2) 2D
128 perovskite, with a focus on the (001) and (011) planes. The typical 2D perovskite structure of
129 BA₂FAPb₂I₇ is shown, displaying the in-plane (001) and (011), and out-of-plane (200) lattice
130 planes. **Fig. 1C to 1F**, describes a preliminary experiment on the growth of a layer of FAPbI₃ on a
131 crystal of BA₂FAPb₂I₇. **Fig. 1C** (schematic) and **Fig. 1D** (optical images) shows the experiment at
132 different stages in time. We first partially covered a substrate with a film of red coloured,
133 millimeter-scale BA₂FAPb₂I₇ monocrystals that were fabricated with the air-liquid interface
134 method and spread on an indium tin oxide (ITO) glass substrate. Once these crystals were dried
135 on a hotplate at 100°C, we wiped away half the glass slide to create a bare glass region on about
136 half of the glass area. We then added a few drops of FAPbI₃ precursor solution (composed of an
137 equimolar ratio of FAI and PbI₂) onto the blank surface and annealed the substrate at a temperature
138 of 100°, 125°, or 150°C (experiments shown in **Fig. 1** were performed at a substrate temperature
139 of 100°C). The solution flowed over and react with the BA₂FAPb₂I₇ 2D perovskite crystal film.
140 Upon contact with the 2D crystals, the solution spontaneously (within 10 to 15 s) transformed into
141 a shiny black film. The same transformation was obtained for annealing temperatures of 125° and
142 150°C. After letting the film equilibrate for 5 min, we obtained three distinct regions on the
143 substrate (**Fig. 1D**).



144
145
146
147

Fig. 1. Design principle and proof-of-concept for 2D perovskite lattice templating of FAPbI₃. A) The $d_{(011)}$ interplanar spacing for $n=1$ and FA-based $n=2$ 2D perovskites with various A' cations: PA, BA, OA, and PEA. The range of reported values for FAPbI₃ $d_{(001)}$ interplanar spacing

148 is plotted as gray horizontal bar. Both $\text{BA}_2\text{FAPb}_2\text{I}_7$ and $\text{PA}_2\text{FAPb}_2\text{I}_7$ exhibit a $d_{(011)}$ nearly identical
149 to the $d_{(001)}$ of FAPbI_3 , as shown in the inset. **B)** Diagram of the unit cells of FAPbI_3 (left) and
150 $\text{BA}_2\text{FAPb}_2\text{I}_7$ (right). The (001) and (011) planes are drawn for each structure. The Pb-I-Pb distance
151 corresponds to the (001) interplanar spacing of FAPbI_3 and to the (011) spacing of $\text{BA}_2\text{FAPb}_2\text{I}_7$.
152 **C)** Schematics of the templated FAPbI_3 drop-coating experiment. First FAPbI_3 precursor solution
153 was dropped onto a glass substrate and allowed to flow over crystals of $\text{BA}_2\text{FAPb}_2\text{I}_7$. When heated,
154 the δ - FAPbI_3 on top of the $\text{BA}_2\text{FAPb}_2\text{I}_7$ transformed to α - FAPbI_3 before the δ - FAPbI_3 on top of
155 the bare substrate. Left in ambient air, the α - FAPbI_3 on top of the bare substrate transformed to δ -
156 FAPbI_3 before the α - FAPbI_3 on top of the $\text{BA}_2\text{FAPb}_2\text{I}_7$. **D)** Corresponding photographs of the
157 experiment in **(C)** showing the three distinct regions of the substrate. i: $\text{BA}_2\text{FAPb}_2\text{I}_7$ without
158 FAPbI_3 solution, ii: $\text{BA}_2\text{FAPb}_2\text{I}_7$ below FAPbI_3 solution, and iii: FAPbI_3 solution on bare glass.
159 **E)** PL, and **(F)** XRD of regions i, ii, and iii after 1 hour of exposure to ambient air, showing that
160 the α - FAPbI_3 was stabilized when deposited above $\text{BA}_2\text{FAPb}_2\text{I}_7$.

161
162 The lower region of the substrate, which was originally bare, changed to a black color with
163 partially converted α - FAPbI_3 , at 100 °C. The middle region where the solution touched the 2D
164 perovskite consisted of the black phase FAPbI_3 on the surface and $\text{BA}_2\text{FAPb}_2\text{I}_7$ below that. Finally,
165 the top part of the substrate where the solvent did not flow remained as $\text{BA}_2\text{FAPb}_2\text{I}_7$ of millimeter-
166 sized monocrystal film. We then left the film for 1 hour under ambient conditions. As the
167 temperature decreased, the bottom region (originally the bare glass region) converted to the yellow
168 phase of FAPbI_3 while the intermediate region remained black, suggesting the successful phase
169 stabilization of the FAPbI_3 . The $\text{BA}_2\text{FAPb}_2\text{I}_7$ crystal film remained unchanged over this time
170 because of its inherent stability compared to its 3D counterpart.

171 We characterized the three regions of the final film using both PL and XRD measurements.
172 **Fig. 1C** shows the PL spectra of the film obtained at the three specific regions, labelled (i), (ii),
173 and (iii). The dominant PL of region (i) at 2.15 eV corresponded to the ground-state excitonic
174 emission of $\text{BA}_2\text{FAPb}_2\text{I}_7$ film, accompanied by a small shoulder around 2.0 eV. The intermediate
175 region (ii) showed strong emission at 1.48 eV corresponding to the intrinsic bandgap of the α -
176 FAPbI_3 phase, with very weak emission at around 2.15 eV from $\text{BA}_2\text{FAPb}_2\text{I}_7$. These results
177 indicated the coexistence of the bulk black phase FAPbI_3 3D perovskite atop the 2D perovskite

178 crystal film. The presence of the 2D perovskite at the bottom was confirmed by PL measurements
179 taken from the back of the film in region (ii), which exhibited emission solely from the 2D
180 perovskite. As anticipated, no emission was observed from region (iii) that contained the
181 photoinactive yellow phase of the FAPbI₃. Additional PL analysis for the drop-coating experiment
182 is shown in **Fig. S1**. The detection of n=3 (BA₂FA₂Pb₃I₁₀) in the photoluminescence (PL)
183 measurement acquired from the rear side provides clear evidence of the intercalation process, a
184 phenomenon previously reported by our group (refer to **Fig. S1**) (44). We emphasize that the phase
185 stabilization of FAPbI₃ occurred also at 100° and 125°C, which are well below the standard
186 annealing temperatures of 150° to 160°C.

187 The XRD measurements presented in **Fig. 1F** validated the findings from the
188 measurements in **Fig. 1, C to E**. Region (i) showed a pure 2D BA₂FAPb₂I₇ perovskite as evidenced
189 by the strong interlayer (h00) XRD plane originating from the inorganic layer stacking. From
190 region (ii), we found a similar XRD pattern but with the (001) and (002) diffraction planes from
191 the α -phase FAPbI₃ perovskite that indicates the presence of a mixture of 2D and 3D perovskites.
192 In region (iii), XRD showed only the presence of the δ -phase FAPbI₃.

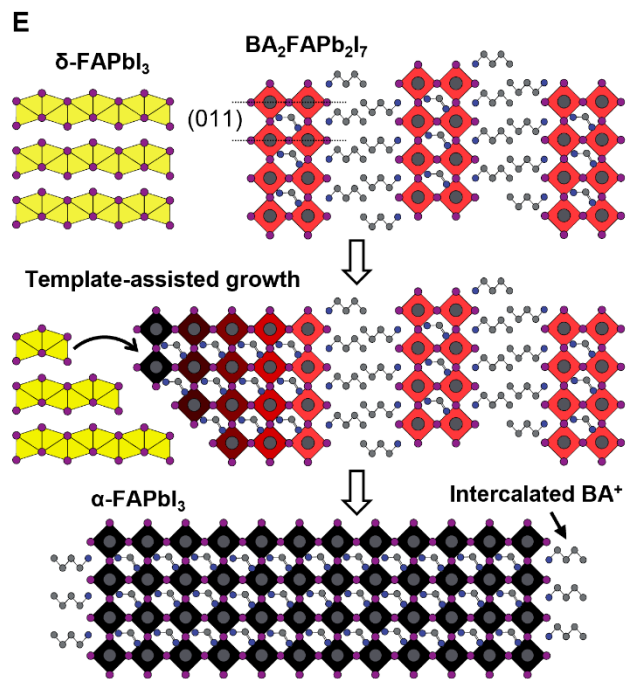
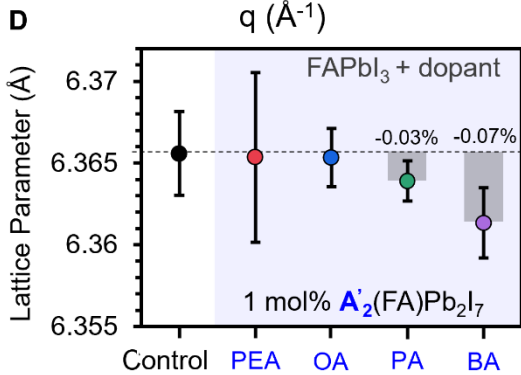
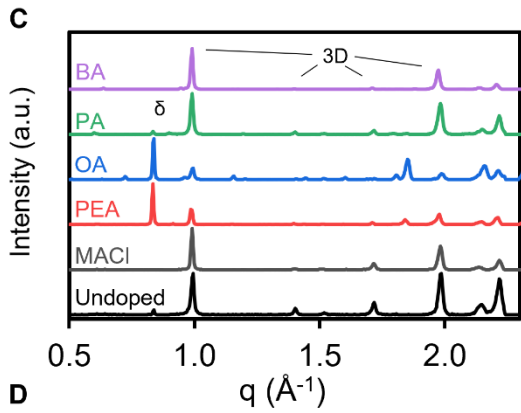
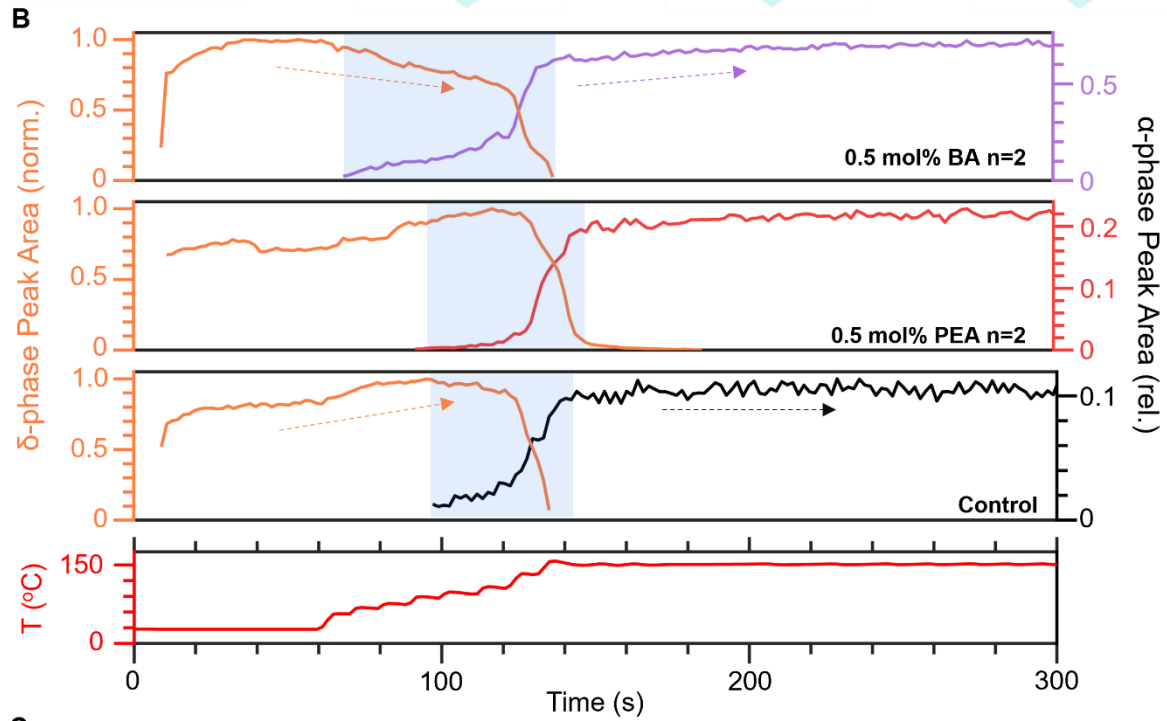
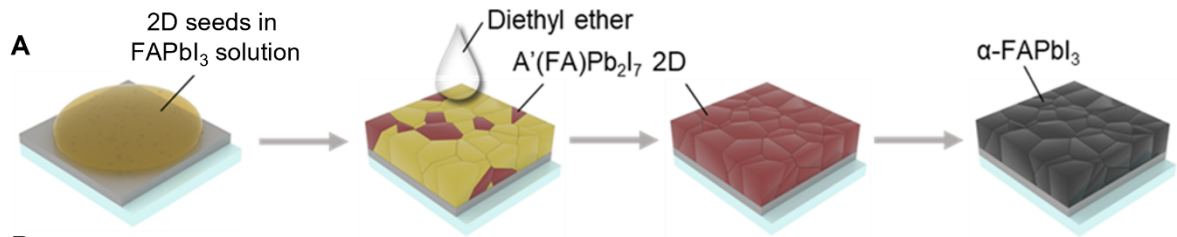
193 The results shown in **Fig. 1** suggest that the incorporation of BA₂FAPb₂I₇ into FAPbI₃
194 during film formation could stabilize the perovskite phase through templating between the two
195 structures' Pb-I-Pb interatomic distances. To test this hypothesis in FAPbI₃ films, 2D perovskites
196 were added as templating agents to precursor solutions of 1:1 FAI: PbI₂ in mixed 4:1 DMF: DMSO
197 solvent. We compared the effect of 2D perovskites with four different A'-site cations: BA, PA,
198 OA, and PEA. Using a technique previously developed by our group (41), pre-synthesized 2D
199 crystals were added instead of the more conventional choice of A' cation halide salts. Rather than
200 dissolving completely into constituent ions, 2D crystals in a DMF: DMSO solvent formed sub-

201 micrometer sized crystallites (termed as memory seeds) that preserved their perovskite structure
202 and served as nucleation sites during film formation. These memory seeds could transfer their
203 initial n-value to solution-processed films. However, when dissolved in a FAPbI₃ precursor
204 solution rather than pure DMF: DMSO, 2D perovskite crystallites were surrounded by a high
205 concentration of mobile A-site cations, which tended to intercalate into the seeds and increase their
206 n-value. As a result, a 2D additive with a given A'-site cation will grow from a FAPbI₃ solution at
207 its thermodynamically preferred n-value in such an environment. With this in mind, only 2D
208 perovskites of the n-value that will precipitate from a FAPbI₃ solution were considered as
209 candidates for α -phase stabilization. Through solution processing experiments summarized in **Fig.**
210 **S2**, we found that each of the four RP 2D perovskites considered here grew in their n=2 phase
211 from FAPbI₃ solution.

212 **Crystallization dynamics of 2D templated FAPbI₃ thin films**

213 We used our selectively designed 2D perovskites BA₂FAPb₂I₇ and PA₂FAPb₂I₇ to grow stabilized
214 FAPbI₃ perovskite thin films. **Fig. 2A** visually illustrates the film formation process of FAPbI₃
215 with 2D perovskite additive, offering insight into the visible alterations that occur during the
216 process. Perovskite films were synthesized by spin-coating with precursors of FAI: PbI₂:2D
217 perovskite with a molar ratio of 1:1:x mol%. After antisolvent washing with diethyl ether, the thin
218 film underwent a series of intermediate stages, which can be seen visually as changes in colour
219 from pale red (before annealing) to dark brown, and finally to a black film when annealed at
220 temperatures ranging from 100° to 150°C for 20 minutes.

221



223 **Fig. 2. 2D-stabilized FAPbI₃ film formation mechanism.** **A)** Fabrication steps of a 2D crystal
224 templated FAPbI₃ thin film, **B)** Integrated peak areas for the (100)^δ (orange, left axis) and (001)^{3D}
225 (black, right axis) peaks over time for control FAPbI₃ (bottom), FAPbI₃ with 0.5 mol% PEA n=2
226 added (middle), and FAPbI₃ with 0.5 mol% BA n=2 added (top). The (001)^{3D} peak area as
227 indicated on the right vertical axis is normalized to the maximum of the (100)^δ peak area. The
228 regions between the emergence of the (001)^{3D} peak and the full conversion to α-FAPbI₃ are
229 highlighted in blue. **C)** Azimuthally integrated WAXS patterns averaged across the first 90
230 seconds of annealing after reaching 150°C for each FAPbI₃ additive tested (2D concentration is 1
231 mol%). **D)** The α-FAPbI₃ (001) lattice parameter for films with 1 mol% of each 2D additive, as
232 measured on separately fabricated samples at RT. Error bars indicate standard deviation based on
233 data from 3 to 5 samples. **E)** Schematic diagram illustrating the mechanism of lattice-matched 2D
234 templated FAPbI₃ perovskite formation.

235
236 To elucidate the mechanism that produces a RT phase-stable FAPbI₃ film, we measured
237 the structural dynamics of the perovskite during thin-film formation using synchrotron-based
238 WAXS. The perovskite thin-films were deposited from solution onto a bare ITO substrate by using
239 a robotic antisolvent pipette and a resistive-heating spin-coater in a WAXS chamber under a
240 nitrogen atmosphere (**Fig. S3**). We first investigated the crystallization kinetics of a FAPbI₃ film
241 with 1 mol% BA₂FAPb₂I₇ incorporated. A WAXS pattern taken during thin-film formation (**Fig.**
242 **S4**) showed concentric diffraction rings corresponding to the Bragg reflections of the stacking axis
243 diffraction planes of BA₂FAPb₂I₇ and α- and δ- phases of 3D-FAPbI₃. The diffraction peaks
244 correspond to crystallographic planes in the 2D, α-FAPbI₃, and δ-FAPbI₃ crystal structures.

245 The WAXS pattern was azimuthally integrated and plotted as a function of time along with
246 spin speed and temperature to observe the film's structural evolution (**Fig. S4**). In this in-situ
247 experiment can be divided into four stages: (i) antisolvent dropping during spin-coating; (ii) after
248 spin-coating but before annealing; (iii) slow annealing ramping from RT to 150°C; and (iv)
249 constant annealing at 150°C. The δ- phase FAPbI₃ immediately formed after depositing antisolvent
250 (10 s), as indicated by the strong (100)^δ (q , the length of the reciprocal lattice vector, is 0.84 \AA^{-1}),
251 (101)^δ, and (110)^δ diffraction planes (drawn in **Fig. S5**). Once the spin-coating is completed (30 s),

252 the δ -phase persisted as 2D $\text{BA}_2\text{FAPb}_2\text{I}_7$ seeds began to crystallize at RT, illustrated by the out-
253 of-plane $(400)^{2\text{D}}$ ($q = 0.65\text{\AA}^{-1}$) and $(600)^{2\text{D}}$ ($q = 0.96\text{\AA}^{-1}$) diffraction peaks (**Fig. S4**).

254 Next, a nonlinear stepwise annealing sequence was applied, in which the substrate
255 temperature was increased by steps of 20°C in 20 second intervals up to 100°C and then increased
256 by steps of 25°C up to 150°C (stage iii). Slow ramping to 150°C allowed us to observe the onset
257 temperature of the FAPbI_3 α -phase. In this stage, for annealing at low temperatures ($<100^\circ\text{C}$), the
258 diffraction intensity of the 2D increased and a new peak emerged near $q = 1\text{\AA}^{-1}$ corresponding to
259 the $(001)^{3\text{D}}$ plane from α -phase FAPbI_3 . **Fig. 2B, top** shows the integrated peak area for the $(100)^\delta$
260 and $(001)^{3\text{D}}$ peaks as a function of time for FAPbI_3 with 0.5 mol% BA $n=2$ incorporated. The
261 $(001)^{3\text{D}}$ peak emerged after 75 s and slowly increases in intensity as the $(100)^\delta$ peak simultaneously
262 decreases. Around after 130 s ($T = 130^\circ\text{C}$), the remaining δ -phase abruptly converted into α -phase.
263 As the film continued to anneal at 150°C for the remainder of the experiment (stage iv), the 2D
264 diffraction peaks slowly faded and the α -phase FAPbI_3 peaks slowly grew more intense.

265 We repeated this experiment for four other types of precursor solutions. For additive-free
266 FAPbI_3 : **Fig. S6A** shows the in-situ contour WAXS plot for a 1:1 $\text{FAI}:\text{PbI}_2$ solution. In contrast to
267 the FAPbI_3 -2D sample, which exhibited a gradual emergence of α -phase between 100° and 150°C
268 followed by a complete $\delta \rightarrow \alpha$ transformation at 130°C , the additive-free (control) FAPbI_3 showed
269 a much more abrupt transition from δ -phase to α -phase near 150°C (**Fig. 2B, bottom**) consistent
270 with previous reports. The $(001)^{3\text{D}}$ peak emerged later with a shorter tail in control FAPbI_3 , and
271 the $(100)^\delta$ peak did not prematurely decrease as in the film that incorporated BA $n=2$. We observed
272 a much lower $(001)^{3\text{D}}$ peak intensity (relative to the $(100)^\delta$ peak intensity) for control pristine
273 FAPbI_3 compared to FAPbI_3 with BA $n=2$ additive, suggesting a lowered crystallinity. Unlike the

274 film with added BA n=2, the (001)^{3D} peak of control FAPbI₃ did not grow more intense as
275 annealing at 150°C continued.

276 For a precursor solution of 1:1:35 mol% FAI: PbI₂: MAcl in 4:1 DMF: DMSO, which is
277 commonly used to grow phase stabilized FAPbI₃ (25), the introduction of MA into the A-site of
278 FAPbI₃ lowered the effective tolerance factor and stabilized the α -phase at a lower temperature
279 compared to additive-free FAPbI₃. As a result, the abrupt $\delta \rightarrow \alpha$ transformation occurred at 75°C
280 for the FAPbI₃-MAcl sample (**Fig. S6B and S10A**). However, like the control sample and in
281 contrast to the 2D-templated sample, no region of gradual $\delta \rightarrow \alpha$ transformation was observed.

282 Next, BA n=2 was added to 1:1 PbI₂: FAI with concentrations of 0.25, 0.5, and 1.0 mol%.
283 **Fig. S7** shows contour plots of the in-situ WAXS experiment for additive concentrations of 0.25
284 mol% (top) and 1.0 mol% (bottom). In all cases, the incorporation of BA n=2 increased the (001)^{3D}
285 peak intensity relative to the control, suggesting that even minute amounts of BA n=2 could
286 improve α -phase crystallinity. The 0.5 mol% BA n=2 incorporated FAPbI₃ showed a similar film
287 formation process to the 1.0 mol% sample discussed above, that is, a decrease in the (100) ^{δ} peak
288 and a slow emergence of the (001)^{3D} peak at a lowered temperature. However, 0.25 mol% BA n=2
289 incorporation did not lower the onset temperature of the (001)^{3D} peak relative to the control, and
290 did not cause the same characteristic decrease in (100) ^{δ} intensity below 150°C. The phase-
291 stabilization appeared to be concentration invariant down to a certain minimum 2D concentration,
292 below which the templating effect was lost but the film crystallinity was still improved.

293 We then examined a series of 2D additives including PA n=2, OA n=2, and PEA n=2. We
294 note that the effect PA n=2 was similar to that of BA n=2, lowering the onset temperature of the
295 α -phase peak and causing a decrease in the δ -phase below 150°C (**Fig. S8 and S10B**). In contrast,
296 OA n=2 and PEA n=2 have markedly different effects (**Fig. S9 and S10B**). For OA n=2, the 2D

307 peaks formed weakly and the α -phase emerged earlier than for the control sample, but no $\delta \rightarrow \alpha$
308 transformation was observed. Instead, the δ -phase persisted throughout annealing, suggesting that
309 $\text{OA}_2\text{FAPb}_2\text{I}_7$ seeds could serve as nucleation sites for FAPbI_3 to a limited extent but slowed the δ
300 $\rightarrow \alpha$ transformation. FAPbI_3 with 0.5 mol% PEA n=2 additive showed no 2D peaks and no early
301 α -phase emergence (**Fig. 2B, middle**). Moreover, FAPbI_3 with 1 mol% PEA n=2 also retained δ -
302 phase peaks throughout the measurement, suggesting that the $\text{PEA}_2\text{FAPb}_2\text{I}_7$ not only failed to form
303 seeds for templating FAPbI_3 but also suppressed $\delta \rightarrow \alpha$ transformation kinetics. **Fig. 2C** shows the
304 azimuthally integrated WAXS patterns of FAPbI_3 samples with 1 mol% 2D, averaged across the
305 first 90 s of annealing at 150°C. This plot revealed the incomplete $\delta \rightarrow \alpha$ transformation for the
306 films incorporating 1 mol% OA and PEA n=2, contrasting with the complete transformation for 1
307 mol% BA and PA n=2 (also visible in **Fig. S10**). Interestingly, all 2D films showed a slow decrease
308 in the 2D peak intensities and a slow increase in the $(001)^{3\text{D}}$ peak intensity during annealing at
309 150°C that was not observed for the control film (**Fig. 2B and Fig. S10**). Although gradual
310 volatilization of the A' cation in $\text{A}'_2\text{FAPb}_2\text{I}_7$, leaving behind FAPbI_3 could account for these
311 changes, as discussed below, optical and nuclear magnetic resonance (NMR) results suggest that
312 the 2D phase was not completely lost to volatilization, and that there may be a competing
313 mechanism of 2D restructuring within the lattice.

314 The in-situ WAXS results suggested that $\text{BA}_2\text{FAPb}_2\text{I}_7$ and $\text{PA}_2\text{FAPb}_2\text{I}_7$ could template α -
315 phase FAPbI_3 , but $\text{OA}_2\text{FAPb}_2\text{I}_7$ and $\text{PEA}_2\text{FAPb}_2\text{I}_7$ could not. Ex-situ 1D XRD was performed on
316 separate 1 mol% 2D-incorporated FAPbI_3 films (**Fig. 2D**) and showed that FAPbI_3 films with
317 added OA n=2 or PEA n=2 had an identical $(001)^{3\text{D}}$ interplanar spacing as control FAPbI_3 , but that
318 PA n=2 and BA n=2 caused a small but noticeable compression of the $(001)^{3\text{D}}$ interplanar spacing
319 by -0.03% and -0.07%, respectively. Because the $(011)^{2\text{D}}$ interplanar spacing was lightly smaller

320 for BA n=2 than for PA n=2 (**Fig. 1A**), a higher compressive strain for FAPbI₃ with added BA
321 n=2 compared to PA n=2 also supports the (011) lattice templating hypothesis.

322 To verify our structural results, we performed similar in-situ optical spectroscopy
323 measurements on the BA₂FAPb₂I₇-templated FAPbI₃ samples. During the initial stages of
324 annealing, the film exhibited a strong excitonic absorption peak at 2.15 eV corresponding to
325 BA₂FAPb₂I₇, which with progressive annealing transformed into α -FAPbI₃, characterized by a 3D
326 perovskite absorption band edge (**Fig. S11**). Similarly, a strong emission of the BA₂FAPb₂I₇
327 perovskite was observed at 2.15 eV in the in-situ PL measurement, accompanied by a broad
328 emission at lower energies (**Fig. S12**). We hypothesized that the lower energy emissions were from
329 a combination of effects, including edge state emission (45, 46), the formation of higher n-value
330 2D phases (e.g. n=3 BA₂FA₂Pb₃I₁₀) (47,48), and quantum confinement effects of the 2D and
331 FAPbI₃ crystallites (49-52). Sub-bandgap edge state emission in BA₂FAPb₂I₇ was verified by
332 spatially resolved PL, which showed a 1.8 eV PL emission peak only at the edges of an exfoliated
333 BA₂FAPb₂I₇ single crystal. Additionally, the presence of a PL emission peak at 1.85eV and the
334 observation of n=3 excitons in power-dependent PL indicate that FA intercalation increases the
335 layer thickness from n=2 to n=3 during annealing. A similar broad emission below the n=2
336 bandgap was observed during film formation for FAPbI₃ with PA₂FAPb₂I₇ additive (**Fig. S12**),
337 consistent with the structural results for PA₂FAPb₂I₇ shown in **Fig. S8**. However, no sub-bandgap
338 emission was observed for the control FAPbI₃ or for FAPbI₃ incorporating MACl, OA₂FAPb₂I₇,
339 or PEA₂FAPb₂I₇ (**Fig. S13**).

340 Based on the in-situ WAXS and PL measurements in **Fig. 2** and **Fig. S2 to S10**, we propose
341 the following film formation process mediated by 2D templating. The film first forms grains of δ -
342 phase FAPbI₃ and 2D seeds at RT. The 2D likely formed initially because of its more negative

343 formation enthalpy, its RT phase-stability, and the presence of 2D seeds in the precursor solution
344 as confirmed through dynamic light scattering (DLS) measurements shown in **Fig. S14**. During
345 annealing, the δ -phase restructured itself beginning at the low-energy surfaces of the 2D seed
346 crystals to form α -phase FAPbI₃. At the interface with FAPbI₃, the arrangement of PbI₆ octahedra
347 in a 2D perovskite may facilitate nucleation of a stable α -phase FAPbI₃, with subsequent phase
348 transformation toward the bulk (53). Indeed, from **Fig. 2D**, we deduced that the growth mechanism
349 favoured the formation of a compressively strained α -phase (001) plane templated by the 2D (011)
350 interplanar spacing. The low-temperature α -phase formation being only observed for films with
351 added PA and BA n=2, and these films being also the only ones to exhibit lattice strain, is strong
352 evidence for a templating effect off the (011)^{2D} spacing.

353 The (011) interplanar spacings of BA₂FAPb₂I₇ (6.359 Å) and PA₂FAPb₂I₇ (6.364 Å) are
354 almost perfectly lattice matched with the (001)^{3D} interplanar spacing of FAPbI₃, both falling within
355 the range of reported FAPbI₃ lattice constants from 6.352 Å to 6.365 Å (5,6), whereas the (011)
356 interplanar spacings of OA₂FAPb₂I₇ (6.336 Å) and PEA₂FAPb₂I₇ (6.265 Å) were not well matched.
357 This structural difference explains why OA-2D and PEA-2D did not show the same $\delta \rightarrow \alpha$
358 conversion process as BA-2D and PA-2D. The templating process and the resulting FAPbI₃ strain
359 appeared 2D concentration-independent down to some minimum threshold, which for BA 2D
360 perovskites was between 0.25 and 0.5 mol%. As the temperature was raised to 150°C and the
361 sample continued to anneal, we hypothesize that the 2D perovskite simultaneously volatilized its
362 A' cation and underwent a slow FA intercalation process, which increased its n-value.

363 Other reports have suggested that the A' cation of 2D perovskites incorporated into FAPbI₃
364 volatilized completely during annealing except for a small fraction left at grain boundaries,^{19,37,38}
365 which would also explain the disappearance of our 2D signal over time and the slow increase in

366 the (001)^{3D} peak intensity during annealing at 150°C. Solid-state ¹H NMR on scraped films of
367 FAPbI₃ with added 2D before and after annealing did reveal a partial volatilization of the spacer
368 cation during film formation, but also confirmed appreciable fractions of BA and PA even after
369 annealing at 150°C for 20 min (**Fig. S15** and **S16**). Time-of-flight secondary-ion mass
370 spectrometry (ToF-SIMS) results suggested that the remaining 2D spacer cations were
371 homogenously distributed up to 1 mol% and for higher concentrations, appeared more pronounced
372 toward the film interface with the substrate (**Fig. S17**).

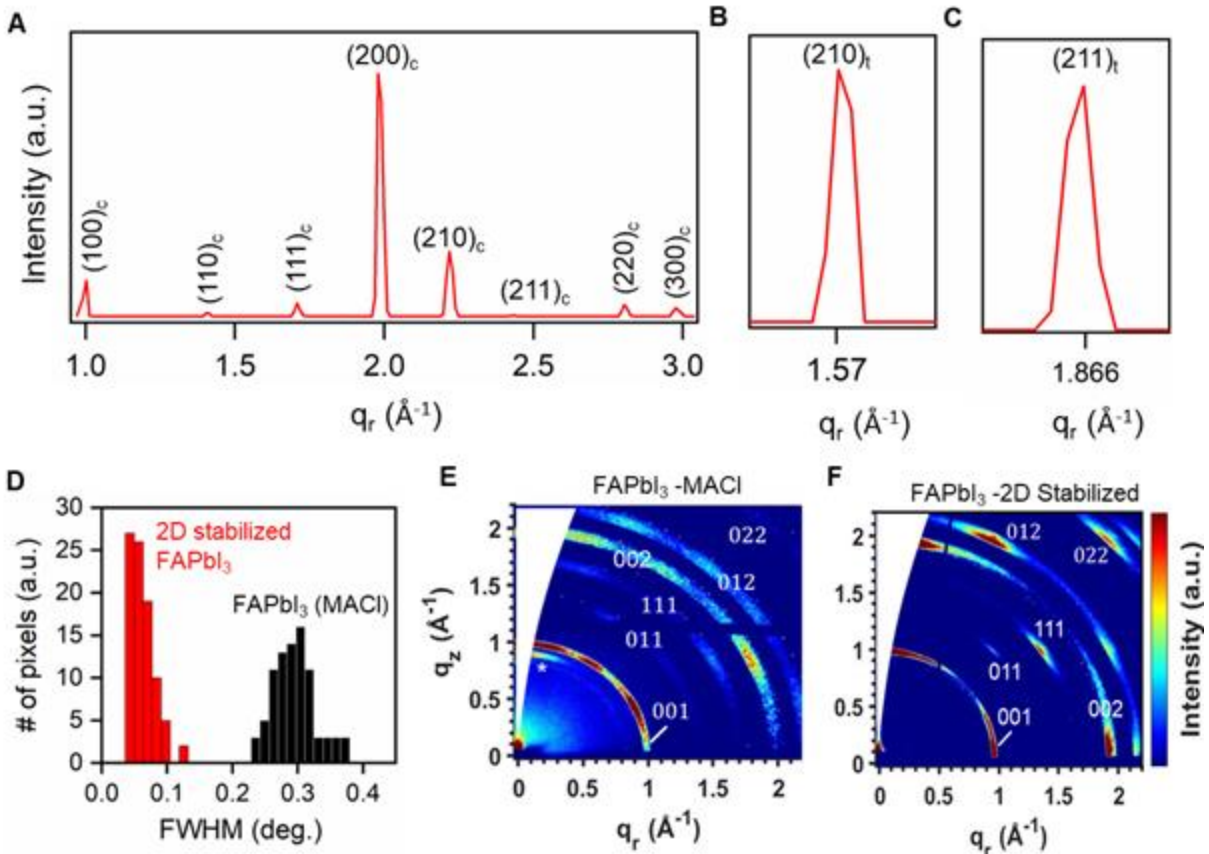
373 The BA and PA cations lead to the formation of a mixed 2D/3D phase that was challenging
374 to characterize with the aforementioned long-range techniques. Instead, we applied high-field (21
375 T) solid-state NMR spectroscopy to resolve the local structures of the organic cations in the mixed
376 phase (**Fig. S16**). The ¹H NMR peaks associated with the large (BA and PA) and small (FA)
377 cations were well resolved so the amount of 2D phase present in the templated FAPbI₃ materials
378 could be identified and quantified. In addition, the local structures of the mixed phases, elucidated
379 by analysing 2D ¹H-¹H correlation NMR spectra (**Fig. S16, C to F**), showed the presence of
380 through-space intermolecular interactions between the large cations (BA or PA) in the 2D phase
381 and the small cations (FA) in the 3D FAPbI₃ phase. Based on the data presented above, we
382 illustrate a comprehensive schematic diagram capturing the different stages of film formation in a
383 2D templated FAPbI₃ (**Fig. 2E and discussion in SI 1.18**).

384

385

386

387



388

389 **Fig. 3. Ex-situ structural characterization of phase stabilized FAPbI₃ films.** A) A
 390 representative azimuthally integrated nano-XRD pattern for a film of BA₂FAPb₂I₇-templated
 391 FAPbI₃. B) The (210)_h, and C) the (211)_h peaks of BA₂FAPb₂I₇-templated FAPbI₃ which can be
 392 seen after integrating several nano-XRD patterns obtained for different pixels within the testing
 393 region. These peaks are forbidden in a cubic crystal structure and confirm the existence of
 394 tetragonal FAPbI₃. D) A histogram of nano-XRD peak FWHM values for different pixels of a
 395 BA₂FAPb₂I₇-stabilized FAPbI₃ film (red) and a MACI-stabilized FAPbI₃ film (black). 2D-
 396 stabilized FAPbI₃ shows a significantly lower FWHM. E – F) Representative GIWAXS patterns
 397 for E) MACI-stabilized FAPbI₃ and F) BA₂FAPb₂I₇-stabilized FAPbI₃.

398

399 Structural and optical characteristics of Phase stabilized FAPbI₃

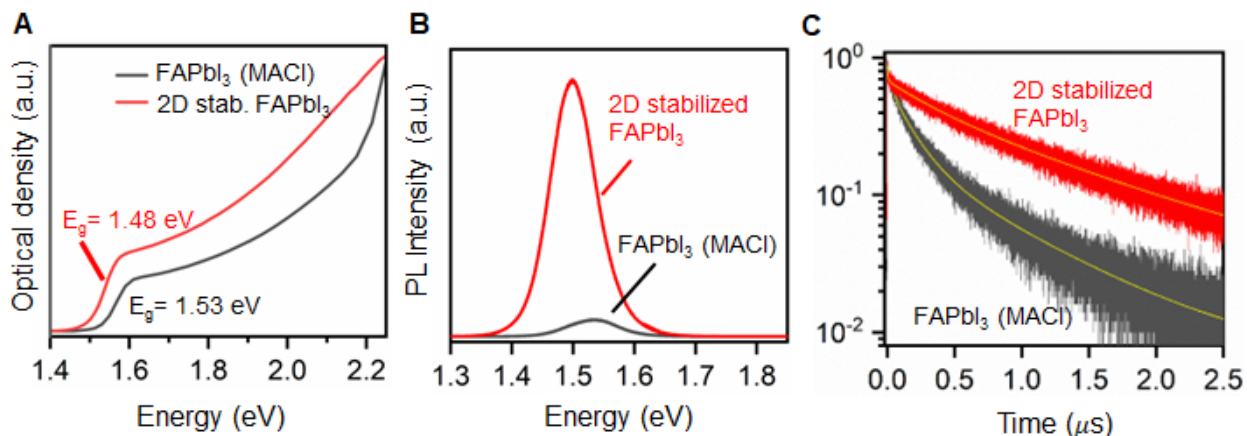
400 We hypothesized that the observed compressive lattice strain applied by the templating 2D phase
 401 can result in the formation of a locally segregated tetragonal structure (54,55). To investigate the
 402 impact of 2D stabilization on nanoscale structural properties of FAPbI₃, we performed nanoscale
 403 XRD with a 25-nm spot size x-ray probe on MACI-stabilized FAPbI₃ and 2D-stabilized FAPbI₃.
 404 The high brilliance of a synchrotron light source enabled resolution of diffraction from minority

405 phases (56,57). As shown in **Fig. S18**, both films showed sufficient x-ray stability to accommodate
406 the measurement. Localized x-ray scattering from both cubic (i.e., α) and tetragonal phases was
407 observed. A representative summed diffraction CCD image from a map of 2D-stabilized FAPbI₃
408 is shown in **Fig. S19**, and an azimuthally integrated pattern is shown in **Fig. 3A**. In addition to
409 intense scattering from the cubic perovskite lattice, we observed two subtle peaks that we indexed
410 to the tetragonal phase, the (210)_t (t=tetragonal) at 1.57 Å⁻¹ and (211)_t at 1.866 Å⁻¹ (**Fig. 3, B and**
411 **C**). The (211)_t peak could not be definitively indexed as tetragonal because of the overlapping
412 (210)_h (h=hexagonal, δ -phase) peak at virtually the same scattering vector, but the (210)_t was
413 unambiguously identified (58). Furthermore, because we observed no additional scattering peaks
414 from the hexagonal phase in this sample, we also attribute the (211)_t peak to the tetragonal phase.
415 The diffraction from tetragonal phase was far less intense than diffraction from the cubic phase,
416 with total summed diffraction intensity from the (211)_t peak amounting to 0.8% of the intensity of
417 the (200)_c (c=cubic) peak (see **Fig. S19**).

418 To investigate the impacts of 2D stabilization on the quality of the perovskite crystallites
419 in the thin film, we performed five-dimensional rocking curves (rocking curves with a two-
420 dimensional detector and two-dimensional spatial mapping) on the sample where the angle of the
421 incident x-ray was varied and spatial maps in the plane of the sample were repeated over the same
422 area to precisely analyze the width of the diffraction peak. The 2D-stabilized FAPbI₃ exhibited
423 substantially narrower diffraction full-width at half-maximum (FWHM) than the MAI-doped
424 FAPbI₃ (**Fig. 3D**). The narrower diffraction peak could be a result of an increase in domain size or
425 reduced microstructural disorder (microstrain) (59). However, the well-established increase in
426 domain size seen when MAI was included in perovskite precursors suggested that a smaller
427 domain size in MAI-doped FAPbI₃ was not the cause (25,60,61). We concluded that the 2D-

428 stabilization resulted in a reduced structural disorder within the crystallites of the thin film, which
429 is consistent with previous reports (53). Halder-Wagner analysis summarized in **Fig. S20** and **S21**
430 further revealed that microstrain in 2D-stabilized FAPbI₃ decreased with increasing 2D
431 concentration.

432 The grazing-incidence WAXS (GIWAXS) patterns of the MACl-doped FAPbI₃ perovskite
433 thin films (**Fig. 3E**) and FAPbI₃ with BA₂FAPb₂I₇ additive revealed two different characteristics
434 of the thin films. The MACl-doped FAPbI₃ films exhibited Bragg intensities extended along arc
435 segments, indicating a random orientation of crystal domains or grains within a polycrystalline
436 film (high mosaicity). Furthermore, these films showed PbI₂ diffraction peaks. In contrast, the 2D-
437 stabilized FAPbI₃ films reveal well-defined Bragg diffraction spots along the (001) plane, observed
438 along the Debye–Scherrer ring near $q = 1 \text{ \AA}^{-1}$. This distinct observation implied smaller mosaicity
439 and improved grain orientation in the out-of-plane direction, perpendicular to the substrate.
440 Furthermore, mosaicity appeared to be reduced with increasing 2D concentration (**Fig. S22**).
441 Atomic force microscopy (AFM) likewise showed an increase in FAPbI₃ grain size when 2D
442 concentration was increased from 0.25 mol% to 0.5 mol%, although a further increase caused the
443 grain size to decrease (**Fig. S23**). These results were consistent with the observation in **Fig. S7** of
444 improved crystallinity for FAPbI₃ films incorporating even small amounts of BA n=2.



445

446 **Fig. 4. Optical characterization of the phase stabilized FAPbI₃ films.** **A)** Absorption spectra of
447 MACl-stabilized FAPbI₃ (grey) and BA₂FAPb₂I₇-stabilized FAPbI₃ (red) with their band gaps
448 indicated. **B)** PL spectra of MACl-stabilized FAPbI₃ (gray) and BA₂FAPb₂I₇-stabilized FAPbI₃
449 (red). **C)** TRPL spectra of MACl-stabilized FAPbI₃ (gray) and BA₂FAPb₂I₇-stabilized FAPbI₃
450 (red).

451 We observed an increase in the absorption of the 2D stabilized FAPbI₃ compared to the
452 MACl-doped FAPbI₃. (**Fig. 4A**). Using the Tauc plot calculated from the absorption spectrum
453 (**Fig. S24**), we derived a bandgap of 1.48 eV for the 2D stabilized FAPbI₃ (versus the 1.52 eV band
454 gap of the MACl-doped films) that was much closer to the smallest reported (1.45 eV) bandgap of
455 FAPbI₃ (5). This band gap reduction (**Fig. 4A-B**) was consistent with experimental signatures
456 pointing toward a reduction of the lattice disorder (**Fig. 3E-F**) (53). In a polymorphous picture of
457 the cubic phase of FAPbI₃, the reduction of polymorphism also leads to reduced tilt amplitudes
458 (4,62). As 2D concentration increased, the valence band maximum (VBM) was lowered (**Fig. S25**)
459 and the band gap widened.

460 We also observed an order of magnitude increase in the PL intensity of the 2D-stabilized
461 FAPbI₃ compared to the MACl-doped FAPbI₃ indicating reduced nonradiative recombination
462 (**Fig. 4B**). The PL peak positions aligned with the absorption thresholds for both the films. In time-
463 resolved PL measurements (**Fig. 4C**), the 2D stabilized FAPbI₃ film exhibited a slower PL decay
464 rate compared to the reference, implying a decrease in nonradiative recombination attributable to
465 a reduction in trap-mediated bulk or surface recombination processes.

466 **Photovoltaic studies**

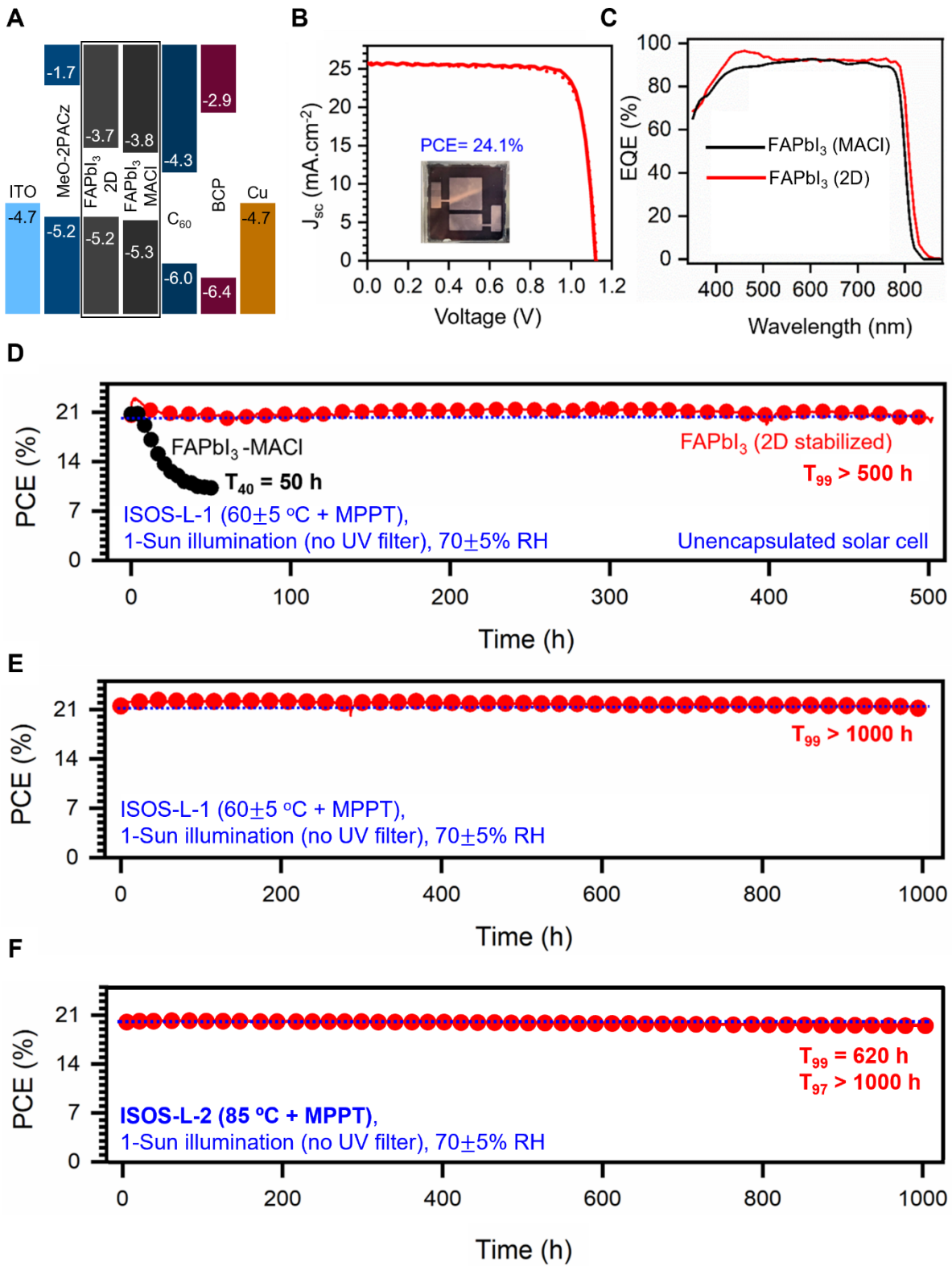
467 We used 2D stabilized FAPbI₃ to fabricate perovskite solar cells using an inverted architecture
468 with MeO-2PACz as the hole transport layer and C₆₀ as the electron transport layer. To construct
469 a band diagram of the device architecture (**Fig. 5A**), we measured the valence band maxima and
470 conduction band minima of the MACl-doped FAPbI₃ and 2D stabilized FAPbI₃ by combining
471 photoemission yield spectroscopy (PES) and absorption measurements. The details of the

472 measurements are discussed in the methods section of the SI. The 2D stabilized FAPbI₃ although
473 slightly shifted toward higher energy compared to the MACl-doped FAPbI₃ had an appropriate
474 band alignment for charge carrier separation and extraction.

475 The current density-voltage (J - V) characteristics of the best-performing 2D stabilized
476 FAPbI₃ device in reverse and forward bias sweeps are illustrated in **Fig. 5B**. We achieved a power
477 conversion efficiency (PCE) of 24.1% for an active area of 0.5 cm² under AM1.5G illumination
478 (**Fig. 5E**) with a short circuit current density (J_{SC}) of 25.5 mA.cm⁻², open circuit voltage (V_{OC}) of
479 1.12 V, and fill factor of 82%. These metrics compare favourably with the corresponding
480 thermodynamic limits of 31.1 mA.cm⁻², 1.21 V, and 89%, respectively (63). **Fig. 5C** shows the
481 external quantum efficiency (EQE) for the same device as that of the J - V curve. Solar cells under
482 identical conditions using different 2D perovskite concentration were fabricated to confirm the
483 impact of concentration on performance. The statistical distributions of J_{SC} , V_{OC} , fill factor (FF),
484 and PCE for 40 devices of each condition are shown in **Fig. S26**. The J_{SC} obtained by integrating
485 the EQE over the wavelength is 24.3 mA cm⁻², which was in good agreement with that of the
486 device's J - V curve measured using a solar simulator. For comparison, we fabricated FAPbI₃
487 devices stabilized using PA₂FAPb₂I₇, OA₂FAPb₂I₇ and PEA₂FAPb₂I₇ (see **Fig. S27**). The PA-
488 templated FAPbI₃ device exhibited a PCE of 21%, with a J_{sc} of 25.2 mA.cm-2, V_{OC} of 1.06V, and
489 FF of 78.1%. In the case of optimized OA- and PEA-templated FAPbI₃, we achieved PCEs of
490 16.54% (J_{sc} of 23.93 mA.cm-2, V_{OC} of 0.97V, and FF of 71%) and 14.65% (J_{sc} of 23.15 mA.cm⁻
491 ², V_{OC} of 0.96V, and FF of 65%), respectively.

492 Finally, we compared the intrinsic and operational stability of undoped, BA₂FAPb₂I₇-
493 templated, and MACl-doped FAPbI₃ films and devices. The 2D-templated FAPbI₃ was
494 exceptionally stable under a variety of conditions compared to both undoped and MACl-doped

495 FAPbI₃. The shelf stability of 2D-stabilized FAPbI₃ films showed a significant improvement
496 compared to undoped FAPbI₃ (**Fig. S28**). We also performed in-situ GIWAXS measurements (**Fig.**
497 **S29**) to compare the stability of MACl-doped and BA₂FAPb₂I₇-incorporated FAPbI₃ devices in a
498 >90%RH environment at 65°C with 1-Sun illumination. The 2D-templated FAPbI₃ device showed
499 minimal $\alpha \rightarrow \delta$ conversion over 170 min in the degrading environment. In contrast, the δ -phase
500 became dominant in the MACl-doped FAPbI₃ device within the first 15 min of measurement. The
501 much higher stability of the 2D-templated FAPbI₃ device in this experiment corroborated the
502 maximum power point tracking (MPPT) device stability tests shown in **Fig. 5D** for 2D-templated
503 FAPbI₃ and MACl-doped FAPbI₃.



504

505 **Figure 5: 2D-stabilized FAPbI₃ device performance.** **A)** Device architecture of best-performing
 506 device showing band alignment of each layer. **B)** The J-V curve of the champion device shows

507 both a forward sweep (solid line) and reverse sweep (dashed line). The inset shows a real image
508 of the device. **C)** The EQE of the champion 2D-stabilized FAPbI₃ device compared to the
509 champion MAI-stabilized FAPbI₃ device. **D-F)** Stability tests on 2D stabilized FAPbI₃. **D)**
510 Unencapsulated 2D-FAPbI₃ (red) and MAI-FAPbI₃ (black) cell under 1-sun illumination at 60°C
511 with MPP tracking, in ambient air. **E)** Encapsulated cell under 1-sun illumination at 60°C with
512 MPP tracking. **F)** Encapsulated cell under 1-sun illumination at 85°C with MPP tracking.
513

514 We evaluated the device stability with standard interfaces. We first performed
515 measurements on unencapsulated p-i-n solar cells in ambient air under 1-Sun illumination (no UV
516 filter) with MPPT. As shown in **Fig. 5D**, the 2D-templated devices showed almost no PCE drop
517 during the first 500 hours of operation with $T_{99}>500$ h. In contrast, the unencapsulated MAI-
518 doped FAPbI₃ sample degraded within the first 50 hr of operation showing a $T_{40}=50$ h. Further, as
519 shown in **Fig. 5E**, an encapsulated 2D-templated FAPbI₃ device showed almost no efficiency drop
520 from an initial 21% PCE for more than 1000 hours ($T_{99}>1000$ hr) of continuous 1-Sun illumination
521 at MPPT in ambient air (ISOS-L-1 protocol). This stability is among the best reported for FAPbI₃-
522 based perovskite devices, which in recent reports (26,27,36) have been measured under inert
523 conditions.

524 The encapsulated solar cells were additionally measured under 1-sun illumination at MPPT
525 at 85°C on a hot plate in the ambient atmosphere (ISOS-L-2 protocol), as shown in **Fig. 5F**. The
526 2D-stabilized FAPbI₃ devices retained 99% of their initial PCE after 620 hours, and more than
527 97% of their initial PCE after 1000 hours. Using the rule of thumb from Si photovoltaics that a
528 10°C increase in temperature translates to a 2x increase in degradation rate (64), a $T_{97} = 1000$ hours
529 at 85°C corresponds to a $T_{97} = 16000$ hours (1.8 years) at 45°C. This result is a critical step towards
530 a FAPbI₃-based device with commercially-relevant stability.

531

532

533 Discussion

534 In summary, our investigation unveils a unique approach to achieve a highly stable black phase of
535 FAPbI₃, even at temperatures considerably lower than the δ -FAPbI₃ to α -FAPbI₃ transition
536 temperature. This method involves templating the (001) interplanar spacing of 3D FAPbI₃ to the
537 (011) interplanar spacing of carefully selected 2D perovskites with FA as the cage cation,
538 considering the respective Pb-Pb interatomic spacing for each structure. Detailed characterization,
539 incorporating correlated WAXS, optical absorbance, and PL, indicates that the resulting black
540 FAPbI₃ phase exhibits a lattice constant corresponding to the $d_{(011)}$ interplanar spacing of the
541 underlying 2D perovskite. We extend this templating strategy to scalable solution-processed
542 methods by introducing pre-synthesized 2D perovskite seeds to FAPbI₃ precursor solutions.
543 During the film formation, the phase-stable 2D perovskite nucleates first due to its lower enthalpy
544 of formation and stability at room temperature. The 2D structure acts as a seed on which the 3D
545 perovskite to adopt the underlying 2D lattice periodicity, allowing for the preferential templating
546 of the 3D perovskite on the 2D phase during subsequent film annealing. The resulting bulk FAPbI₃
547 films exhibit an energy gap (E_g) of 1.48 eV and demonstrate exceptional durability under
548 aggressive conditions, achieving a remarkable PCE of 24.1% in a p-i-n device architecture on a
549 0.5 cm² device area. These outcomes validate a novel design strategy for the templated growth of
550 3D perovskites using 2D perovskites and will enable new physical behaviours and properties and
551 functionalities relevant for optoelectronic devices. We anticipate that such strategies might extend
552 beyond perovskites, potentially using other molecular and organic systems with comparable lattice
553 constants to produce epitaxial kinetically stabilized materials.

554
555
556
557

558 REFERENCES

559

- 560 1. Masi, S., Gualdrón-Reyes, A. F. & Mora-Seró, I. Stabilization of Black Perovskite Phase in FAPbI₃
561 and CsPbI₃. *ACS Energy Lett.* **5**, 1974–1985 (2020).
- 562 2. Huang, Y. *et al.* The intrinsic properties of FA(1-x)MAxPbI₃ perovskite single crystals. *J. Mater.*
563 *Chem. A* **5**, 8537–8544 (2017).
- 564 3. Tao, S. *et al.* Absolute energy level positions in tin-and lead-based halide perovskites. *Nature*
565 *communications* **10**, 2560 (2019).
- 566 4. Zhao, X.-G., Dalpian, G. M., Wang, Z. & Zunger, A. Polymorphous nature of cubic halide perovskites.
567 *Phys. Rev. B* **101**, 155137 (2020).
- 568 5. Stoumpos, C. C., Malliakas, C. D. & Kanatzidis, M. G. Semiconducting Tin and Lead Iodide
569 Perovskites with Organic Cations: Phase Transitions, High Mobilities, and Near-Infrared
570 Photoluminescent Properties. *Inorg. Chem.* **52**, 9019–9038 (2013).
- 571 6. Kawachi, S. *et al.* Structural and Thermal Properties in Formamidinium and Cs-Mixed Lead Halides.
572 *J. Phys. Chem. Lett.* **10**, 6967–6972 (2019).
- 573 7. Kieslich, G., Sun, S. & Cheetham, A. K. An extended tolerance factor approach for organic–inorganic
574 perovskites. *Chemical science* **6**, 3430–3433 (2015).
- 575 8. Ferreira, A. C. *et al.* Elastic softness of hybrid lead halide perovskites. *Physical Review Letters* **121**,
576 085502 (2018).
- 577 9. Li, Z. *et al.* Stabilizing perovskite structures by tuning tolerance factor: formation of formamidinium
578 and cesium lead iodide solid-state alloys. *Chemistry of Materials* **28**, 284–292 (2016).
- 579 10. Saliba, M. *et al.* Cesium-containing triple cation perovskite solar cells: improved stability,
580 reproducibility and high efficiency. *Energy & environmental science* **9**, 1989–1997 (2016).
- 581 11. Jeon, N. J. *et al.* Compositional engineering of perovskite materials for high-performance solar cells.
582 *Nature* **517**, 476–480 (2015).

- 583 12. Entropy-driven structural transition and kinetic trapping in formamidinium lead iodide perovskite |
584 Science Advances. <https://www.science.org/doi/10.1126/sciadv.1601650>.
- 585 13. Green, M. A. *et al.* Solar cell efficiency tables (version 62). *Progress in Photovoltaics: Research and*
586 *Applications* **31**, 651–663 (2023).
- 587 14. Min, H. *et al.* Perovskite solar cells with atomically coherent interlayers on SnO₂ electrodes. *Nature*
588 **598**, 444–450 (2021).
- 589 15. Yoo, J. J. *et al.* Efficient perovskite solar cells via improved carrier management. *Nature* **590**, 587–593
590 (2021).
- 591 16. Jeong, J. *et al.* Pseudo-halide anion engineering for α -FAPbI₃ perovskite solar cells. *Nature* **592**, 381–
592 385 (2021).
- 593 17. Kim, M. *et al.* Conformal quantum dot–SnO₂ layers as electron transporters for efficient perovskite
594 solar cells. *Science* **375**, 302–306 (2022).
- 595 18. Jeong, M. J. *et al.* Boosting radiation of stacked halide layer for perovskite solar cells with efficiency
596 over 25%. *Joule* **7**, 112–127 (2023).
- 597 19. Park, J. *et al.* Controlled growth of perovskite layers with volatile alkylammonium chlorides. *Nature*
598 1–3 (2023) doi:10.1038/s41586-023-05825-y.
- 599 20. Zhao, Y. *et al.* Inactive (PbI₂)₂RbCl stabilizes perovskite films for efficient solar cells. *Science* **377**,
600 531–534 (2022).
- 601 21. Jiang, Q. *et al.* Surface reaction for efficient and stable inverted perovskite solar cells. *Nature* **611**,
602 278–283 (2022).
- 603 22. Li, Z. *et al.* Organometallic-functionalized interfaces for highly efficient inverted perovskite solar cells.
604 *Science* **376**, 416–420 (2022).
- 605 23. Zhu, Z. *et al.* Correlating the perovskite/polymer multi-mode reactions with deep-level traps in
606 perovskite solar cells. *Joule* **6**, 2849–2868 (2022).
- 607 24. Li, G. *et al.* Highly efficient p-i-n perovskite solar cells that endure temperature variations. *Science*
608 **379**, 399–403 (2023).

- 609 25. Kim, M. *et al.* Methylammonium Chloride Induces Intermediate Phase Stabilization for Efficient
610 Perovskite Solar Cells. *Joule* **3**, 2179–2192 (2019).
- 611 26. Min, H. *et al.* Efficient, stable solar cells by using inherent bandgap of α -phase formamidinium lead
612 iodide. *Science* **366**, 749–753 (2019).
- 613 27. Park, B. *et al.* Stabilization of formamidinium lead triiodide α -phase with isopropylammonium chloride
614 for perovskite solar cells. *Nat Energy* **6**, 419–428 (2021).
- 615 28. Hui, W. *et al.* Stabilizing black-phase formamidinium perovskite formation at room temperature and
616 high humidity. *Science* **371**, 1359–1364 (2021).
- 617 29. Lee, J.-W., Seol, D.-J., Cho, A.-N. & Park, N.-G. High-Efficiency Perovskite Solar Cells Based on the
618 Black Polymorph of HC(NH₂)₂PbI₃. *Advanced Materials* **26**, 4991–4998 (2014).
- 619 30. Kim, G. *et al.* Impact of strain relaxation on performance of α -formamidinium lead iodide perovskite
620 solar cells. *Science* **370**, 108–112 (2020).
- 621 31. Park, Y. H. *et al.* Inorganic Rubidium Cation as an Enhancer for Photovoltaic Performance and
622 Moisture Stability of HC(NH₂)₂PbI₃ Perovskite Solar Cells. *Advanced Functional Materials* **27**,
623 1605988 (2017).
- 624 32. Alanazi, A. Q. *et al.* Benzylammonium-Mediated Formamidinium Lead Iodide Perovskite Phase
625 Stabilization for Photovoltaics. *Advanced Functional Materials* **31**, 2101163 (2021).
- 626 33. Alanazi, A. Q. *et al.* Atomic-Level Microstructure of Efficient Formamidinium-Based Perovskite Solar
627 Cells Stabilized by 5-Ammonium Valeric Acid Iodide Revealed by Multinuclear and Two-
628 Dimensional Solid-State NMR. *J. Am. Chem. Soc.* **141**, 17659–17669 (2019).
- 629 34. Hu, R. *et al.* Enhanced stability of α -phase FAPbI₃ perovskite solar cells by insertion of 2D (PEA)₂
630 PbI₄ nanosheets. *Journal of Materials Chemistry A* **8**, 8058–8064 (2020).
- 631 35. Huang, Y. *et al.* Low-Temperature Phase-Transition for Compositional-Pure α -FAPbI₃ Solar Cells
632 with Low Residual-Stress and High Crystal-Orientation. *Small Methods* **6**, 2200933 (2022).
- 633 36. Lee, J.-W. *et al.* 2D perovskite stabilized phase-pure formamidinium perovskite solar cells. *Nat*
634 *Commun* **9**, 3021 (2018).

- 635 37. Liang, J. *et al.* Volatile 2-Thiophenemethylammonium and Its Strongly Bonded Condensation Product
636 for Stabilizing α -FAPbI₃ in Sequential-Deposited Solar Cells. *ACS Materials Lett.* **5**, 1395–1400
637 (2023).
- 638 38. Liang, J. *et al.* Volatile 2D Ruddlesden-Popper Perovskite: A Gift for α -Formamidinium Lead
639 Triiodide Solar Cells. *Advanced Functional Materials* 2207177 (2022).
- 640 39. Shen, C. *et al.* Stabilizing Formamidinium Lead Iodide Perovskite by Sulfonyl-Functionalized
641 Phenethylammonium Salt via Crystallization Control and Surface Passivation. *Solar RRL* **4**, 2000069
642 (2020).
- 643 40. Shi, P. *et al.* Oriented nucleation in formamidinium perovskite for photovoltaics. *Nature* 1–5 (2023)
644 doi:10.1038/s41586-023-06208-z.
- 645 41. Sidhik, S. *et al.* Memory Seeds Enable High Structural Phase Purity in 2D Perovskite Films for High-
646 Efficiency Devices. *Adv. Mater.* **33**, 2007176 (2021).
- 647 42. Sidhik, S. *et al.* High-phase purity two-dimensional perovskites with 17.3% efficiency enabled by
648 interface engineering of hole transport layer. *Cell Reports Physical Science* **2**, 100601 (2021).
- 649 43. Metcalf, I. *et al.* Synergy of 3D and 2D Perovskites for Durable, Efficient Solar Cells and Beyond.
650 *Chem. Rev.* **123**, 9565–9652 (2023).
- 651 44. Hou, J., Li, W., Zhang, H., Sidhik, S., Fletcher, J., Metcalf, I., Anantharaman, S.B., Shuai, X., Mishra,
652 A., Blancon, J.C. and Katan, C. Synthesis of 2D perovskite crystals via progressive transformation of
653 quantum well thickness. *Nature Synthesis*, **pp.1-11**, (2023).
- 654 45. Blancon, J.-C., Even, J., Stoumpos, Costas. C., Kanatzidis, Mercouri. G. & Mohite, A. D.
655 Semiconductor physics of organic–inorganic 2D halide perovskites. *Nat. Nanotechnol.* **15**, 969–985
656 (2020).
- 657 46. Blancon, J.-C. *et al.* Extremely efficient internal exciton dissociation through edge states in layered 2D
658 perovskites. *Science* **355**, 1288–1292 (2017).
- 659 47. Blancon, J.-C. *et al.* Scaling law for excitons in 2D perovskite quantum wells. *Nat Commun* **9**, 2254
660 (2018).

- 661 48. Stoumpos, C. C. *et al.* Ruddlesden–Popper Hybrid Lead Iodide Perovskite 2D Homologous
662 Semiconductors. *Chem. Mater.* **28**, 2852–2867 (2016).
- 663 49. Even, J., Pedesseau, L. & Katan, C. Understanding quantum confinement of charge carriers in layered
664 2D hybrid perovskites. *ChemPhysChem* **15**, 3733–3741 (2014).
- 665 50. Tamarat, P. *et al.* Universal scaling laws for charge-carrier interactions with quantum confinement in
666 lead-halide perovskites. *Nature Communications* **14**, 229 (2023).
- 667 51. Saponi, D., Kepenekian, M., Pedesseau, L., Katan, C. & Even, J. Quantum confinement and dielectric
668 profiles of colloidal nanoplatelets of halide inorganic and hybrid organic–inorganic perovskites.
669 *Nanoscale* **8**, 6369–6378 (2016).
- 670 52. Katan, C., Mercier, N. & Even, J. Quantum and dielectric confinement effects in lower-dimensional
671 hybrid perovskite semiconductors. *Chemical reviews* **119**, 3140–3192 (2019).
- 672 53. Song, S. *et al.* Molecular Engineering of Organic Spacer Cations for Efficient and Stable
673 Formamidinium Perovskite Solar Cell. *Advanced Energy Materials* **10**, 2001759 (2020).
- 674 54. Doherty, T. A. S. *et al.* Stabilized tilted-octahedra halide perovskites inhibit local formation of
675 performance-limiting phases. *Science* **374**, 1598–1605 (2021).
- 676 55. Beal, R. E. *et al.* Structural Origins of Light-Induced Phase Segregation in Organic-Inorganic Halide
677 Perovskite Photovoltaic Materials. *Matter* **2**, 207–219 (2020).
- 678 56. Winarski, R. P. *et al.* A hard X-ray nanoprobe beamline for nanoscale microscopy. *J Synchrotron Rad*
679 **19**, 1056–1060 (2012).
- 680 57. Li, N. *et al.* Microscopic degradation in formamidinium-cesium lead iodide perovskite solar cells under
681 operational stressors. *Joule* **4**, 1743–1758 (2020).
- 682 58. Weber, O. J. *et al.* Phase Behavior and Polymorphism of Formamidinium Lead Iodide. *Chem. Mater.*
683 **30**, 3768–3778 (2018).
- 684 59. Ungár, T. Microstructural parameters from X-ray diffraction peak broadening. *Scripta Materialia* **51**,
685 777–781 (2004).

- 686 60. Li, Y. *et al.* CH₃NH₃Cl Assisted Solvent Engineering for Highly Crystallized and Large Grain Size
687 Mixed-Composition (FAPbI₃)_{0.85}(MAPbBr₃)_{0.15} Perovskites. *Crystals* **7**, 272 (2017).
- 688 61. Ye, F. *et al.* Roles of MAcl in Sequentially Deposited Bromine-Free Perovskite Absorbers for Efficient
689 Solar Cells. *Advanced Materials* **33**, 2007126 (2021).
- 690 62. Zacharias, M., Volonakis, G., Giustino, F. & Even, J. Anharmonic electron-phonon coupling in
691 ultrasoft and locally disordered perovskites. *npj Comput Mater* **9**, 1–13 (2023).
- 692 63. Alam, M. A. & Khan, M. R. *Principles of solar cells: connecting perspectives on device, system,*
693 *reliability, and data science.* (World Scientific Publishing Co. Pte. Ltd, 2022).
- 694 64. Boyd, C. C., Cheacharoen, R., Leijtens, T. & McGehee, M. D. Understanding Degradation
695 Mechanisms and Improving Stability of Perovskite Photovoltaics. *Chem. Rev.* **119**, 3418–3451 (2019).

696

697

698 **Acknowledgements**

699 In situ diffraction experiments were conducted at the Advanced Light Source, beamline 12.3.2
700 supported by Nobumichi Tamura, which is a US Department of Energy Office of Science User
701 Facility under contract no. DE-AC02-05CH11231. The authors thank Jonathan Slack from the
702 ALS for development and maintenance of the in-situ spin coater. The authors are grateful to
703 Tanguy Terlier for the measurement and analysis of ToF-SIMS data.

704 **Funding:**

705 The work Rice University was supported by the DOE-EERE DE-EE0010738 program. I.M.
706 acknowledges the financial support from the Hertz Foundation and the National Science
707 Foundation Graduate Research Fellowship Program (This material is based upon work supported
708 by the National Science Foundation Graduate Research Fellowship Program under grant no. NSF
709 20-587. Any opinions, findings and conclusions or recommendations expressed in this material
710 are those of the author and do not necessarily reflect the views of the National Science Foundation).
711 A.B. was supported by a fellowship through the National Science and Engineering Graduate
712 Fellowship Program (NDSEG) sponsored by the Air Force Research Laboratory (AFRL), the
713 Office of Naval Research (ONR), and the Army Research Office (ARO). J.H. acknowledges the
714 financial support from the China Scholarship Council (No. 202107990007). J.E. acknowledges the
715 financial support from the Institut Universitaire de France. Work at the Molecular Foundry was
716 supported by the Office of Science, Office of Basic Energy Sciences, of the U.S. Department of
717 Energy under Contract No. DE-AC02-05CH11231. T. K. acknowledges funding by the German
718 Science Foundation (DFG, fellowship number KO6414).

719

720 **Authors contributions:**

721 A.D.M., and J.E. conceived the idea, designed the experiments, analyzed the data, and cowrote
722 the manuscript. S.S., W.L., and I.M., designed experiments, analyzed the data and co-wrote the
723 manuscript. S.S. Fabricated devices, tested devices, performed templating experiments,
724 performed WAXS measurements, performed in-situ PL measurements, performed stability
725 experiments. I.M. Fabricated devices, tested devices, synthesized 2D crystals, performed WAXS
726 measurements, performed GIWAXS measurements, performed in-situ PL measurements. W.L.
727 and E.T. performed and analyzed the GIWAXS measurements. T.K. performed WAXS
728 measurements, performed in-situ PL measurements under the guidance of C.M.S-F. C.D. and
729 A.T. performed nano-XRD measurements and analyzed the data under the guidance from D.F.
730 M.K. performed the Dynamic Light Scattering of FAPbI₃ solutions under the guidance from
731 A.B.M. J. H. synthesized the 2D perovskite crystals. F.M., R.P., and R.G. fabricated devices,
732 tested devices and helped in performing the stability experiments. H.Z. Performed ex-situ optical
733 measurements with the help from A.T. I.A.M.P. performed and analyzed the ss-NMR
734 measurements under the guidance of G.N.M.R. A.B. performed the PES measurements for the
735 perovskite thin films under the guidance of M.G.K. M.A.A. analyzed device performance. C.K.
736 analyzed the structural properties of 2D and lattice mismatch between the 2D and 3D. D.G.
737 analyzed the optical spectroscopy measurements and contributed to editing the paper.

738

739

740 **Competing interests:** The authors declare no competing interests.

741 **Data and Materials Availability:** All (other) data needed to evaluate the conclusions in the
742 paper are present in the paper or the Supplementary Materials.

743

745 **Two-dimensional perovskite templates for durable**
746 **and efficient formamidinium perovskite solar cells**

747 Siraj Sidhik^{1,2#}, Isaac Metcalf^{1#}, Wenbin Li³, Tim Kodalle⁴, Connor Dolan⁵, Mohammad
748 Khalili², Jin Hou¹, Faiz Mandani², Andrew Torma³, Hao Zhang³, Jessica Persaud², Amanda
749 Marciel², Itzel Alejandra Muro Puentes⁶, G. N. Manjunatha Reddy⁶, Adam Balvanz⁷, Mohamad
750 A. Alam⁸, Claudine Katan⁹, Esther Tsai¹⁰, David Ginger¹¹, David Fenning⁵, Mercuri G.
751 Kanatzidis¹², Carolin M. Sutter-Fella⁴, Jacky Even^{13*} and Aditya D. Mohite^{1,2*}

752

753 **1. Methods and Characterization**

754 **1.1 High purity 2D perovskite powder synthesis**

755 We synthesized the 2D Ruddlesden-Popper perovskite parent crystals, $\text{BA}_2\text{FAPb}_2\text{I}_7$ by combining
756 the lead oxide (PbO, Sigma Aldrich, 99%), formamidinium hydrochloride (FACl, Sigma Aldrich,
757 $\geq 98\%$), and butylamine (BA, Sigma Aldrich, 99.5%) in precise stoichiometric ratios. This mixture
758 was dissolved in a solution of hydroiodic acid (HI, 57 wt% in H_2O) and hypophosphorous acid
759 (H_3PO_2 , 50% in H_2O) and stirred at a temperature of 240°C until complete dissolution of the
760 precursor materials and boiling of the solution occurred. Subsequently, the precursor solution was
761 allowed to cool down to room temperature, resulting in the crystallization of flat single crystals
762 with sizes ranging from micrometres to millimetres. To ensure the quality and phase purity of the
763 synthesized crystals, we performed a comprehensive analysis using a combination of X-ray
764 diffraction and absorbance measurements.

765 **1.2 Air-liquid interface method for single crystal growth of $\text{BA}_2\text{FAPb}_2\text{I}_7$**

766 To synthesize large-area 2D Ruddlesden-Popper perovskite crystals, $\text{BA}_2\text{FAPb}_2\text{I}_7$, we combine
767 lead oxide (PbO, Sigma Aldrich, 99%), formamidinium hydrochloride (FACl, Sigma Aldrich, $\geq 98\%$),
768 and butylamine (BA, Sigma Aldrich, 99.5%) in precise stoichiometric ratios. This mixture is
769 dissolved in a solution of hydroiodic acid (HI, 57 wt% in H_2O) and hypophosphorous acid (H_3PO_2 ,

770 50% in H₂O), and stirred at a temperature of 240°C until the precursor materials completely
771 dissolve and the solution begins to boil. Subsequently, the solution is kept at a temperature of
772 100°C without stirring. A clean glass is introduced at the bottom of the vial, allowing the large-
773 area crystals to form at the air-liquid interface. Once the crystal has formed, the glass is carefully
774 extracted from the vial using forceps, with the slightest movement aiding in scooping up the
775 formed crystals. The resulting film on the glass is washed with ether and annealed at a temperature
776 of 125°C to remove any trapped solvents in the crystals.

777 **1.3 Solar cell fabrication**

778 *Inverted planar perovskite solar cells:* The patterned glass/ITO substrates underwent a sequential
779 cleaning process involving ultrasonication in soap water, followed by deionized water, acetone,
780 and a mixture of acetone and ethanol (1:1), each for 15 minutes. After drying the substrates and
781 subjecting them to 30 minutes of UV-ozone cleaning, they were transferred to a glove box. Inside
782 the glove box, a hole-transporting layer (HTL) with a thickness of approximately 10 nm was
783 created using the SAMs layer (MeO-2PACz, TCI, America) at a concentration of 0.8 mg/ml in
784 Ethanol. The HTL was deposited by spin coating at 5000 rpm for 30 seconds, followed by
785 annealing at 100 °C for 10 minutes.

786 To prepare the FAPbI₃ perovskite precursor solution with a concentration of 1.0 M, the
787 PbI₂, and FAI, were mixed in a solvent mixture of DMF and DMSO (6:1). The solution was
788 continuously stirred for 4 h, following which various mol% of the formamidinium based 2D
789 perovskite, A₂FA_{n-1}Pb_nI_{3n+1}, where A⁺ stands for different bulky organic cations such as
790 butylammonium, and pentylammonium etc, was introduced and left for aging on the hot plate at
791 70°C for 30 min. A single-step spin coating process was employed to achieve a uniform coverage
792 of the perovskite film by spin coating the solution at 5000 rpm for 30 seconds with an acceleration

793 of 2500 rpm/s. The samples were subsequently annealed at 150 °C for 20 minutes. Lastly, the
794 devices were completed by thermal evaporation of C60 (30 nm), BCP (1 nm), and Copper (100
795 nm) under a vacuum of less than 2×10^{-6} torr. The active area selected for the devices was 0.5 cm².

796 **1.4 Optical absorbance and photoluminescence measurements**

797 *Thin film absorbance measurements:* Film absorbance measurements were carried out using a
798 setup that involved illuminating the samples with modulated monochromatic light at a frequency
799 of 2 kHz. The light was generated by a quartz-tungsten-halogen light source and passed through a
800 monochromator (SpectraPro HRS 300, Princeton Instruments). To detect the transmitted light,
801 synchronous detection was employed using a silicon photodiode connected to an SR865 lock-in
802 amplifier. The measurements were conducted in the spectral range of 400 – 800 nm, with a dwell
803 time of 0.1 s for each data point. Throughout the experiment, the samples were maintained under
804 vacuum conditions of approximately 10^{-4} torr and kept at room temperature.

805 *Steady-state photoluminescence measurements:* Thin-film photoluminescence (PL) measurements
806 were performed using a lab-built confocal microscopy system to acquire steady-state
807 photoluminescence (SS-PL) data. Spectra were collected using an Andor Kymera 329i
808 spectrometer and an Andor iDus 416 CCD detector. The acquired spectra were then processed
809 using Savitzky-Golay filtering for optimal signal-to-noise ratio. For photoexcitation, the samples
810 were illuminated with a monochromatic pulsed laser emitting at 2.58 eV (480 nm). The laser, with
811 a pulse duration of 6 ps and a repetition rate of 78.1 MHz, was focused near the diffraction limit,
812 achieving a resolution of approximately 0.5 μm. The excitation intensity was carefully adjusted to
813 360 W/cm². PL measurements were conducted in the spectral range of 450 - 900 nm with a dwell
814 time of 0.1 s. The experiments were performed under vacuum conditions (10^{-5} torr) at room
815 temperature. PL maps were acquired by scanning a region of either 40 μm x 40 μm or 100 μm x

816 100 μm , using a step size of 1 μm . At each step, the peak position of the photoluminescence signal
817 was extracted and recorded for further analysis.

818 **1.5 Time-resolved photoluminescence (TRPL) measurements**

819 Time resolved photoluminescence (TRPL) measurements were performed by exciting the samples
820 with various fluence laser pulse (420 nm, 40 fs pulse duration and 100 kHz repetition rate). These
821 laser pulses are generated by frequency doubling the laser pulse from diode-pumped Yb:KGW
822 femtosecond laser system (PHAROS) using barium-beta-borate crystal. This laser pulse (beam
823 spot size of 20 μm) was then focused onto sample with a 3.8 mm focal length lens. The emitted
824 light was then collected using a Mitutoyo objective lens (numerical aperture = 0.7, magnification
825 = 100 \times) from the transmission side and subsequently spatially filtered using a mechanical iris
826 located at the conjugate plane. Elastically scattered light was rejected by using a long pass filter
827 (wavelength 650 nm, optical density = 6.0). Additionally, bandpass filter centred at 800 nm
828 (wavelength = 800 \pm 20 nm, optical density = 4.0) was employed to filter the emitted light. The
829 emitted light was then focused onto the Micro Photon Device (MPD) PDM series single-photon
830 avalanche photodiode with an active area of 50 μm . The temporal resolution was set at a binning
831 size of 64 ps. Photoluminescence spectra were collected by directing the emitted light towards a
832 spectrometer using a flippable mirror.

833 **1.6 Ultrafast Transient absorption spectroscopy**

834 Time-resolved absorption (TA) data of the samples were obtained using transient femtosecond
835 pump-probe spectroscopy. The samples were excited by 420 nm laser pulse generated by using an
836 optical parametric amplifier having a pulse duration of 40 fs and a beam spot size of 120 μm .
837 Diode-pumped Yb: KGW femtosecond laser system based on the principle of chirped-pulse
838 amplification (PHAROS) produces light pulses centred at 840 nm. These laser pulses were then

839 passed through 0.5 mm thick barium-beta-borate crystal where the frequency will be doubled to
840 produce laser pulses centred at 420 nm acting as pump pulse. These laser pulses are focused on
841 the sample with a spot size of 120 μm in diameter ($1/e^2$). Another laser pulse from the amplifier is
842 focused onto a sapphire crystal to produce white-light supercontinuum that acts as a probe pulse.
843 The optical path length between pump and probe is manipulated by passing the probe beam
844 through a retroreflector mounted on high precision motorized translational stage. Probe pulse
845 (beam diameter 35 μm) was then focused and spatially overlapped with the pump pulse onto the
846 sample. It is then re-collimated and directed onto a multi-mode fibre for wavelength-sensitive
847 detection.

848 **1.7 X-ray diffraction measurements**

849 1D X-ray diffraction of the 3D perovskite thin films were measured in the 2θ between 2° and 30° ,
850 with a step of 0.01° and a speed of $2^\circ/\text{min}$, using a Rigaku SmartLab X-Ray diffractometer with
851 $\text{Cu}(K\alpha)$ radiation ($\lambda = 1.5406 \text{ \AA}$). For lattice parameter determination shown in **Figure 2E**, thin
852 films were scraped with a blade and wiped onto a glass slide to remove any residual strain from
853 the substrate. The scraped films were then coated with a thin film of PMMA to prevent $\alpha \rightarrow \delta$
854 conversion during XRD measurement in air.

855 Single crystal X-Ray diffraction of the 2D perovskite crystals was taken with a Rigaku Synergy-S
856 diffractometer using a Mo target. The temperature was held at 300K.

857 **1.8 Differential Scanning Calorimetry (DSC) measurements**

858 FAPbI_3 powders for DSC were prepared by spin-coating $300\mu\text{L}$ of FAPbI_3 precursor solution onto
859 a large-area (25cm^2) substrate, drying at room temperature under vacuum, and scraping with a
860 blade. DSC was performed using a TA DSC 250 with a scan rate of $1^\circ\text{C}/\text{min}$.

861 **1.9 Nuclear Magnetic Resonance (NMR) measurements**

862 FAPbI₃ powders for NMR were prepared by spin-coating 300 μ L of FAPbI₃ precursor solution
863 onto a large-area (25cm²) substrate, annealing, and scraping with a blade. Powders were dissolved
864 in 600 μ L of deuterated DMSO. ¹H NMR was performed on a 600 MHz Bruker NEO Digital NMR
865 Spectrometer. For ¹H NMR a higher BA n=2 concentration of 5 mol% was employed to better
866 resolve the butylammonium signal. For solid-state NMR measurements, thin films of control 2D
867 and 2D-doped FAPbI₃ were deposited on glass substrates, scraped with a blade, and collected as a
868 powder. To minimize the material degradation during solid-state NMR data collection, the
869 materials were separately packed into air-tight and opaque zirconia rotors (1.3 mm, outer diameter)
870 fitted with VESPEL caps. All ex-situ solid-state MAS NMR experiments were conducted at 21.1
871 T (Larmor frequency ¹H = 900 MHz). The MAS frequency was 50 kHz in all ssNMR experiments.
872 ¹D 1H MAS NMR spectra were acquired by co-addition of 16 transients. An interscan delay was
873 set to 45 s, as determined from saturation recovery measurements and analyses, to ensure the full
874 *T*₁ relaxation and hence the quantitative proton peak intensities. 2D ¹H-¹H spin diffusion NMR
875 experiments were acquired using a three-pulse NOESY-like sequence with 500 μ s of mixing time
876 for the α -FAPbI₃-low dimensional phase (BA or PA). A rotor-synchronized increment of 20 μ s
877 was applied to detect 400 *T*₁ increments, each with 2 co-added transients. For all materials, the ¹H
878 experimental shift was calibrated with respect to neat TMS using adamantane as an external
879 reference (¹H resonance, 1.81 ppm).

880 From 1D ¹H ssNMR spectra of precursor compounds, control 2D materials and 2D-doped
881 FAPbI₃ materials (**Figure S15A-B**), the ¹H peaks corresponding to the different organic cations
882 can be identified and distinguished. For reference, the ¹H signals of the FA⁺ is attained (blue boxes),
883 and BA⁺ signals in the BA-stabilized perovskite can be found in the orange box, and BA⁺ signals
884 in the BA-stabilized perovskite are presented in the purple box. The origin of these signals is

885 further corroborated by acquiring the ^1H ssNMR spectra of neat 2D $\text{BA}_2\text{FAPb}_2\text{I}_7$ and $\text{PA}_2\text{FAPb}_2\text{I}_7$
886 phases. The comparison of the ^1H peak integrals associated with the of FA^+ and BA^+ suggests that
887 there is ~ 7.9 mol% of 2D phase present in the 3D phase, which is estimated to be ~ 7.9 mol% for
888 the 2D $\text{PA}_2\text{FAPb}_2\text{I}_7$ doped material.

889 To gain insights into the local proximities between the BA cations and the FA cations in
890 the 2D $\text{BA}_2\text{FAPb}_2\text{I}_7$ / $\text{PA}_2\text{FAPb}_2\text{I}_7$ doped FAPbI_3 phases, 2D ^1H - ^1H spin-diffusion (SD) NMR
891 experiments were carried out and analyzed. Specifically, magnetization exchange between dipolar
892 coupled spins (here protons) allows the through-space proximities between neighboring sites, for
893 example, information on through-space ^1H - ^1H proximities in different organic cations to be probed.
894 In 2D ^1H - ^1H SD spectra, the on-diagonal peaks provide information on chemical shifts and the off-
895 diagonal peaks contain information on spin magnetization exchange between chemically
896 inequivalent spins. For both BA and PA-stabilized 3D phases, a mixing delay of 50 μs was
897 insufficient to produce off-diagonal peaks, but a mixing delay of 500 μs leads to the magnetization
898 exchange between the ^1H sites in in BA^+ , FA^+ and between BA^+/FA^+ and PA^+/FA^+ as seen in green
899 and gray boxes, respectively (**Figure S15E-F**). These peaks indicate the coexistence of a mixed
900 2D/3D phase. Relatively strong intensity peaks observed for the BA-stabilized FAPbI_3 phase
901 suggesting that the high degree of mixing of 2D phase within the 3D phase, as compare to the PA-
902 stabilized FAPbI_3 . In addition, the peaks with in the purple and orange boxes indicate the close
903 proximities between the proton sites within PA and BA cations respectively.

904

905 **1.10 Time-of-Flight Secondary Ion Mass Spectrometry (ToF-SIMS) measurements**

906 Positive high mass resolution depth profiles were conducted using a combined TOF-SIMS NCS
907 instrument, which integrates a TOF.SIMS instrument (ION-TOF GmbH, Münster, Germany) and

908 an in-situ Scanning Probe Microscope (NanoScan, Switzerland) at the Shared Equipment
909 Authority from Rice University. The analysis field of view covered an area of $80 \times 80 \mu\text{m}^2$ (Bi^{3+}
910 at 30 keV, 0.35 pA) with a raster of 128 x 128 during the depth profile. To compensate for charge
911 effects, an electron flood gun was employed throughout the analysis. The charge effects were
912 adjusted using a surface potential of -36V and an extraction bias of 0V.

913 The cycle times were set at 90 μs , corresponding to a mass range of $m/z = 0 - 735$ a.m.u.
914 During sputtering, a raster of $450 \times 450 \mu\text{m}^2$ was used (Cs^+ @ 1 keV, 44 nA). The beams operated
915 in a non-interlaced mode, alternating between 1 analysis cycle and 1 frame of sputtering (taking
916 approximately 1.31s), followed by a 2-second pause for charge compensation. To enhance the
917 understanding of the data, MCs^{n+} ($n = 1, 2$) depth profiling was also employed. This method is
918 particularly useful for quantifying alloys and identifying ion compounds. The cesium primary
919 beam was utilized for sputtering during the depth profile, enabling the detection of MCs^+ or MCs^{2+}
920 cluster ions, where M represents the element of interest combined with one or two Cs atoms. The
921 use of MCs^+ and MCs^{2+} ions in ToF-SIMS analysis offers several advantages, including the
922 reduction of matrix effects and the ability to detect compounds containing both electronegative
923 and electropositive elements. All depth profiles were point-to-point normalized based on the total
924 ion intensity, and the data were plotted using a 5-point adjacent averaging. The normalization and
925 smoothing techniques facilitated a better comparison of the data obtained from different samples.
926 Depth calibrations were established by measuring the thicknesses using a surface profiler, which
927 generated a line scan of the craters using in-situ SPM through contact scanning.

928 **1.11 In-situ WAXS measurements for FAPbI_3 film formation**

929 The experimental setup took place in a custom-made analytical chamber located at the
930 12.3.2 microdiffraction beamline of the Advanced Light Source. This specialized chamber was

931 designed to accommodate various measurements and processes simultaneously, including the
932 handling of thin films. The indium-doped tin oxide substrate, which had been cleaned using plasma,
933 was securely positioned on the integrated spin coating puck-heater and affixed with a heat transfer
934 paste. To initiate the deposition process, a liquid precursor containing 1 M PbI_2 and
935 formamidinium in a solvent mixture of 6:1 DMF:DMSO was carefully pipetted onto the substrate's
936 surface. To maintain a controlled environment, the chamber was sealed off from the external
937 surroundings and kept under a continuous nitrogen flow. The experiment proceeded by subjecting
938 the precursor to spin coating, which involved two steps: the first spin coating was carried out at
939 4000 rpm for 30 s to create a thin film. During the second spin coating step, precisely 10 s into the
940 process, a remotely controlled pipette dispensed a stream of ethyl acetate.

941 After the completion of the spin coating protocol, a remote heating protocol was initiated.
942 A nonlinear stepwise annealing sequence was applied, in which the substrate temperature was
943 increased by steps of 20°C in 20 sec intervals up to 100°C and then increased by steps of 25°C up
944 to 150°C . The temperature was then maintained at 150°C for the duration of the experiment, which
945 lasted until $t = 300$ s. The incident X-ray beam was directed at an incidence angle of 1° with a beam
946 energy of 10 keV. The distance between the sample and detector, known as the sample detector
947 distance (SDD), was approximately 155 mm. The detector itself was positioned at an angle of 39°
948 relative to the sample plane. WAXS (wide-angle X-ray scattering) data were acquired with an
949 exposure time of 1.0 s and an additional pause of 0.8 s (total 1.8 s) between measurements using a
950 2D Pilatus 1 M detector (Dectris Ltd.). Photoluminescence excitation was achieved by utilizing a
951 532 nm Thorlabs diode-pumped solid-state laser with a power density of 40 mW/cm^2 . The
952 resulting photoluminescence signal was collected by a lens, directed into an optical fiber, and
953 transmitted to a grating OceanOptics QE Pro spectrometer for detection. To regulate the annealing

954 temperature and protocol, a pre-calibrated Raytek MI3 pyrometer recorded the temperature of the
955 heating puck. The temperature control system utilized a pre-programmed PID loop.

956 *Calibration of peak positions during heating:* The heat transfer paste holding the substrate is
957 known to expand with temperature, changing the height of the substrate slightly. A change in
958 height also changes the sample-detector distance and the direct beam position with respect to the
959 detector, giving the illusion that peaks are shifting towards higher q -values as temperature
960 increases. It is best practice to correct for this height change over the temperature ramping with
961 regards to the principal ITO peak at $q = 2.15 \text{ \AA}^{-1}$. However, this peak overlaps with the (112)
962 diffraction peak from the FAPbI₃ δ – phase, which emerges once the antisolvent is deposited and
963 persists during temperature ramping. Instead, we compared the position of the principal ITO peak
964 at room temperature before antisolvent dropping with its position at 150°C after the δ – phase had
965 converted to α – phase. We assumed a linear relation between temperature and change in substrate
966 height, which allowed us to use the in-situ temperature data to correct for this peak shift during
967 temperature ramping.

968

969 **1.12 Dynamic Light Scattering (DLS) measurements**

970 *Experimental methods:* The solutions of FAPbI₃+ BA₂FAPb₂I₇ perovskites were prepared by
971 dissolving precursors and high purity crystal powders in DMF as described in section S1.3 and
972 adding 5 and 10 mg of n=2 BA₂FAPb₂I₇. The prepared solutions were loaded into cylindrical glass
973 cuvettes (Wilmad® NMR tubes 5 mm diam., high throughput. 103 mm length). Dynamic Light
974 Scattering (DLS) measurements were performed immediately by capturing correlation curves at
975 four different angles: 60°, 90°, 120°, and 150°. The measurements were conducted at an ambient

976 temperature of 20°C using a fully automated 3D LS Spectrometer (LASER: 660 nm, 65 mW, LS
977 Instruments AG, Fribourg). Each angle was measured in triplets.

978 *Extraction of the size of the particles in solution:* Below is a detailed description of the analysis
979 conducted on the multi-angle Dynamic Light Scattering (DLS) data obtained from various
980 concentrations of precursor solutions. The autocorrelation curves were measured for each solution
981 to examine their angular dependence. These correlation curves were then fitted using a single-
982 exponential decay model. The residuals resulting from the correlation fitting were measured and
983 plotted. Furthermore, a linear regression of Γ versus q^2 was performed, focusing on the range
984 between 60° and 150°. The scattered light correlation function, $g^{(2)}$, compares the intensity of
985 received signal between time t and later time $t+\tau$,⁽⁵⁾

$$986 \quad g^{(2)}(q, \tau) = \frac{\langle I(t)I(t+\tau) \rangle}{\langle I(t) \rangle^2} \quad (2)$$

987 Using the Siegert relationship that relates the field correlation function and intensity correlation
988 function given by⁽⁶⁾

$$989 \quad g^{(2)}(q, \tau) - 1 = \beta |g^{(1)}(q, \tau)|^2 \quad (3)$$

990 where β is a constant proportional to the signal-to-noise ratio.

991 For a system undergoing Brownian motion the electric field correlation function is shown to decay
992 exponentially as

$$993 \quad g^{(1)}(q, \tau) = \exp(-\Gamma\tau) \quad (4)$$

994 When several groups of particles with different sizes (labelled i) are present in solution, the DLS
995 data can be fitted using⁽⁶⁾:

996
$$g^{(2)}(q, \tau) - 1 = \sum_i \alpha_i \left| g_i^{(1)}(q, \tau) \right|^2 = \sum_i \alpha_i \exp(-\Gamma_i \tau)^2 \quad (5)$$

997 Then, for the group of particles i the value Γ_i is related to the translational diffusion coefficient
 998 $D_{T,i}$ and wave number q through.

999
$$\Gamma_i = D_{T,i} q^2 \quad (6)$$

1000 with,

1001
$$q = \frac{4\pi\eta}{\lambda} \sin\left(\frac{\theta}{2}\right) \quad (7)$$

1002 η is the refractive index of the solvent, λ is the wavelength of the laser, and θ the angle between
 1003 the incident laser beam and the scattered light. Finally, the diffusion coefficient is related to the
 1004 hydrodynamic radius R_H of particles in a Brownian motion by the Stokes-Einstein equation(7)

1005
$$D_{T,i} = \frac{k_B T}{6\pi\mu R_{H,i}} \quad (8)$$

1006 with k_B is the Boltzmann constant, T the temperature, μ the dynamic viscosity, and $R_{H,i}$ the
 1007 median hydrodynamic radius of the group i of particles.

1008 **1.13 Nano X-Ray diffraction measurements.**

1009 Nano X-ray Diffraction measurements were taken at the hard X-ray nanoprobe at Sector
 1010 26 ID-C of the Advanced Photon Source at Argonne National Laboratory. Samples were fabricated
 1011 on X-ray transparent silicon nitride (Norcada, part no. NX5050D) windows for measurement in
 1012 transmission geometry, enabling measurements at near-normal incidence and minimizing beam
 1013 projection on the sample surface. Measurements were taken at 9.6 keV incident X-ray energy using
 1014 an X-ray probe with a full width at half maximum of approximately 25 nm focused using a Fresnel
 1015 zone plate and order-sorting aperture to minimize the probe broadening contribution of higher

1016 order diffraction. Diffraction patterns were collected with a zero-noise diffraction CCD.
1017 Diffraction patterns were recorded using a Dectris Eiger2 single photon counting detector with 75
1018 μm pixel width and angular resolution ranging from $0.018\text{-}0.023^\circ$ per pixel at low and high two
1019 theta, respectively. Dwell times of 0.1 s per point were used to generate nano-diffraction maps.
1020 The X-ray diffraction pattern remained consistent for many seconds of X-ray irradiation at a single
1021 point, as determined by measuring X-ray diffraction patterns over time for all samples (**Figure**
1022 **S17**).

1023 **1.14 Grazing incidence wide angle X-ray scattering**

1024 *Experimental methods:* The GIWAXS (grazing-incidence wide-angle X-ray scattering)
1025 measurements presented in this paper were conducted at two different synchrotron beamlines: 8-
1026 ID-E at the Advanced Photon Source (APS) and 11-BM at the National Synchrotron Light Source-
1027 II (NSLS II). For experiments performed at beamline 8-ID-E, the samples were positioned on a
1028 specialized Linkam grazing incidence x-ray-scattering (GIXS) stage placed inside a vacuum
1029 chamber with a pressure of 10^{-4} torr. The Pilatus 1M (Dectris) area detector was situated
1030 approximately 228 mm away from the sample. A photon energy of 10.91 keV was employed, and
1031 the X-ray beam had a size of $200\ \mu\text{m} \times 20\ \mu\text{m}$ (horizontal \times vertical). On the other hand,
1032 experiments at beamline 11-BM utilized a robotic stage within a vacuum chamber maintained at a
1033 pressure of 6×10^{-2} torr. The sample-to-detector distance was approximately 267 mm, and the
1034 Pilatus 800K (Dectris) area detector was employed. The photon energy used was 13.5 keV, and
1035 the X-ray beam had dimensions of $200\ \mu\text{m} \times 50\ \mu\text{m}$ (horizontal \times vertical).

1036 In-situ GIWAXS during degradation was performed using a solvent vapor annealing
1037 chamber in the open sample staging area at 11-BM. The measurement beam entered and exited
1038 the chamber through Kapton windows on either side. For high-humidity measurements, liquid

1039 water was added to the bottom of the chamber to fix the atmosphere at >90%RH. For illuminated
1040 measurements, AM1.5G light entered the chamber from the top through a glass window. For
1041 heated measurements, a resistive heating element below the sample controlled the chamber
1042 temperature.

1043 *GIWAXS analysis:* To analyze the GIWAXS patterns, a full angular integration was conducted to
1044 obtain a 1-D X-ray spectrum. The Debye-Scherrer formula was employed to determine the average
1045 grain size (D_{hkl}) of the perovskite thin film, where (hkl) represents the Miller indices. For the
1046 analysis of the 2D perovskite top film, the (200) plane was utilized, while the (001) plane was
1047 selected for the 3D perovskite film. The Scherrer equation incorporated a shape factor (K) of 0.9.
1048 The formula is presented as follows:

$$1049 \quad D_{hkl} = \frac{K\lambda}{\beta_{hkl} \cos \theta_{hkl}} \quad (1)$$

1050 where λ is 1.1365 Å and is the X-ray wavelength, θ is the diffraction peak position, β is the full-
1051 with-at-half-max (FWHM). The FWHM was extracted by fitting the diffraction profile to a
1052 pseudo-Voigt function. The FWHM was correct for the geometry of the measurement such as the
1053 X-ray beam divergence, energy bandwidth, and the parallax effect of the beam footprint.

1054 **1.15 Thin-film morphology measurements**

1055 *Scanning electron microscopy (SEM) measurements:* The surficial and cross-sectional SEM
1056 images were acquired using the FEI Quanta 400 ESEM FEG instrument. The fabrication process
1057 involved depositing the 3D control and the 2D templated 3D perovskite films onto a Silicon
1058 substrate, followed by sputtering approximately 15 nm of gold to improve film conductivity. The
1059 SEM images were captured at a voltage of 12.5 kV, and a dwell time of 30 μs was utilized during
1060 image acquisition.

1061 *Atomic force microscopy (AFM) measurements:* The AFM measurements were conducted utilizing
1062 the NX20 AFM instrument from Park Systems. Surface topographical images were acquired in
1063 tapping mode, employing a silicon tip with a resonant frequency of 300 kHz and a spring constant
1064 of 26 N/m. The root mean square (RMS) roughness values were extracted from a $5\mu\text{m} \times 5\mu\text{m}$
1065 image.

1066 **1.16 Determination of electronic band levels using Photoemission yield spectroscopy (PES)**

1067 PES (AC-2, Riken-Keiki) measurements were conducted to determine the valence band maximum
1068 (VBM) of the 3D, 2D ($\text{BA}_2\text{FAPb}_2\text{I}_7$) templated 3D perovskite samples. The measurements were
1069 performed under ambient conditions, with the samples being illuminated by monochromatic
1070 ultraviolet (UV) light. The UV photons used had energy levels exceeding the ionization energy
1071 (IE) of the sample being measured. These photons caused the ionization of an electron to the
1072 vacuum level, which, in turn, ionized a gas molecule in proximity to the surface, as detected by
1073 the instrument. During the measurement, the energy of the photons ranged from 4.2 eV to 6.2 eV,
1074 and the number of generated photoelectrons was recorded for each energy level. This recorded
1075 value was corrected based on the intensity spectrum of the UV lamp used. For semiconductors,
1076 the number of photo-generated electrons near the VBM typically increases as the cube root of the
1077 energy. Therefore, the cube root of the corrected PYSA spectrum was plotted against the photon
1078 energy. The linear region of the plot above the onset was fitted to determine the VBM, which was
1079 identified at the crossing point between the linear fit and the background level. To calculate the
1080 conduction band minimum (CBM) relative to the vacuum level, the measured bandgap was
1081 subtracted from the ionization energy, resulting in the electron affinity (EA).

1082 **1.17 Characterization of solar cell devices**

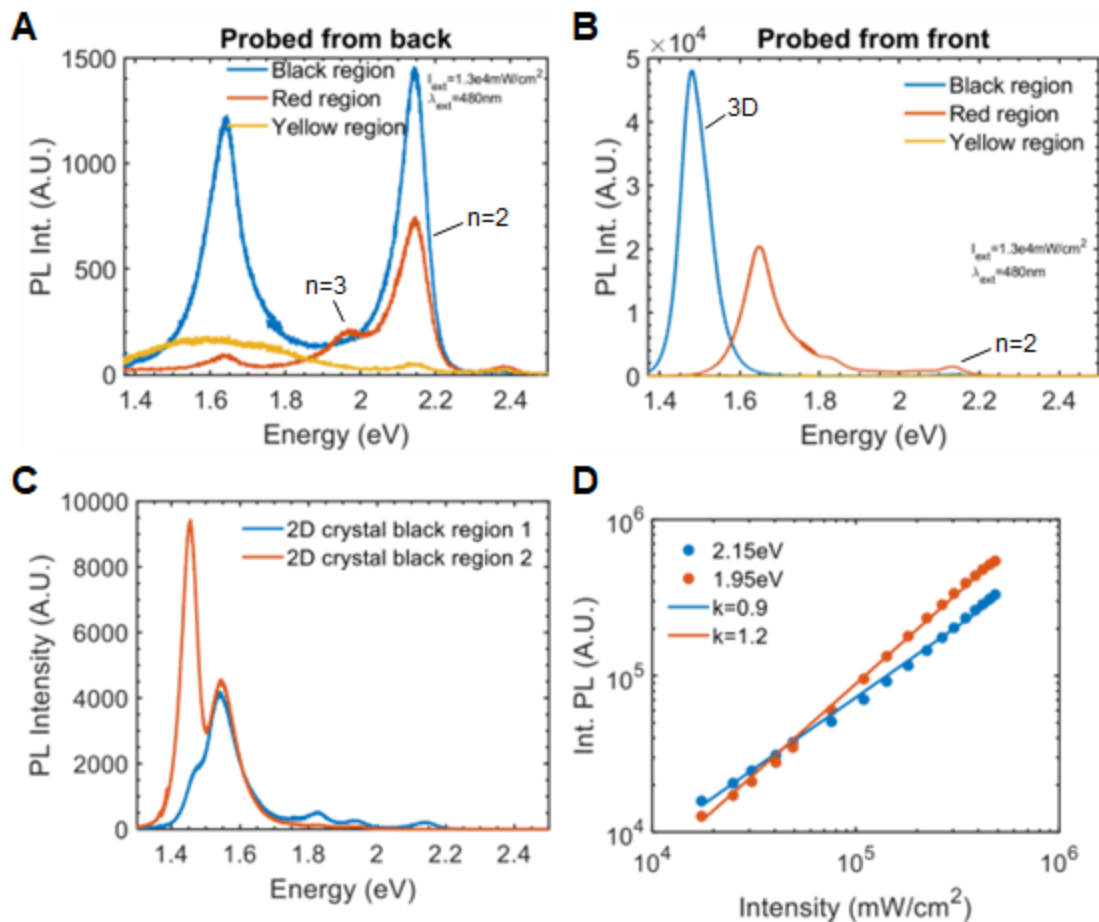
1083 *Solar cell performances:* The performances of the solar cells were obtained by measuring the
1084 current-voltage (J-V) curves of each device illuminated by an ABB solar simulator from Newport
1085 (model 94011). The arc simulator modelled AM 1.5G irradiance of 100 mW/cm^2 whose intensity
1086 was calibrated using a NIST-certified Si solar cell (Newport 91150V, ISO 17025) and corrected
1087 by measuring the spectral mismatch between the solar spectrum, reference cell, and the spectral
1088 response of the PV device. We estimate a mismatch factor of 3%. The solar cells were measured
1089 with a Keithley 2401 instrument from 1.2 to 0 V and back, with a step size of 0.05 V and a dwell
1090 time of 0.1 s, after light soaking for 10 s. The defined active area was 3.14 mm^2 .

1091 *External quantum efficiency:* The external quantum efficiency (EQE) of the solar cell devices was
1092 collected by first illuminating each device with monochromatic light modulated at 2 kHz coming
1093 from a quartz-tungsten-halogen light source fed into a monochromator (SpectraPro HRS 300,
1094 Princeton instruments). The photocurrent response of the solar cells was measured by an SR865
1095 lock-in amplifier. The light source spectrum response was calibrated using a calibrated silicon
1096 diode (FDS1010, Thorlabs).

1097 *Stability tests:* For stability test measurements, the perovskite devices were encapsulated with a
1098 UV- curable epoxy (Poland Inc.) and a glass coverslip as a barrier layer in an argon-filled glove
1099 box. The devices were blown with the argon gun to remove any contaminants or dust particles just
1100 before encapsulation. All the devices were tested at the continuous maximum power point
1101 condition, under full-spectrum simulated AM 1.5G (100 mA cm^{-2} irradiance) in the air using an
1102 ABB solar simulator (94011A, Newport) – ISOS-L1 protocol. Each data point was collected after
1103 an interval of 15 min. The relative humidity was measured to be constant at $60 \pm 5 \% \text{RH}$.

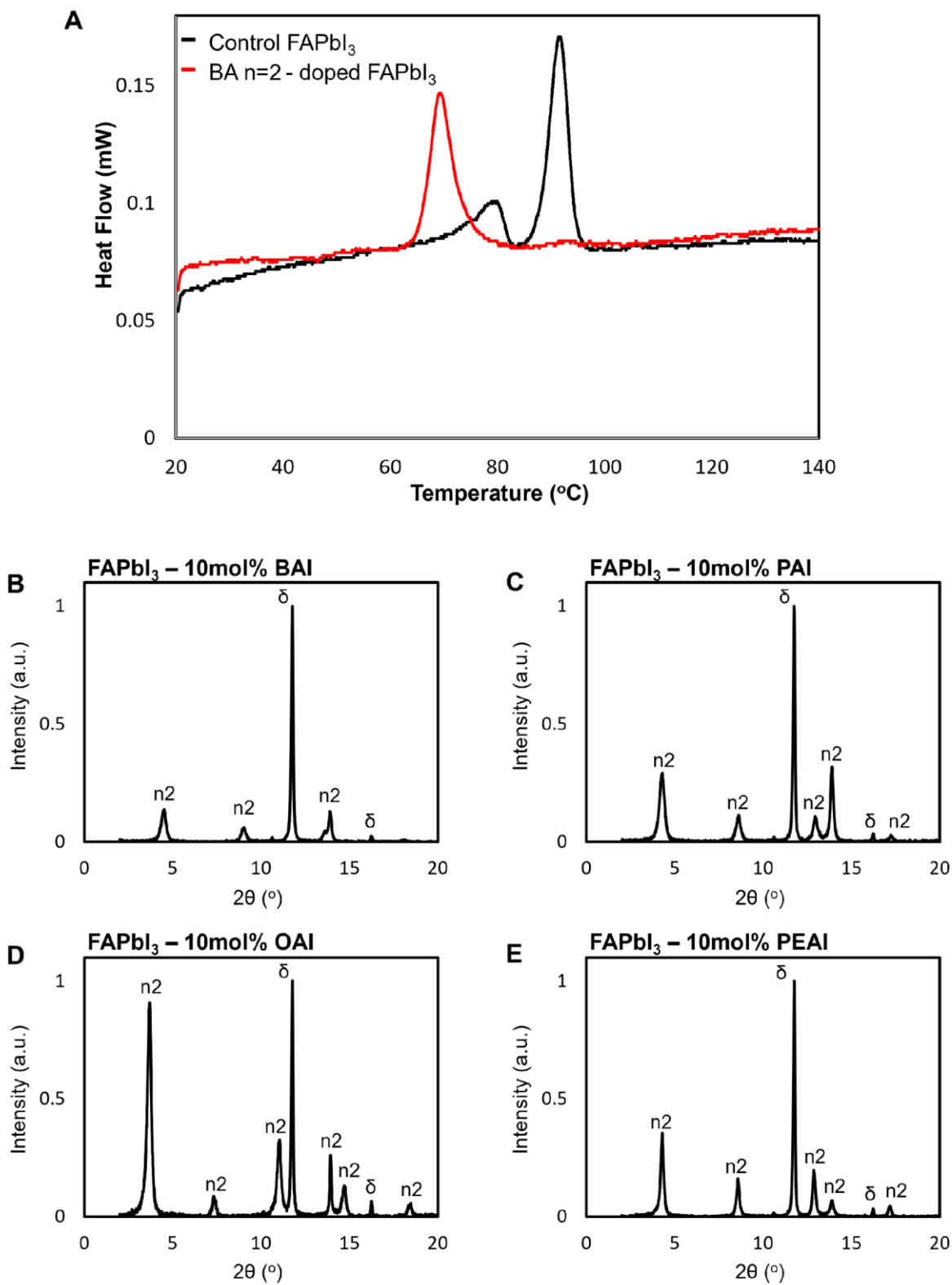
1104 **1.18 Mechanism of 3D FAPbI₃ formation.**

1105 In our synthesis methodology, we dispersed selective 2D perovskite crystals ($\text{BA}_2\text{FAPb}_2\text{I}_7$) in a
1106 FAPbI_3 solution containing $\text{FAI}:\text{PbI}_2$ (1:1) dissolved in a DMF: DMSO solvent. Subsequently, we
1107 observed sub-micrometer-sized crystallites, referred to as "memory seeds," which retained their
1108 perovskite structure and acted as nucleation sites during film formation (Fig. S14) (41). Upon spin
1109 coating, these memory seeds transferred their n-value to the solution-processed films which
1110 comprises of 2D perovskite ($\text{BA}_2\text{FAPb}_2\text{I}_7$) alongside the δ -phase of FAPbI_3 (**Fig. 2E, Step i**).
1111 During annealing, we propose that the transformation to bulk FAPbI_3 occurs through an
1112 intercalation process (**Fig. 2E, Step ii**). Ions such as FA^+ , Pb^{2+} , and I^- permeate the lattice from the
1113 edges of the 2D-HaP crystal, diffusing along the interface between the perovskite layers. These
1114 ions fill voids in the corner-sharing PbI_6 structure, forming additional linkages and integrating with
1115 the $[\text{Pb}_n\text{I}_{3n+1}]$ lattice to form the 3D bulk FAPbI_3 pushing the bulky organic cations to the grain
1116 boundaries (**Fig. 2E, Step iii**). The observed templating effect is attributed to the delicate ionic
1117 interactions between the 2D inorganic octahedral sheets and the organic spacers, coupled with the
1118 lattice matching between the 2D perovskite ($\text{BA}_2\text{FAPb}_2\text{I}_7$) and the 3D FAPbI_3 lattice planes. Our
1119 results are consistent with the previous reports that observe the intercalation of precursor ions into
1120 the lattice to form higher layer thickness 2D-HaP (44).



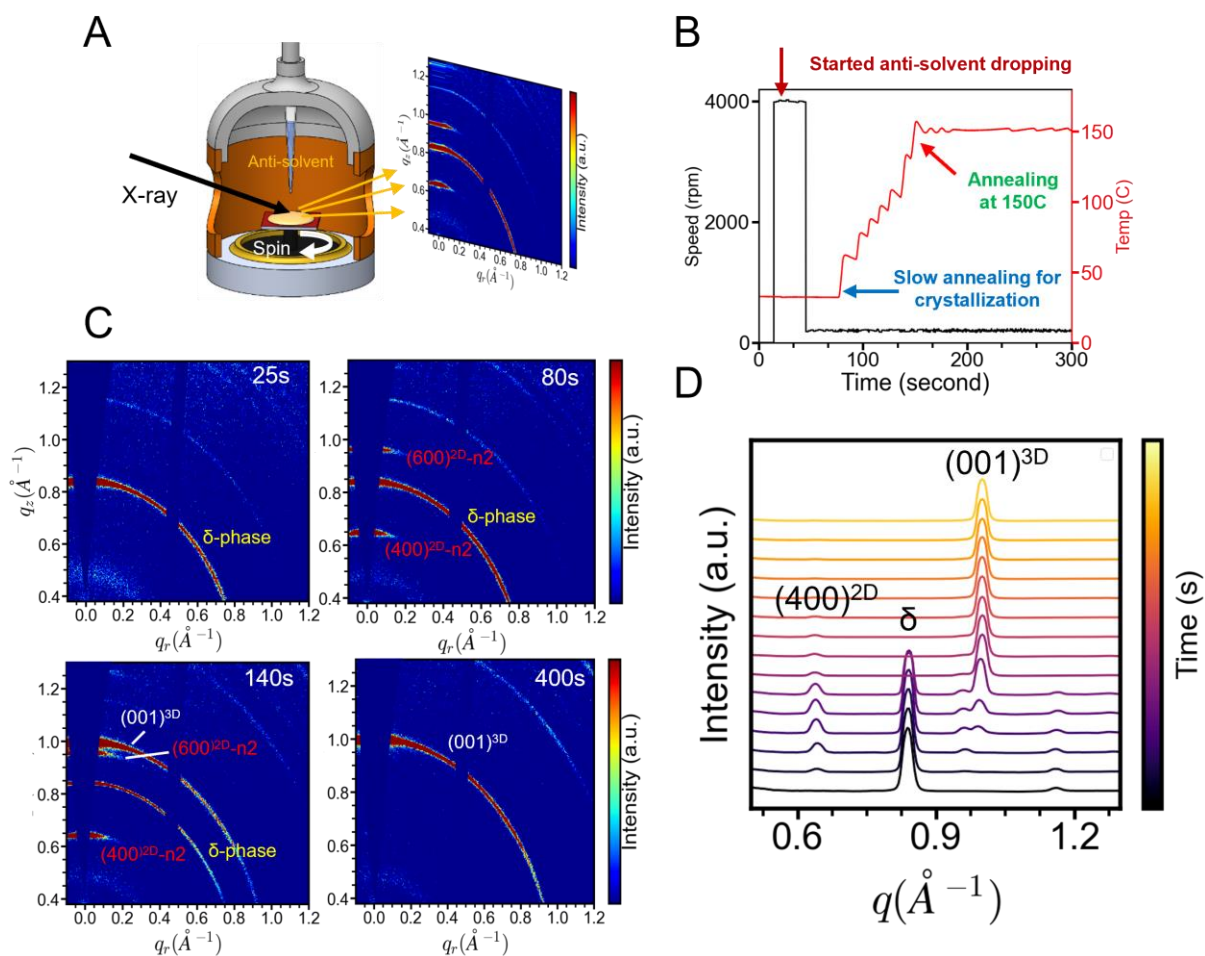
1121
 1122
 1123
 1124
 1125
 1126
 1127
 1128
 1129
 1130
 1131
 1132
 1133
 1134
 1135

Fig. S1. Photoluminescence characterization of templated FAPbI₃ on BA₂FAPb₂I₇ single crystal. Photoluminescence of the 3 different regions on the templated FAPbI₃ drop-coating experiment from the back and the front (A and B, respectively). The red region is depicted as region (i) in **Figure 1D** and was the unexposed FAPbI₃ solution area of the BA₂FAPb₂I₇ single crystal. The black region is depicted as region (ii) in **Figure 1D** and was the edge of the BA₂FAPb₂I₇ single crystal that was in contact with the FAPbI₃ solution. The yellow region (region (iii) in **Figure 1D**) corresponds to the opposite edge of the sample where the FAPbI₃ sample is on glass. **C.** PL spectra of two different regions, one of which (region 1) is on top of the 2D crystal and the other (region 2) where there is no 2D crystal. **D.** Integrated PL peaks as a function of probe intensity for the n=2 and (hypothesized) n=3 excitonic peak (blue and red, respectively). The log-log linear fit constants are shown in the legend as the slope k.



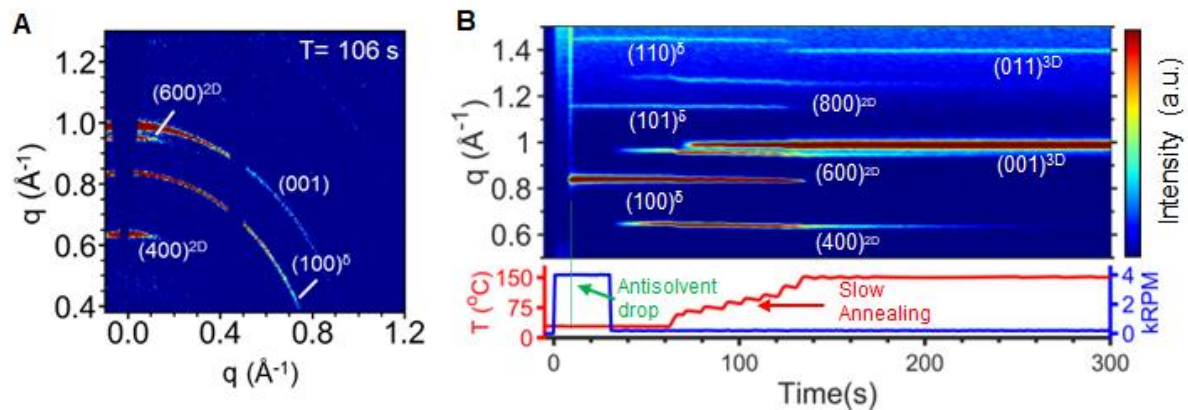
1136
1137 **Fig. S2. Demonstrating the viability of 2D stabilization.** A. Differential Scanning Calorimetry
1138 of a scraped FAPbI₃ film before annealing, with 2 mol% BA n=2 dopant (red) compared to without
1139 (black) showing $\delta \rightarrow \alpha$ conversion at lower temperature for 2D-doped FAPbI₃. B – E. 1D XRD of

1140 films of spin-coated FAPbI₃ solution doped with 10mol% A' iodide salt, annealed for 5 min at
 1141 70°C. **B.** BAI, **C.** PAI, **D.** OAI, **E.** PEAI. In each case the A'I precipitates as phase-pure
 1142 A'₂FAPb₂I₇.



1143 **Fig. S3. In-situ structural probe during thin-film formation for 1.0 mol% BA₂FAPb₂I₇ doped**
 1144 **FAPbI₃.** **A.** Schematic of the in-situ wide-angle-x-ray-scattering experiment during film formation
 1145 and an example of diffraction pattern obtain during measurement. **B.** An example of the
 1146 experimental logs which track the spin-coating speed and temperature of the spin-coater hotplate
 1147 during the measurement. The critical steps during the film-formation are noted on the plot such
 1148 as the anti-solvent dropping, the time at which the annealing starts and the 150°C annealing. **C.**
 1149 The corresponding WAXS diffraction patterns obtain during the measurement at critical times
 1150 (noted on the top right). The Bragg diffraction planes for the 2D, α - and δ -phase are denoted on
 1151 the plot in red, white, and yellow, respectively. **D.** The corresponding time evolution of the
 1152 diffraction pattern during the thin-film formation.

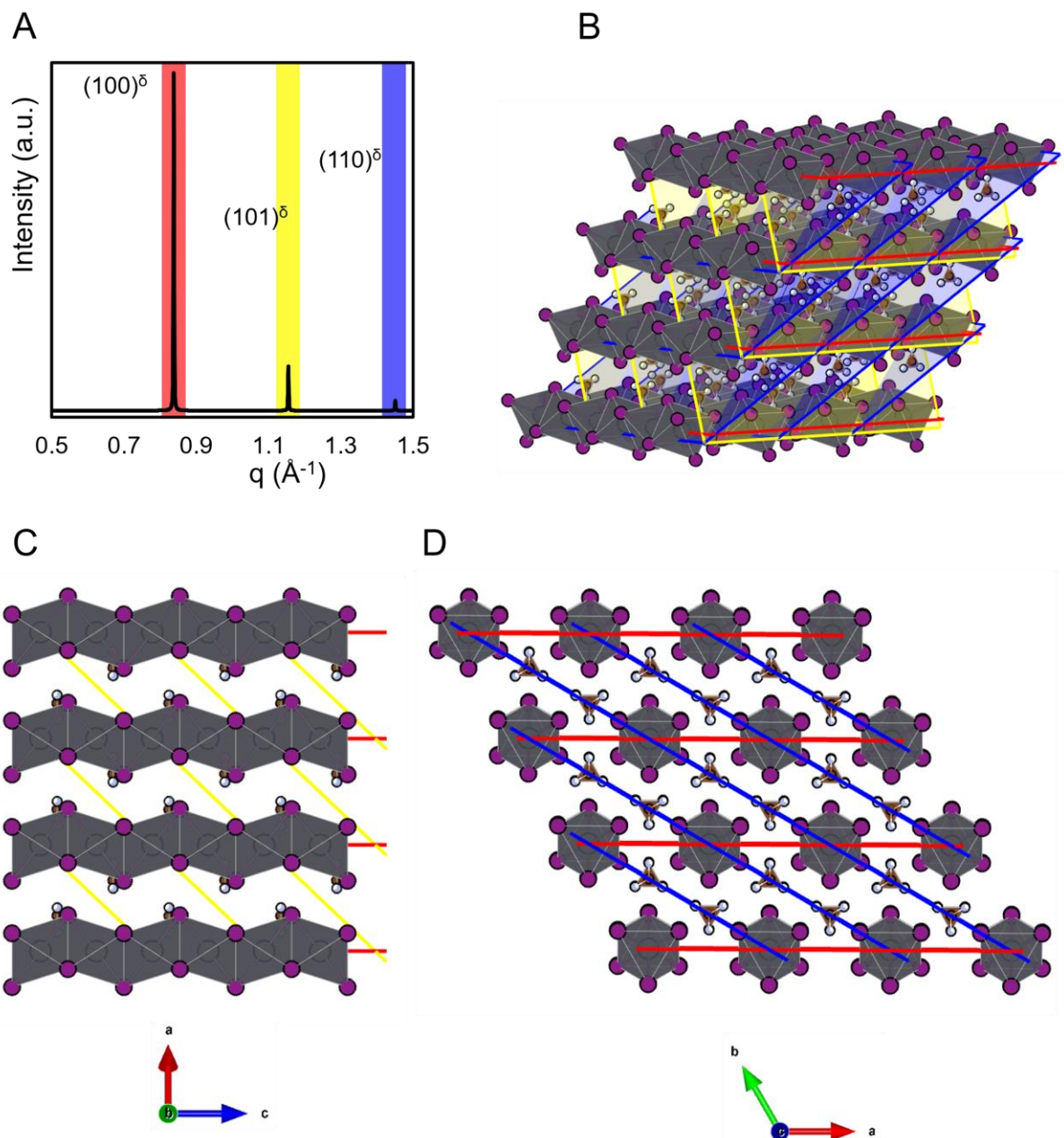
1154
 1155
 1156
 1157
 1158
 1159



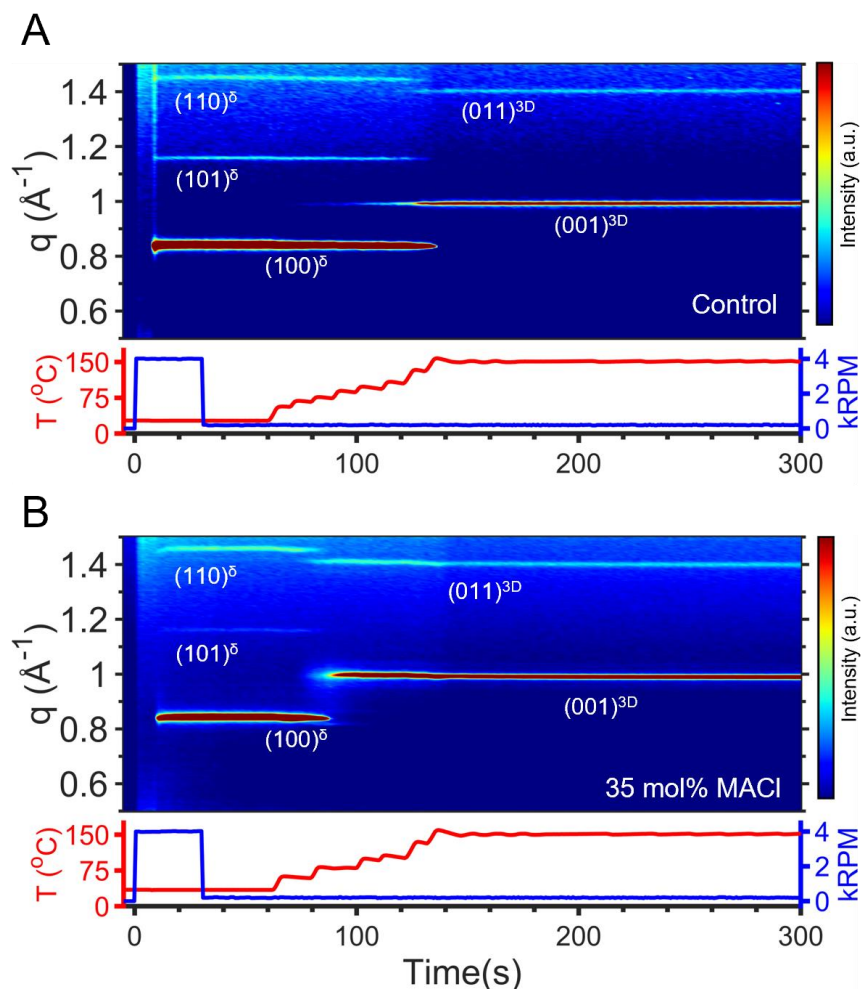
1160
 1161 **Fig. S4.** **A)** WAXS pattern taken during thin-film formation showing the coexistence of δ -FAPbI₃,
 1162 α -FAPbI₃, and BA₂FAPb₂I₇ diffraction peaks. **B)** Azimuthally integrated WAXS pattern over time
 1163 during in-situ spin-coating of a FAPbI₃ precursor solution with 1.0 mol% BA n=2.

1164
 1165
 1166
 1167
 1168
 1169

1170



1171
 1172 **Fig. S5. Diffraction planes in the δ -FAPbI₃ structure.** A. Simulated diffraction pattern for δ -
 1173 FAPbI₃ showing the three lowest-angle diffraction peaks: (100) (red), (101) (yellow, and (110)
 1174 (blue). B. The δ -FAPbI₃ structure with (100) (red), (101) (yellow, and (110) (blue) planes indicated.
 1175 The structure is also shown along the b-axis (C.) and the c-axis (D.).
 1176



1177 **Fig. S6. A-B.** Contour plot of the in-situ WAXS measurement for the fabrication of (A.) control-
 1178 FAPbI₃ and (B.) FAPbI₃ doped with 35 mol% methylammonium chloride. Illustrated on the
 1179 contour plots are Miller indices for the α (3D) and δ phases.
 1180
 1181

1182

1183

1184

1185

1186

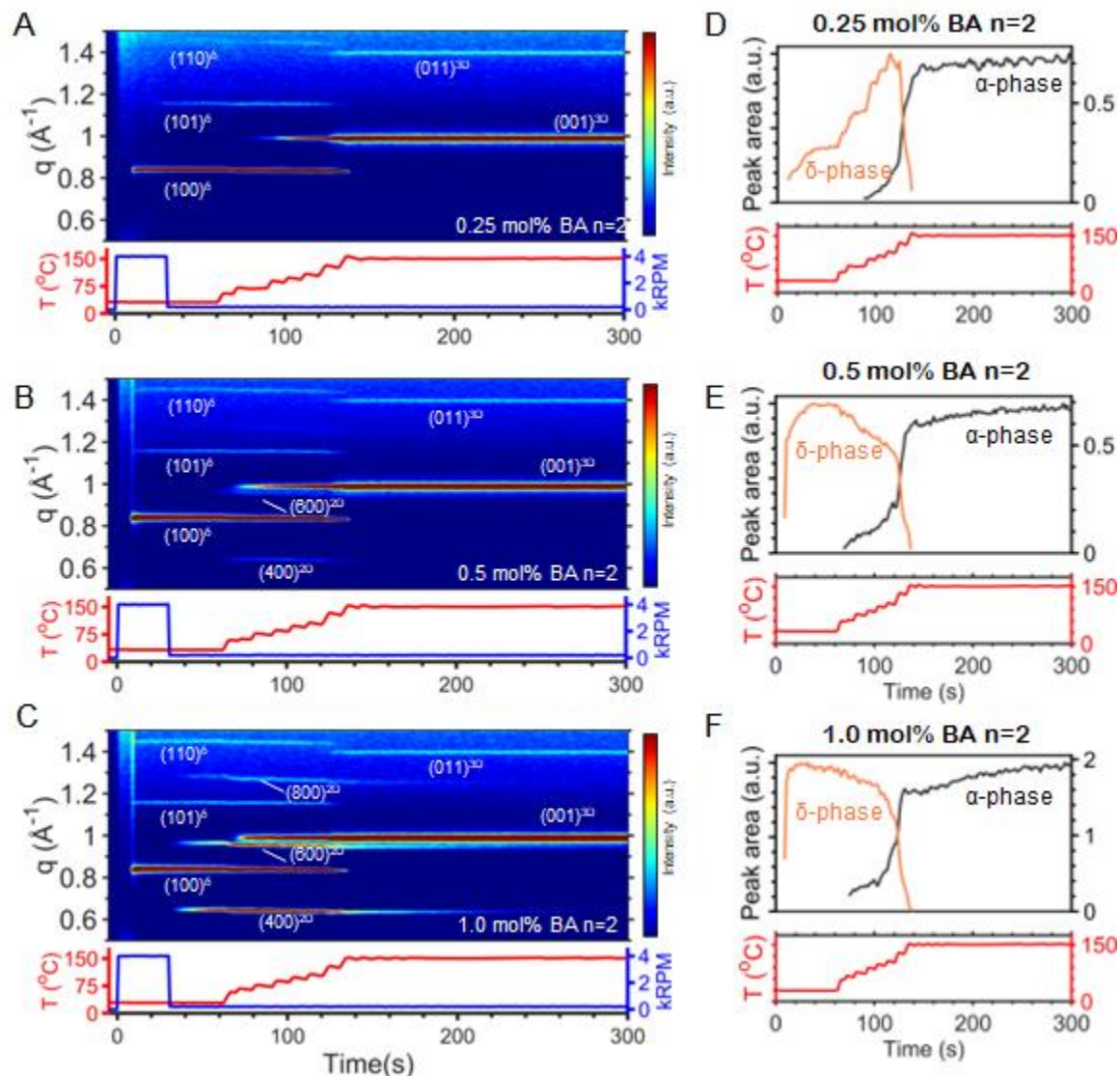
1187

1188

1189

1190

1191



1192

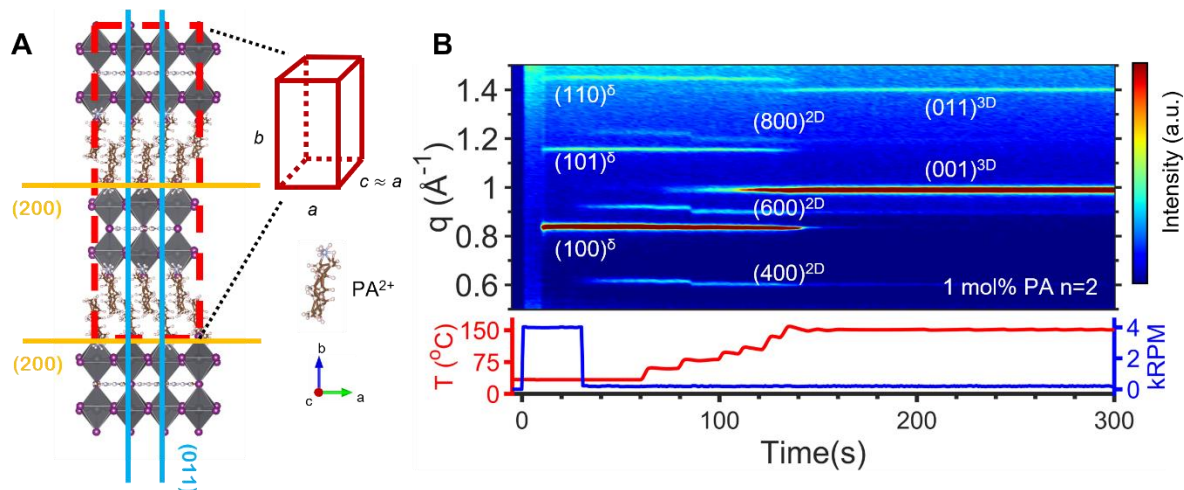
1193

1194 **Fig. S7. Structural dynamics of $\text{BA}_2\text{FAPb}_2\text{I}_7$ -doped FAPbI_3 with different dopant**1195 **concentrations during thin-film formation. A-C.** Contour plot of the in-situ WAXS1196 **measurement for FAPbI_3 doped with 0.25 mol% (A.), 0.5 mol% (B.), and 1.0 mol% (C.) BA $n=2$** 1197 **crystals. Illustrated on the contour plots are Miller indices for the α (3D), δ , and 2D phases. D-F.**1198 **Integrated peak areas for the $(100)^\delta$ (orange) and $(001)^{\delta 3D}$ (black) peaks over time for 0.25 mol%**1199 **(D.), 0.5 mol% (E.), and 1.0 mol% (F.) $\text{BA}_2\text{FAPb}_2\text{I}_7$ -doped FAPbI_3 . The $(001)^{\delta 3D}$ peak area is**1200 **normalized to the maximum of the $(100)^\delta$ peak area.**

1201

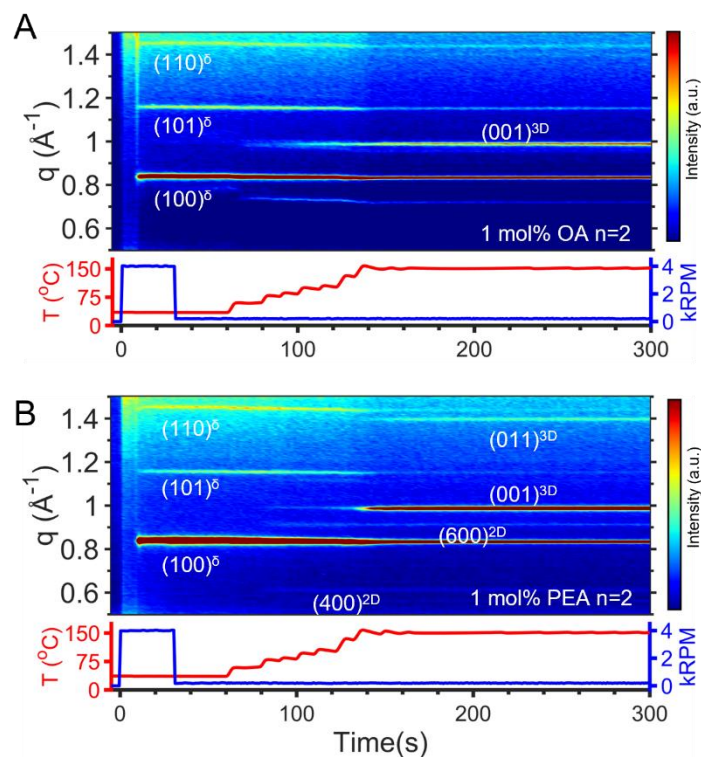
1201

1202
1203
1204
1205
1206



1207
1208
1209
1210
1211
1212
1213
1214
1215
1216
1217
1218

Fig. S8. Structural dynamics of PA₂FAPb₂I₇ doped FAPbI₃ during thin-film formation. A. Structure of the RP $n = 2$ perovskites in the out-of-plane axis. The unit cell is indicated by the dashed line. The out-of-plane (002) **B.** Contour and parameter plot of the in-situ WAXS measurement for 1 mol% PA₂FAPb₂I₇ doped FAPbI₃. Illustrated on the contour plots are Miller indices for the α (3D), δ and 2D phases.



1219

1220 **Fig. S9. Structural dynamics of $\text{PEA}_2\text{FAPb}_2\text{I}_7$ and $\text{OA}_2\text{FAPb}_2\text{I}_7$ doped FAPbI_3 crystals**
 1221 **during thin-film formation. A-B.** Contour plot of the in-situ WAXS measurement for 1 mol%
 1222 PEA- (A.) and OA- (B.) based FAPbI_3 films. Illustrated on the contour plots are Miller indices for
 1223 the α (3D) and δ phases.
 1224

1225

1226

1227

1228

1229

1230

1231

1232

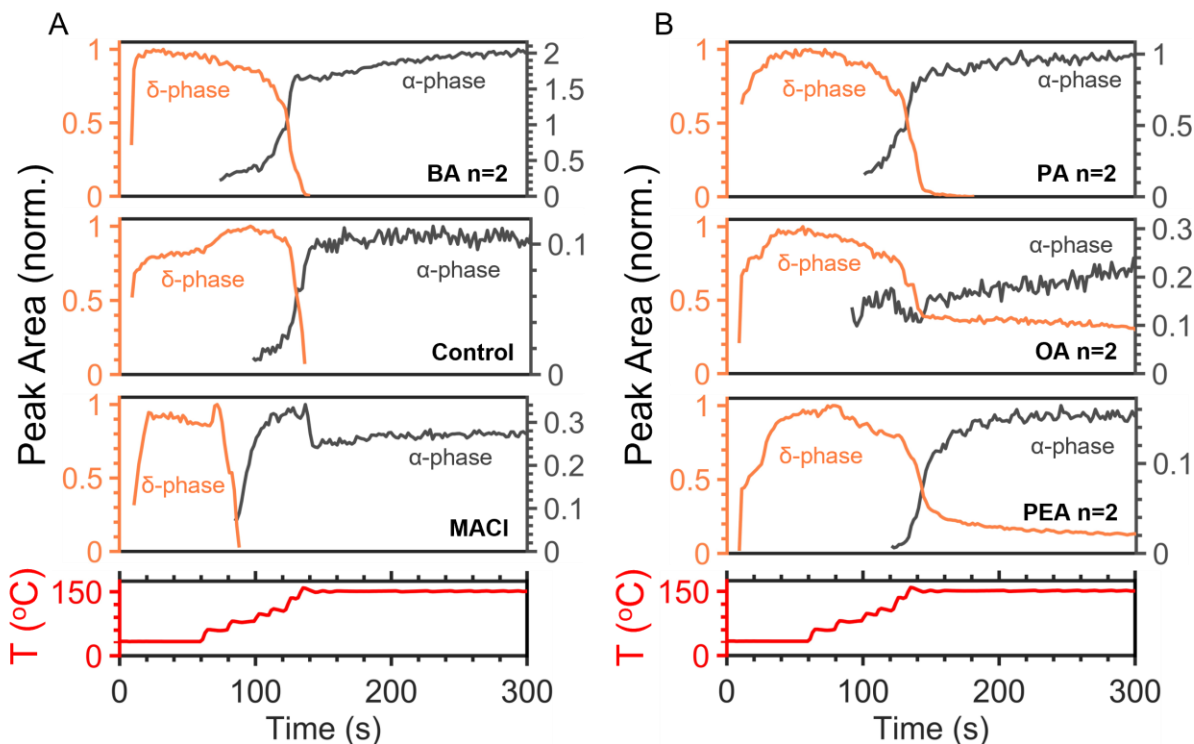
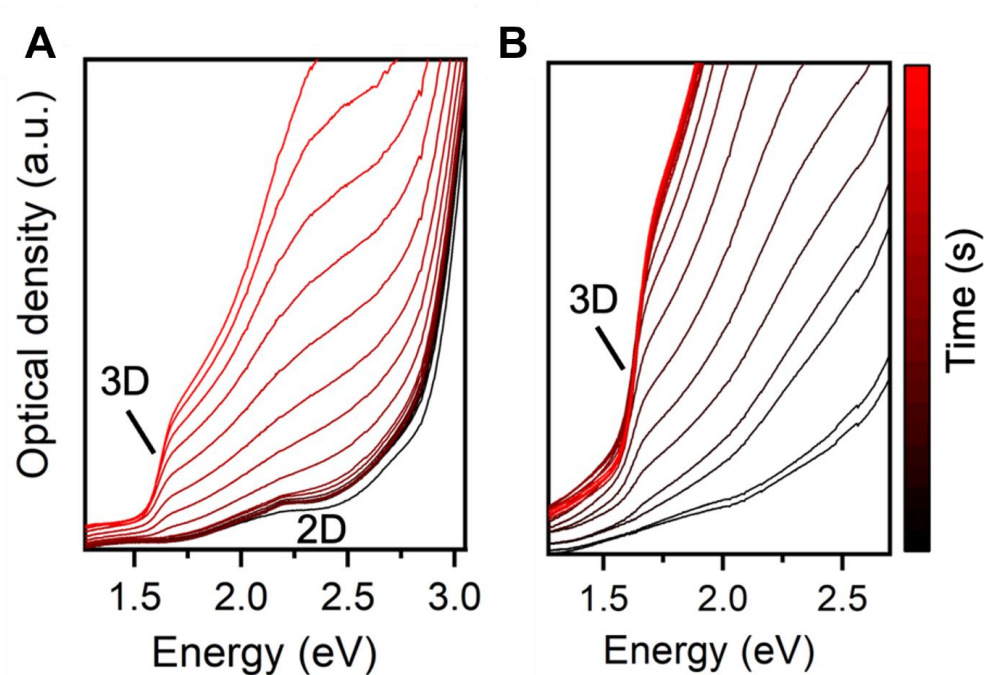


Fig. S10. Integrated peak areas for the (100)^δ (orange) and (001)^{3D} (gray) peaks over time. A. 1 mol% BA₂FAPb₂I₇-doped FAPbI₃ (top), undoped FAPbI₃ (middle), and 35 mol% MACl-doped FAPbI₃ (bottom). **B.** 1 mol% PA₂FAPb₂I₇-doped FAPbI₃ (top), 1 mol% OA₂FAPb₂I₇-doped FAPbI₃ (middle), and 1 mol% PEA₂FAPb₂I₇-doped FAPbI₃ (bottom). The (001)^{3D} peak area is normalized to the maximum of the (100)^δ peak area.

1233
 1234
 1235
 1236
 1237
 1238
 1239
 1240
 1241
 1242
 1243
 1244
 1245
 1246
 1247
 1248
 1249
 1250
 1251
 1252
 1253
 1254
 1255
 1256
 1257
 1258
 1259

1260



1261

1262 **Fig. S11. In-situ optical absorption during thin-film annealing at 150 °C.** Evolution of
1263 absorption pattern for the BA₂FAPb₂I₇ 2D doped FAPbI₃ (A.) and the control (B.) thin-films at
1264 150°C. The gradient color represent time from 0s to 300s.

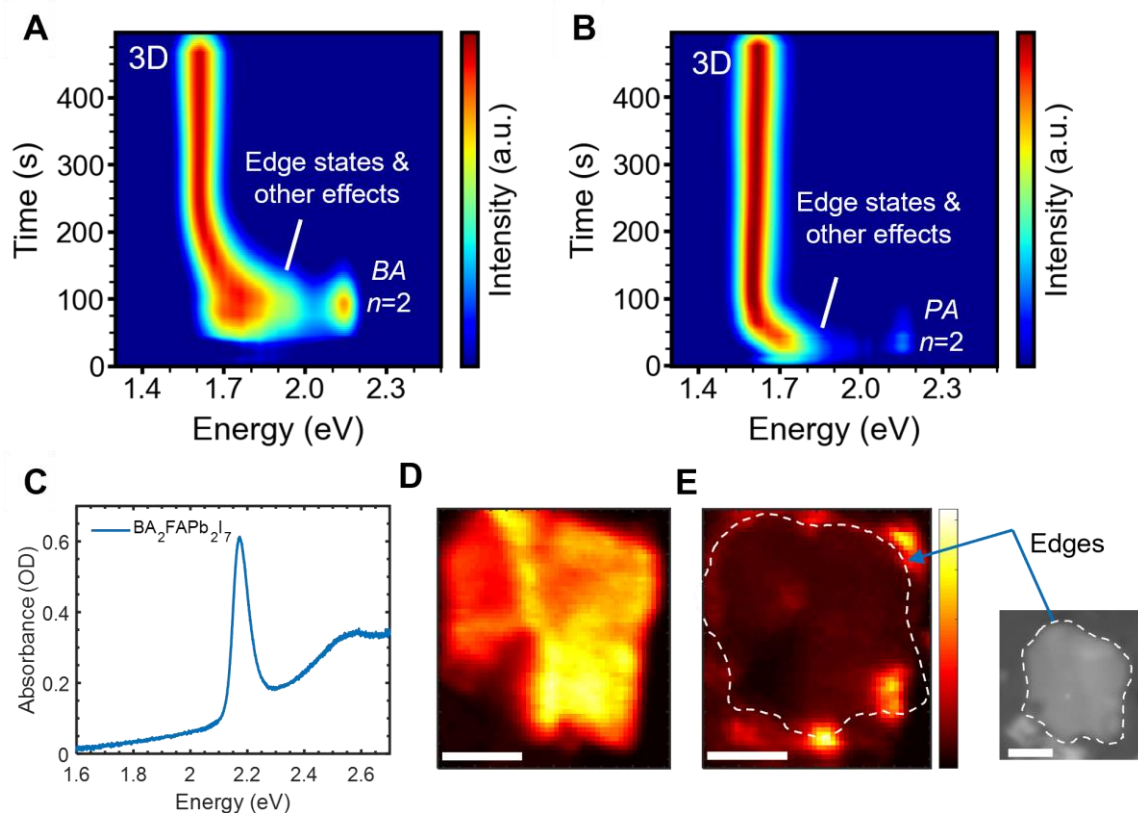
1265

1266

1267

1268

1269



1270

1271 **Fig. S12. Optical properties of 2D doped FAPbI₃ perovskite film and origins of low energy**
 1272 **emission. A - B.** In-situ photoluminescence measurement of the 0.5 mol% BA₂FAPb₂I₇ (A.) and
 1273 PA₂FAPb₂I₇ (B.) doped FAPbI₃ during thin-film formation at 150°C. Denoted on the figure are
 1274 the corresponding emission from different phases. The observed distribution in the bandgap from
 1275 the n=2 2D perovskite to the FAPbI₃ perovskite observed in Fig. S12 (A-B) serves as a clear
 1276 indication of the intercalation process leading to higher n and eventually 3D FAPbI₃ during the
 1277 annealing process. Notably, pentylammonium (PA) exhibits lower rigidity (longer alkyl chain)
 1278 compared to the butylammonium organic cation. This increased flexibility accelerates the
 1279 intercalation process, resulting in a faster conversion to the 3D FAPbI₃ band gap within 100
 1280 seconds. Conversely, the butylammonium demonstrates a wider bandgap distribution and takes a
 1281 longer time (200 seconds) to convert to the FAPbI₃ band gap. C. Optical absorption spectra of an
 1282 exfoliated single crystal BA₂FAPb₂I₇ perovskite. D. and E. The corresponding photoluminescence
 1283 intensity map probed at 2.14 eV (exciton ground state) (D.) and 1.81 eV (E.). Microscopic image
 1284 showing the exfoliated perovskite on the right. Scale bar is 10 μm.

1285

1286

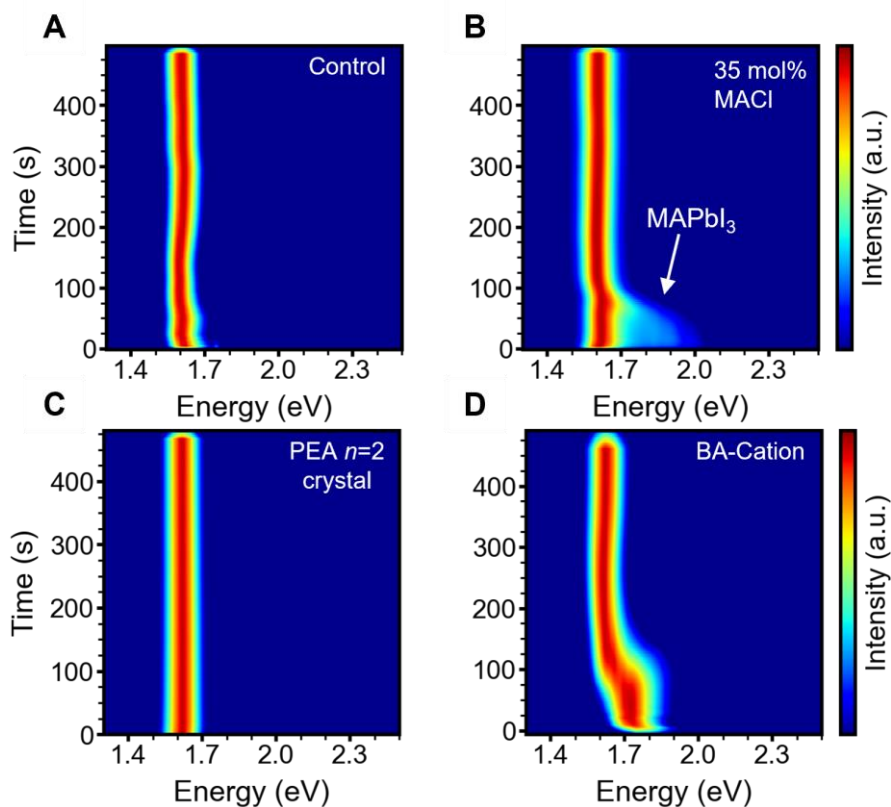
1287

1288

1289

1290

1291



1292

1293

1294 **Fig. S13. In-situ photoluminescence spectra during thin-film annealing at 150°C.** Heat-plots
1295 for time-dependent photoluminescence spectra of control (A.), MACI doped (B.), 1.0 mol%
1296 PEA₂FAPb₂I₇ (C.) and 1.0 mol% BAI doped (D.) FAPbI₃ films at 150°C. The emission peak from
1297 the MAPbI₃ 3D perovskite is labelled on subplot (B.)

1298

1299

1300

1301

1302

1303

1304

1305

1306

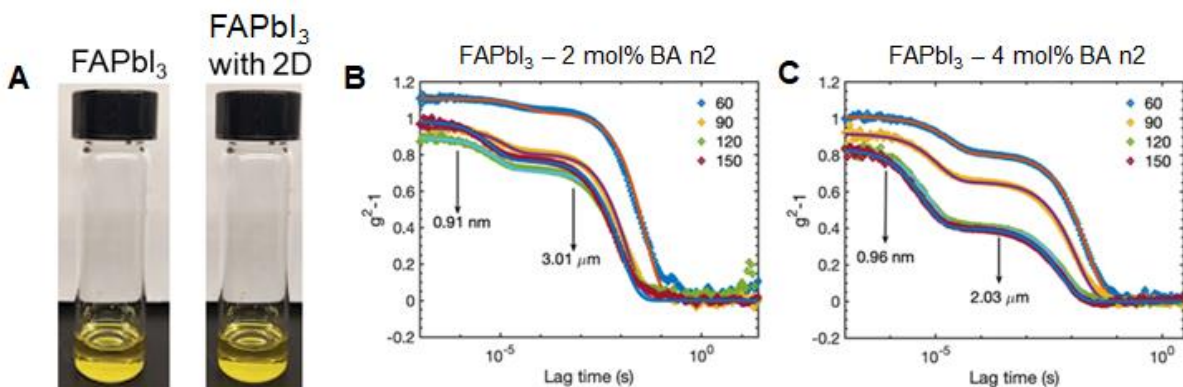
1307

1308

1309

1310

1311



1312

1313

1314

1315 **Fig. S14. A.** Optical images of precursor solution of (left) pure FAPbI₃ and (right) FAPbI₃ with

1316 2D seeds. **B, C.** Dynamic Light scattering measurement of different concentrations of BA₂FAPb₂I₇

1317 dopants. Correlation function (g^2) versus lag time measured at several scattering angles overlaid

1318 with the corresponding fits to determine the particle size.

1319

1320

1321

1322

1323

1324

1325

1326

1327

1328

1329

1330

1331

1332

1333

1334

1335

1336

1337

1338

1339

1340

1341

1342

1343

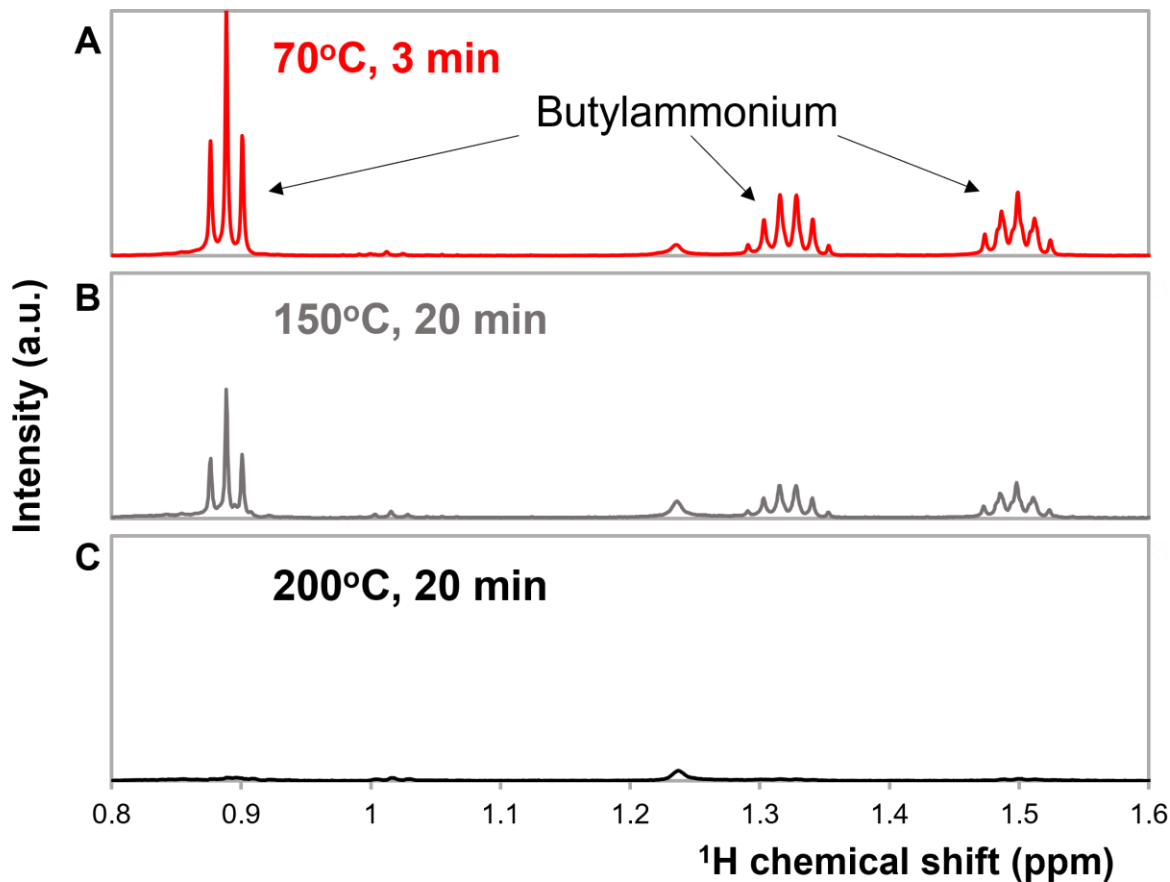
1344

1345

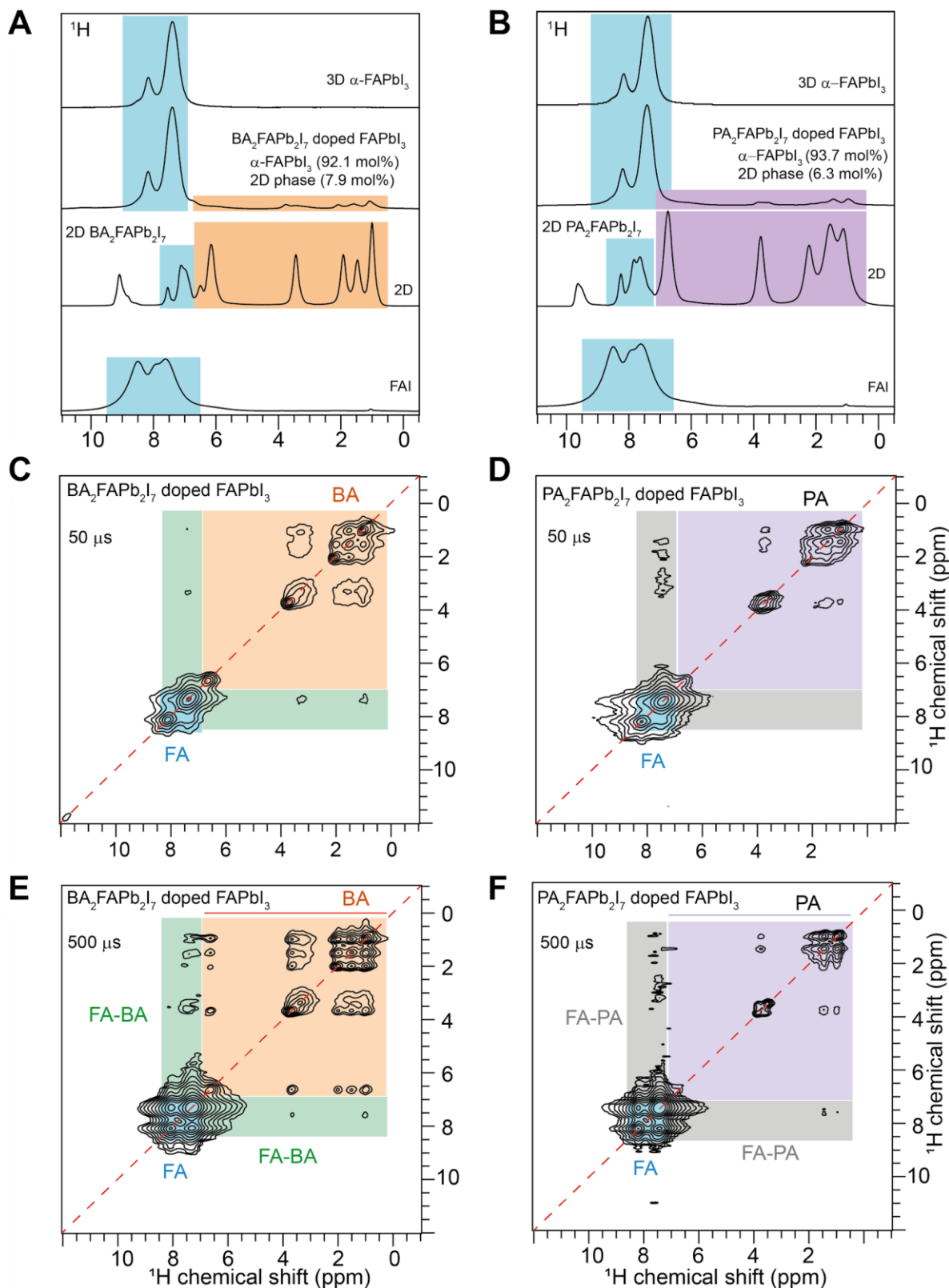
1346

1347

1348
1349
1350
1351
1352



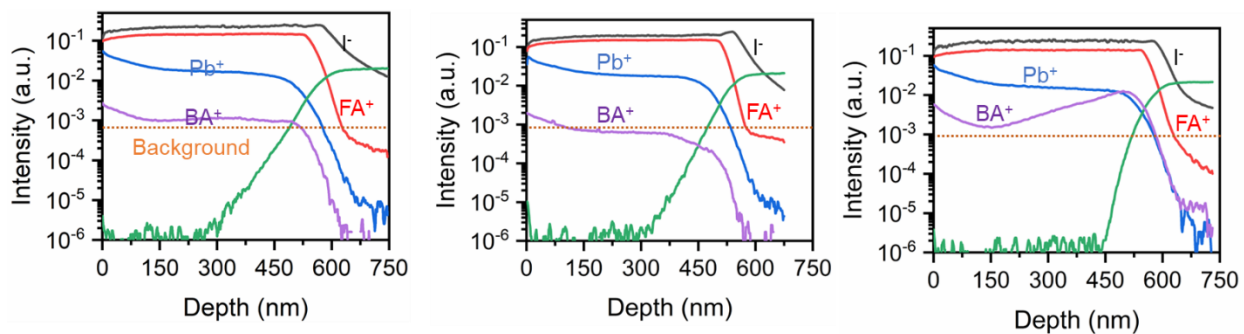
1353
1354 **Fig. S15. Solution-state ^1H NMR spectra of 2D-stabilized FAPbI_3 .** NMR of FAPbI_3 – 5 mol%
1355 BA n=2 films annealed at (A.) 70°C for 3 min, (B.) 150°C for 20 min, and (C.) 200°C for 20 min.
1356 A higher BA n=2 concentration was employed to better resolve the butylammonium signal. Films
1357 were scraped with a blade and the resultant powder was dissolved in deuterated DMSO. Spectra
1358 normalized to the FA peaks (not shown). After annealing for 20 min at 150°C ~65% of the initial
1359 BA remains in the film. After 20 min at 200°C nearly all BA has left the film.
1360
1361
1362



1363
1364
1365

Fig. S16. Solid-state 1D ^1H NMR spectra of 2D-stabilized FAPbI_3 . a-b. Comparison of 1 mol% $\text{BA}_2\text{FAPb}_2\text{I}_7$ and $\text{PA}_2\text{FAPb}_2\text{I}_7$ with stabilized FAPbI_3 after annealing films for 20 min at

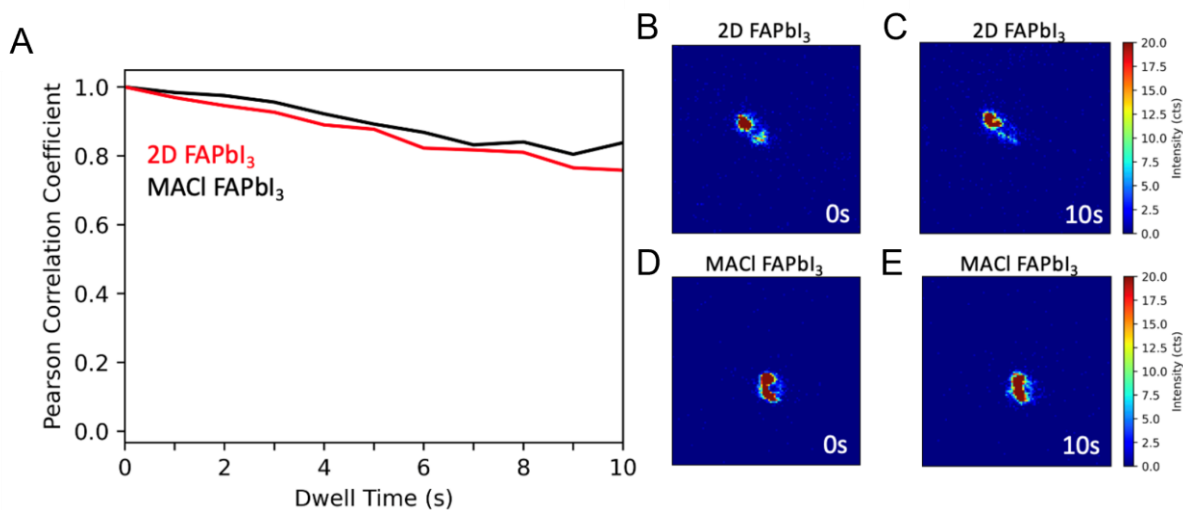
1366 150°C in ambient air. **c-f.** 2D 1H-1H correlation NMR spectra of the 2D doped materials with
1367 coloured boxes in the insets indicating the peaks correspond to large (BA or PA) and small (FA)
1368 cations, and through-space interactions between them.
1369



1370
 1371 **Fig. S17. ToF-SIMS of FAPbI₃ films.** Left: 0 mol% BA₂FAPb₂I₇. Middle: 0.5 mol%. Right: 1.0
 1372 mol%.

1373
 1374

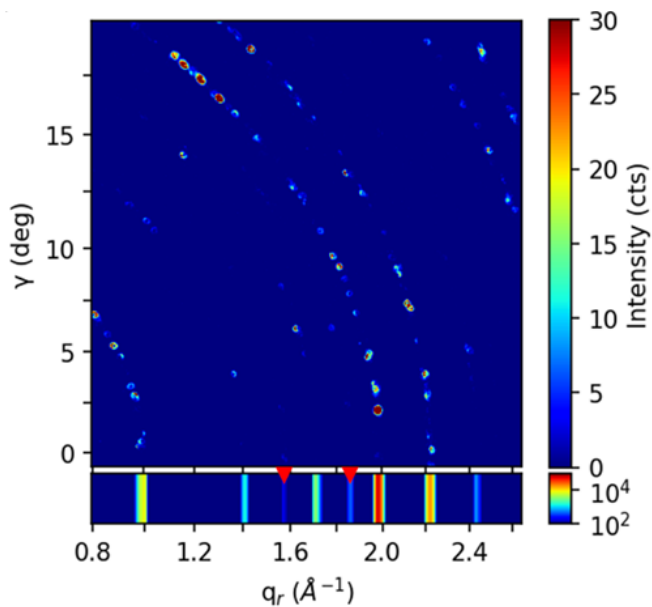
1375



1376
1377
1378
1379
1380
1381
1382
1383
1384
1385
1386
1387
1388

Fig. S18. X-ray stability over time with irradiation at a single point. **A.** Pearson correlation coefficient of the CCD image of the diffraction pattern with respect to the initial diffraction CCD image over 10 s of irradiation time. The substantial correlation over long times indicates X-ray stability much longer than the 100ms dwell time used for nanoprobe diffraction mapping. **B-C.** Diffraction CCD images from single point dwell of 2D FAPbI₃ at t=0 s (**B**) and t=10 s (**C**). **D-E.** Diffraction CCD images from single point dwell of MACl FAPbI₃ at t=0 s (**D**) and t=10 s (**E**).

1389



1390 **Fig. S19. Nanoscale structural properties.** Top: Summed CCD image from a nano-diffraction
1391 mapping of a 2D-stabilized FAPbI₃ sample. Abscissa: q_r (\AA^{-1}), ordinate: azimuthal angle: γ
1392 (degrees). Bottom: azimuthally integrated diffraction pattern, plotted in log scale to make minority
1393 phases apparent. Red triangles denote indexed tetragonal peaks.
1394

1395

1396

1397

1398

1399

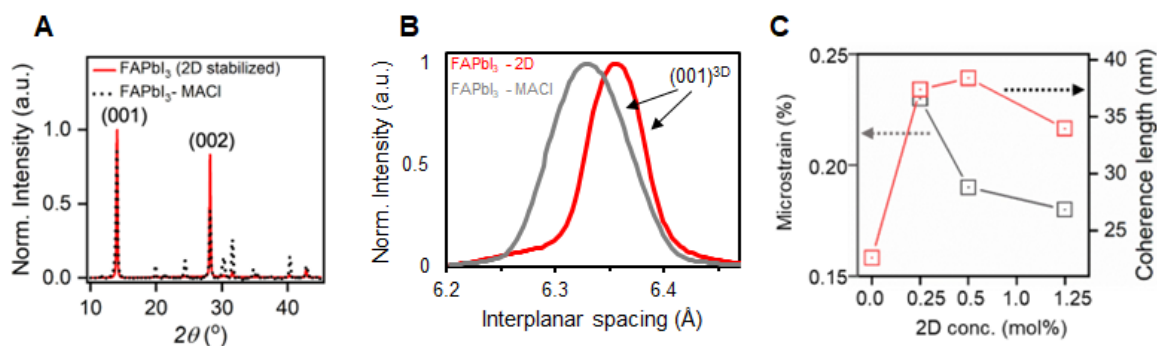
1400

1401

1402

1403

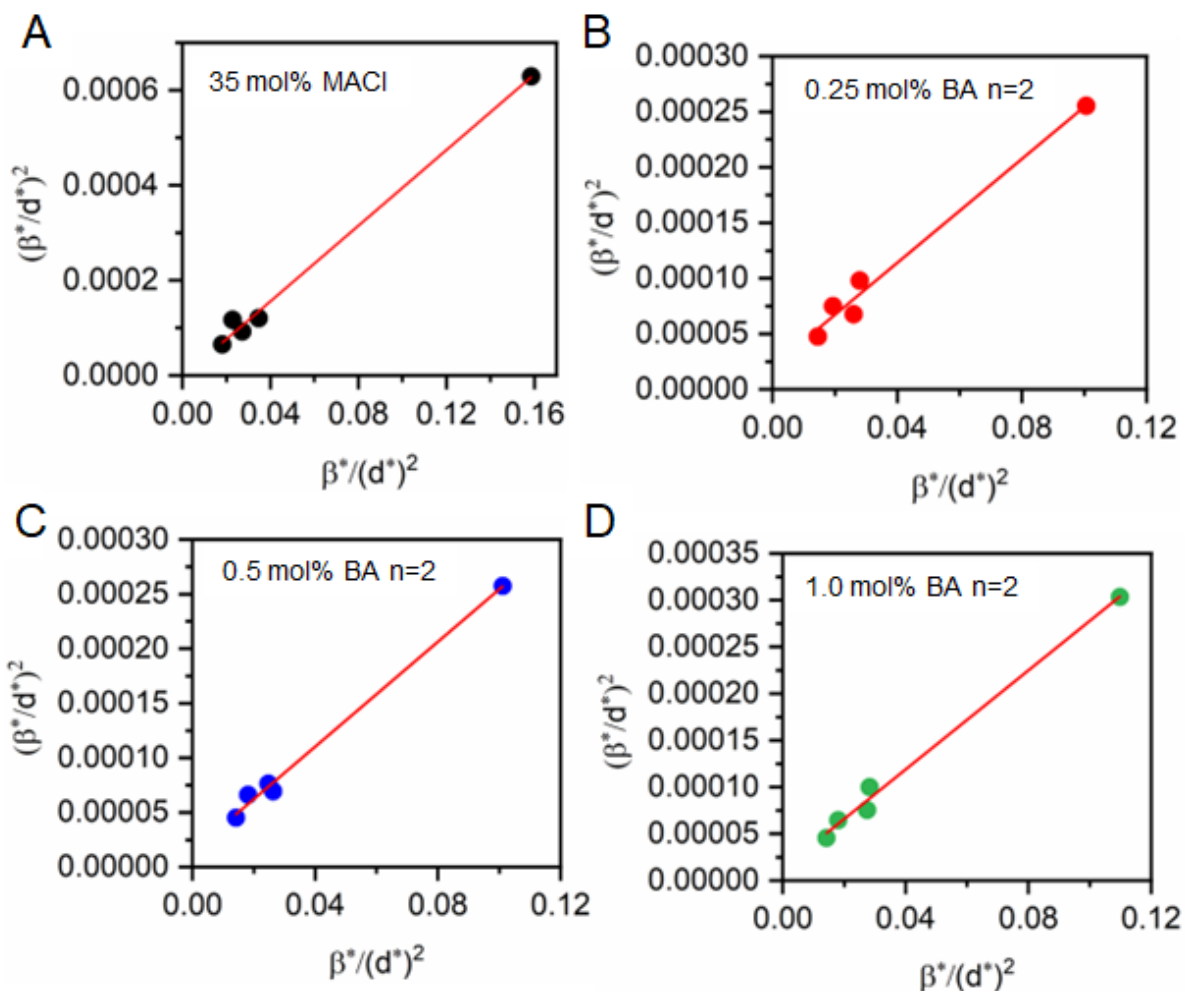
1404



1405
1406 **Fig. S20. Structural characterization of the $\text{BA}_2\text{FAPb}_2\text{I}_7$ and MACl doped FAPbI_3 thin film.**
1407 **A.** Room temperature X-ray diffraction spectra of the $\text{BA}_2\text{FAPb}_2\text{I}_7$ and MACl doped FAPbI_3 thin
1408 film. **B.** Summed diffraction intensity as a function of interplanar spacing showing the $(001)^{3D}$
1409 spacing for the $\text{BA}_2\text{FAPb}_2\text{I}_7$ and MACl doped FAPbI_3 thin film. **C.** Halder-Wagner analysis of the
1410 micro-strain and coherence length of various concentration of $\text{BA}_2\text{FAPb}_2\text{I}_7$ crystal doping.
1411

1412

1413

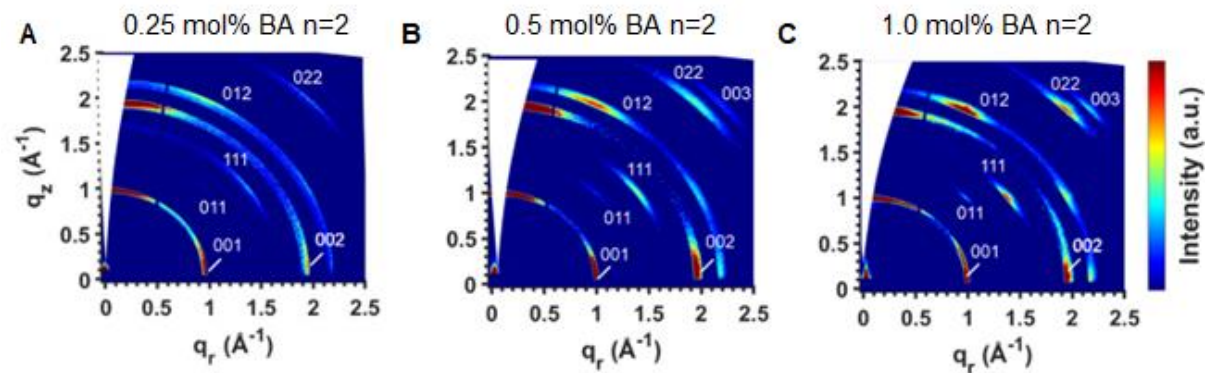


1414
 1415 **Fig. S21. Halder-Wagner plot for FAPbI₃ with various 2D dopant concentrations. A.** 35
 1416 mol% MAI. **B.** 0.25 mol% BA n=2. **C.** 0.5 mol% BA n=2. **D.** 1.0 mol% BA n=2. The Halder-
 1417 Wagner plot is used for extracting the strain ε and crystallite size D from XRD data using the
 1418 equation $\left(\frac{\beta^*}{d^*}\right)^2 = \frac{K}{D} \cdot \frac{\beta^*}{(d^*)^2} + (2\varepsilon)^2$, where $\beta^* = \frac{\beta \cos \theta}{\lambda}$ is the integral breadth of the reciprocal
 1419 lattice point, $d^* = \frac{2 \sin \theta}{\lambda}$ is the reciprocal lattice plane spacing, and K is the shape factor.

1420

1421

1422



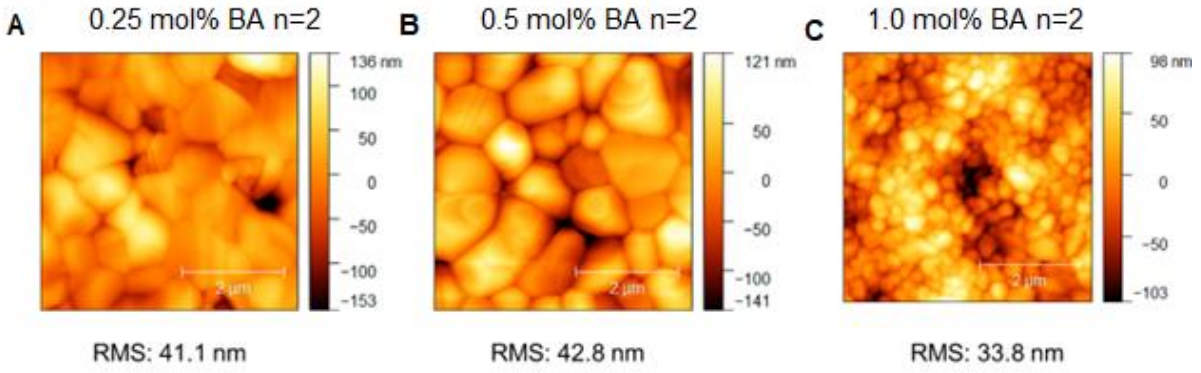
1423

1424

1425

1426

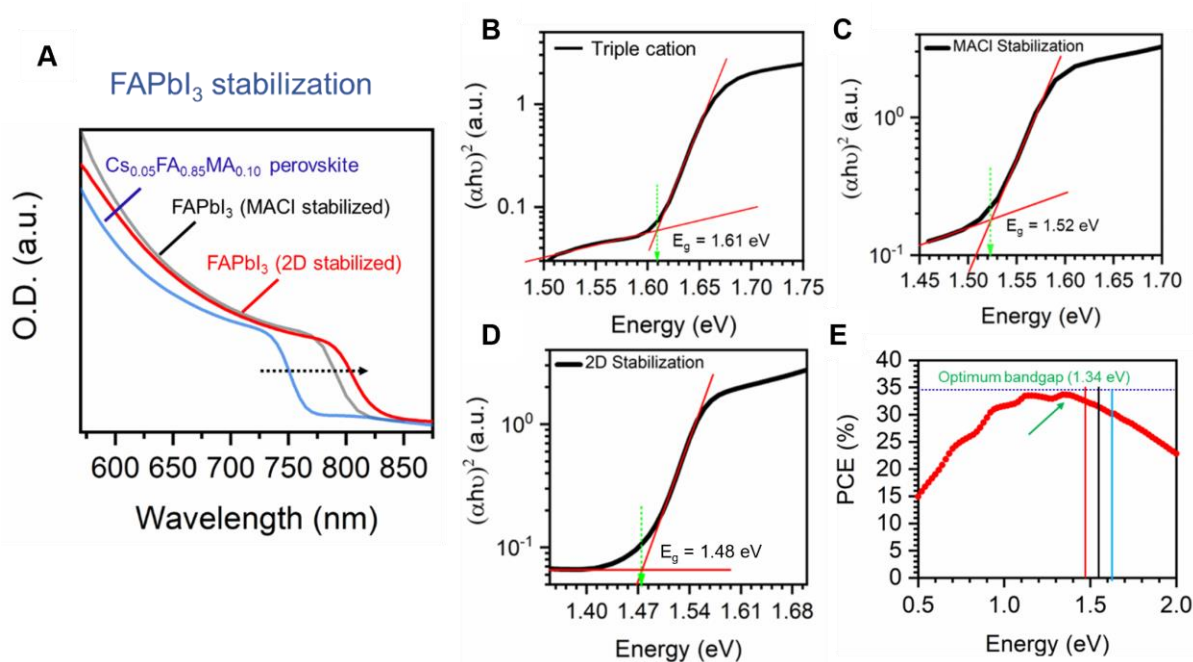
Fig. S22: Grazing Incidence Wide-Angle X-ray scattering patterns for various BA₂FAPb₂I₇ doping concentrations. A. 0.25 mol%. B. 0.5 mol%. C. 1.0 mol%.



1427
1428
1429
1430
1431

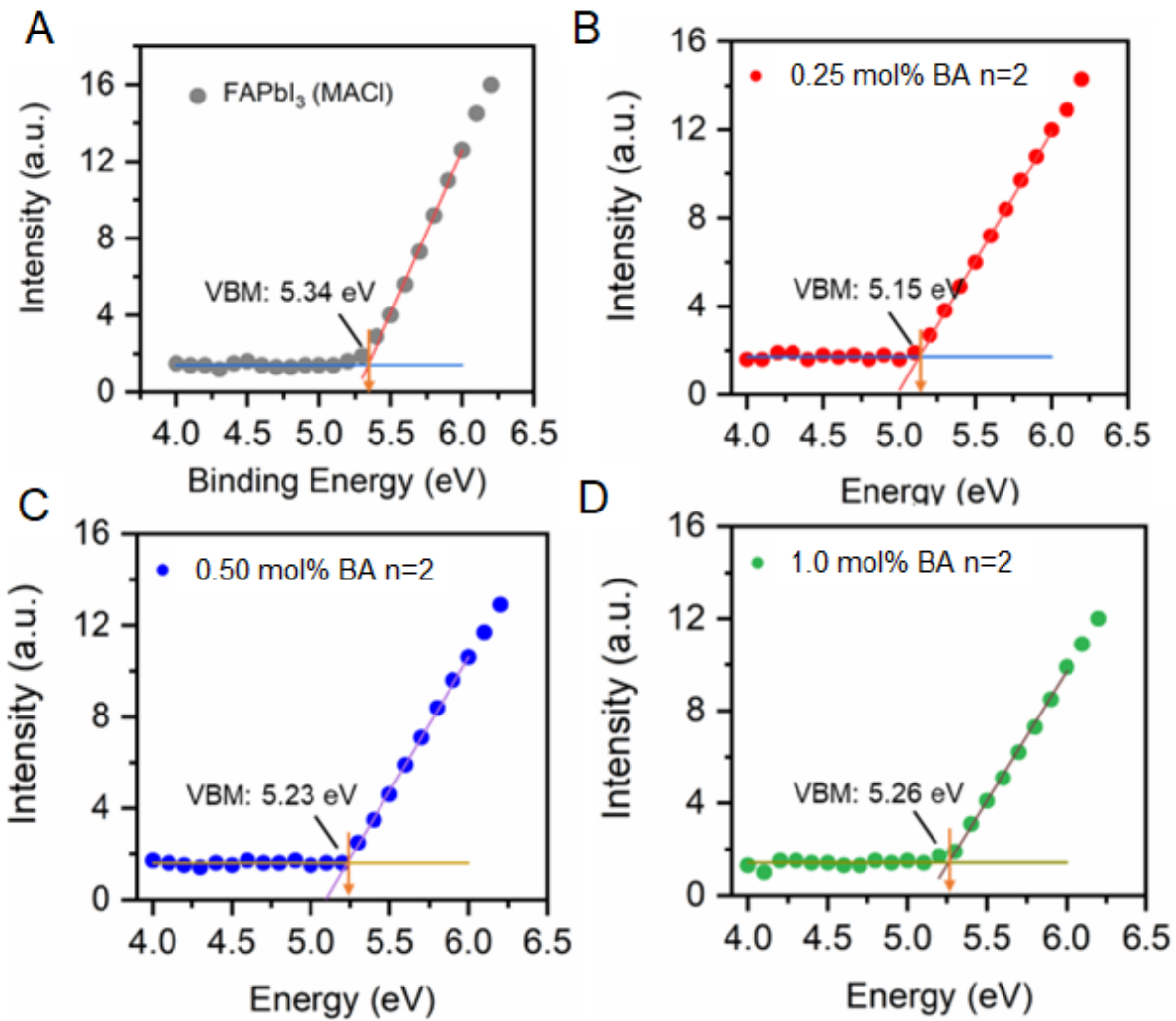
Fig. S23. Morphology of FAPbI₃ thin films. (a-c.) AFM images showing the variation in morphology of the FAPbI₃ thin film with different concentration of the 2D BA₂FAPb₂I₇ perovskite dopant with the extracted RMS roughness. **A.** 0.25 mol%. **B.** 0.5 mol%. **C.** 1.0 mol%.

1432



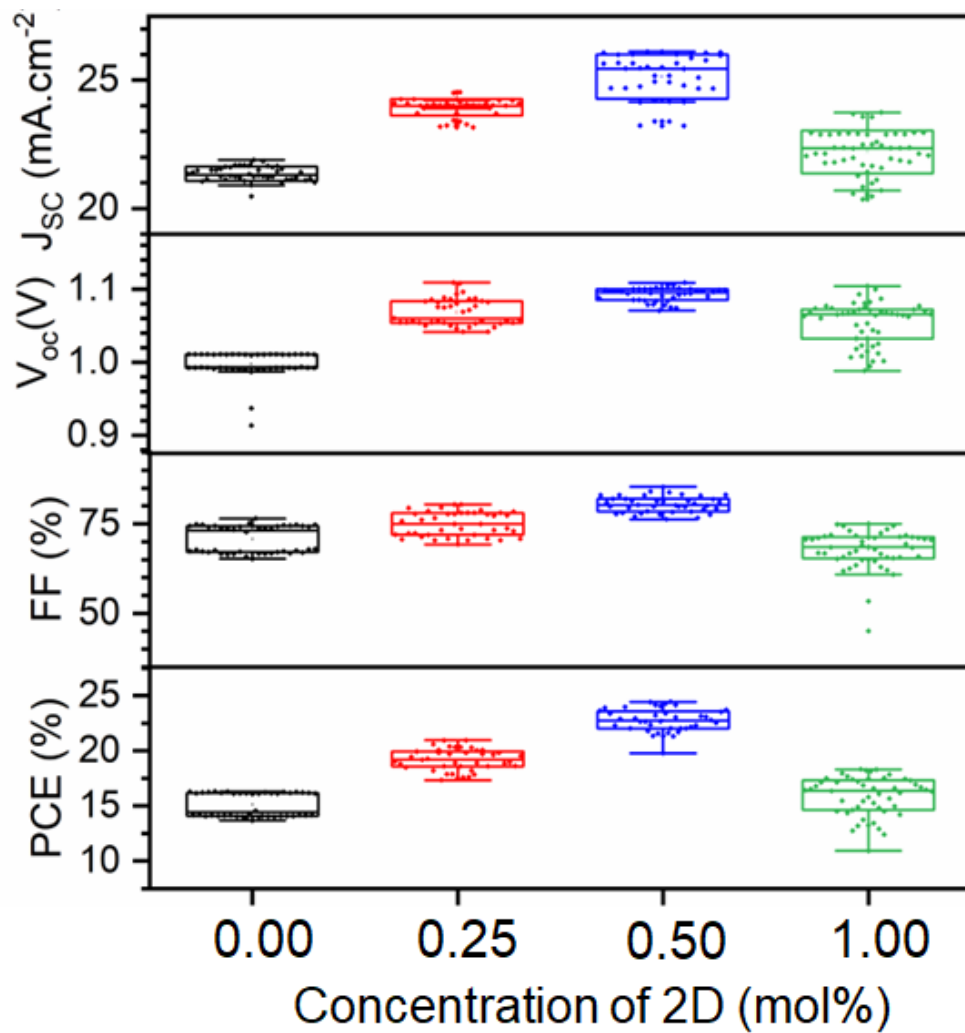
1434
 1435
 1436
 1437
 1438
 1439

Fig. S24. Bandgaps of perovskite films. **A.** Absorption spectra of Cs_{0.05}FA_{0.85}MA_{0.10}Pb(I_{0.9}Br_{0.1})₃ (triple cation) films (blue), MACI-stabilized FAPbI₃ (black), and BA₂FAPb₂I₇-stabilized FAPbI₃ (red). **B-D.** Tauc plot of triple cation film (**B**), MACI-stabilized FAPbI₃ film (**C**), and 2D-stabilized film (**D**). **E.** Bandgaps of each film shown as vertical lines on the Shockley-Queisser limit curve.



1440

1441 **Fig. S25. PES Spectra.** Plots showing the evolution of valence band maximum of the FAPbI₃ thin
 1442 films with **A.** MAI doping, and **B-D.** different concentration of BA₂FAPb₂I₇ 2D perovskite. **B.**
 1443 0.25 mol%. **C.** 0.50 mol%. **D.** 1.0 mol%. The onset of signal indicates the position of the valence
 1444 band maximum.
 1445



1446

1447 **Fig. S26.** Distribution of J-V parameters from FAPbI₃ devices with various molar doping
 1448 concentrations of BA₂FAPb₂I₇.

1449

1450

1451

1452

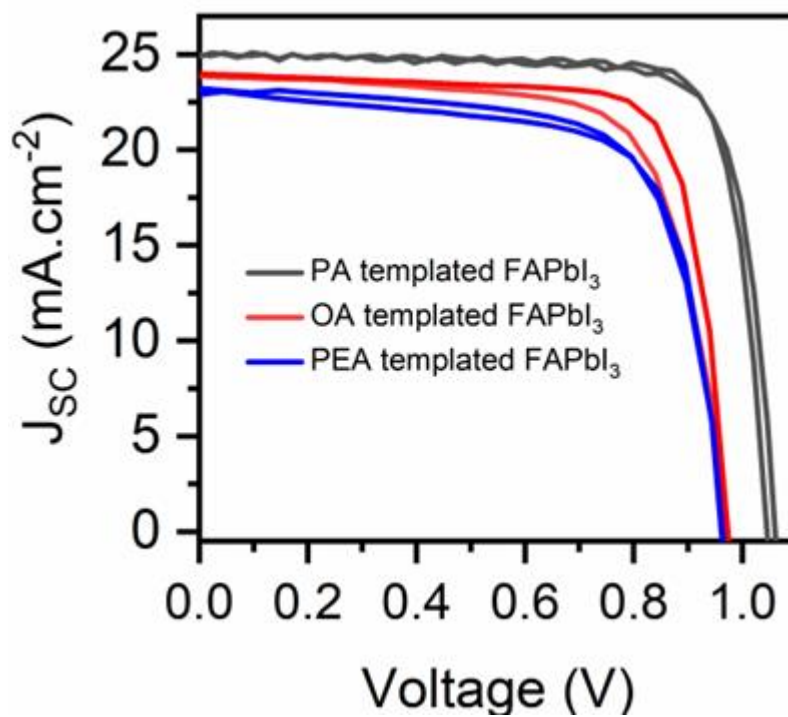
1453

1454

1455

1456

1457



1458

1459

Fig. S27. Plot showing the J-V curve of the champion device fabricated with 0.5 mol% of different 2D perovskite stabilization of FAPbI_3 .

1460

1461

1462

1463

1464

1465

1466

1467

1468

1469

1470

1471

1472

1473

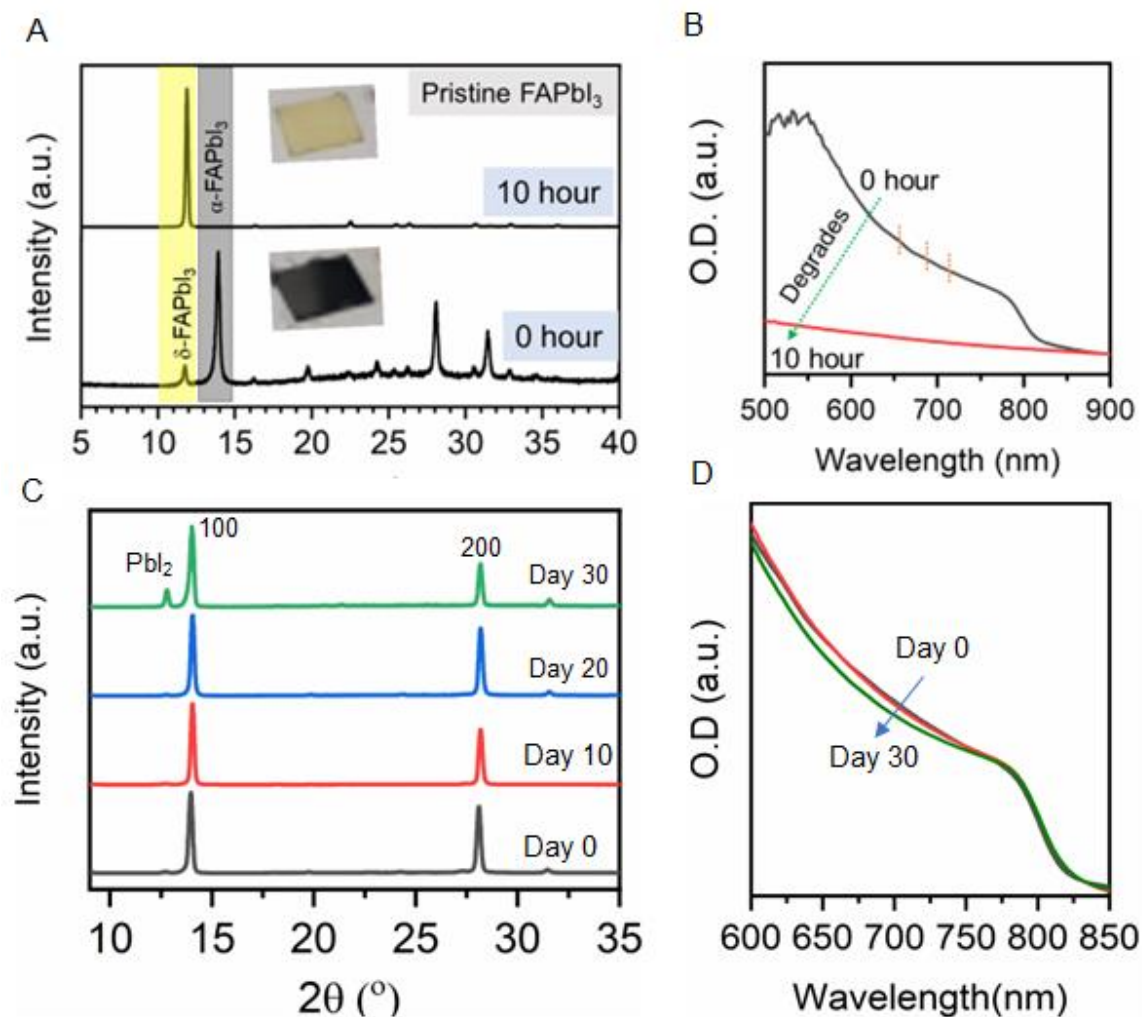
1474

1475

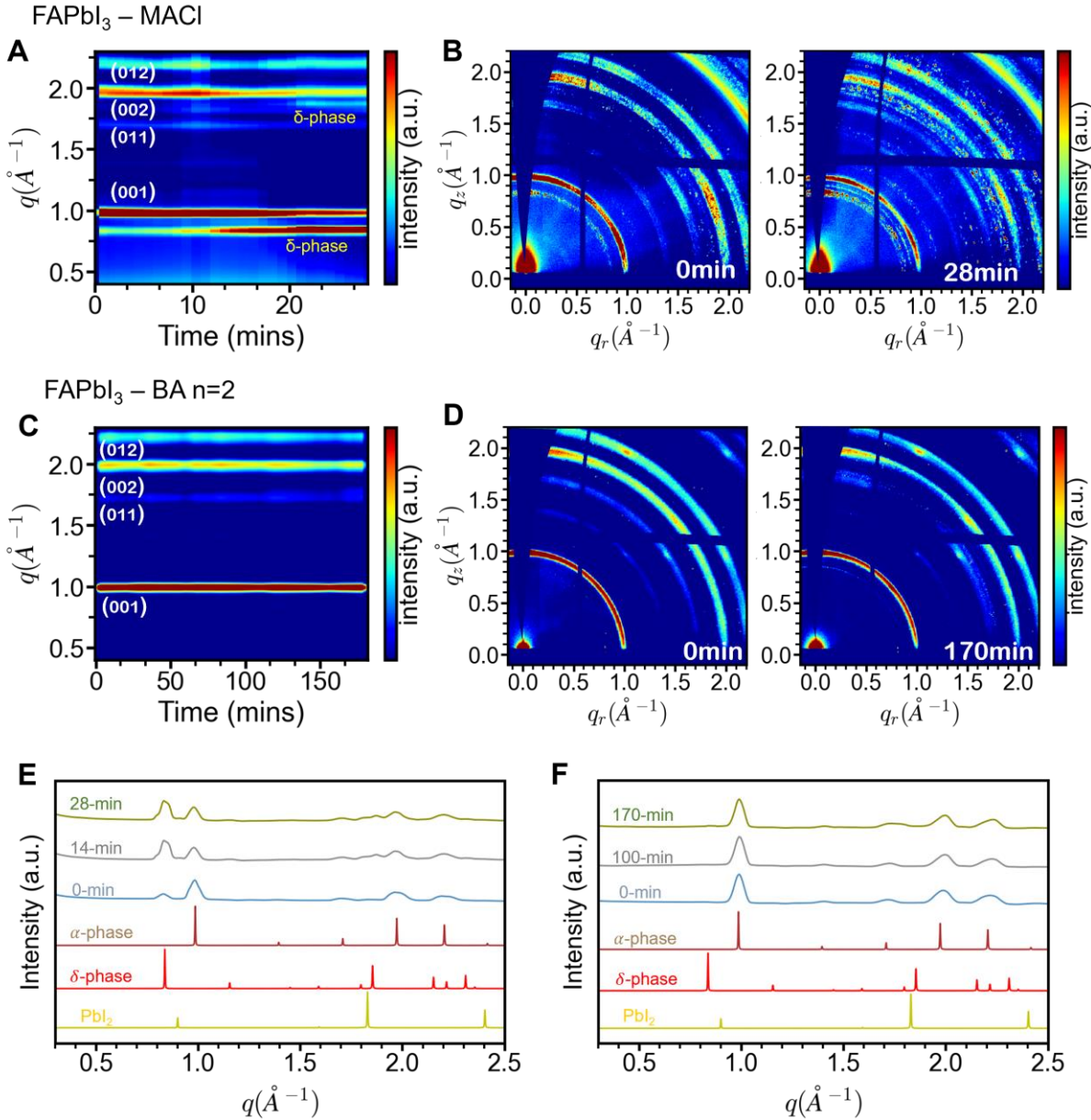
1476

1477

1478



1480 **Fig. S28. Shelf life stability.** **A.** 1D XRD and color images of undoped FAPbI₃ film. Bottom:
 1481 pristine. Top: after 10 hr in ambient air. **B.** 1D XRD and color images of 0.5 mol% BA n=2-doped
 1482 FAPbI₃ film. Bottom: pristine. Middle: after 10 days in ambient air. Top: after 30 days in ambient
 1483 air. **C-D.** Optical absorption spectra for pristine and 10 hr degraded undoped FAPbI₃ film (**C**) and
 1484 pristine, 10 days degraded, and 30 days degraded 0.5 mol% BA n=2-doped FAPbI₃ film (**D**).
 1485
 1486



1487
 1488 **Fig. S29. In-situ WAXS of degrading MACl-doped FAPbI₃ and BA n=2-doped FAPbI₃ p-i-n**
 1489 **devices at >90%RH, 1-sun illumination, and 65°C.** Device architecture is as reported above,
 1490 with a thinner (30nm) Au layer to allow the light and X-ray beam to penetrate. **A.** Azimuthally-
 1491 integrated GIWAXS pattern over time for FAPbI₃-MACl device. **B.** GIWAXS pattern at 0 min
 1492 (left) and 28 min (right) for the FAPbI₃-MACl device. **C.** Azimuthally-integrated GIWAXS
 1493 pattern over time for the FAPbI₃-2D device. **D.** GIWAXS pattern at 0 min (left) and 170 min (right)
 1494 for the FAPbI₃-2D device. **E.** Azimuthally-integrated GIWAXS pattern at 0 min, 14 min, and 28
 1495 min for FAPbI₃-MACl device, with α -FAPbI₃, δ -FAPbI₃, and PbI₂ diffraction peaks also shown.
 1496 **F.** Azimuthally-integrated GIWAXS pattern at 0 min, 100 min, and 170 min for FAPbI₃-2D device,
 1497 with α -FAPbI₃, δ -FAPbI₃, and PbI₂ diffraction peaks also shown.
 1498